8-2022

Materials Design for Energy Applications Using Ab- initio Calculations

Hind Hemaidee Alqurashi
University of Arkansas, Fayetteville

Materials Design for Energy Applications Using Ab- initio Calculations

A dissertation submitted in partial fulfillment
of the requirements for the degree of
Doctor of Philosophy in Microelectronic-Photonics

by

Hind Alqurashi
Umm Al-Qura University
Bachelor of Science in Physics, 2010
Pittsburg State University
Master of Science in Physics, 2016

August 2022
University of Arkansas

This dissertation is approved for recommendation to the Graduate Council.

Bothina Hamad Manasreh, Ph.D.
Dissertation Director

Omar Manasreh, Ph.D.
Committee Member

Morgan Ware, Ph.D.
Committee Member

Hugh Churchill, Ph.D.
Committee Member

Matthew Leftwich, Ph.D.
Ex-Officio Member

The following signatories attest that all software used in this dissertation was legally licensed for use by Hind Alqurashi for research purposes and publication.

Ms. Hind Alqurashi, Student	Dr. Bothina Hamad Manasreh, dissertation Director

This dissertation was submitted to http://www.turnitin.com for plagiarism review by the TurnItIn company's software. The signatories have examined the report on this dissertation that was returned by TurnItIn and attest that, in their opinion, the items highlighted by the software are incidental to common usage and are not plagiarized material.

Dr. Matthew Leftwich, Program Director	Dr. Bothina Hamad Manasreh, dissertation Director

Abstract

The structural, dynamical, electronic, and thermoelectric properties of rock-salt and wurtzite $Cd_{1-x}Zn_xO$ alloys, VTiRhZ (Al, Ga, In, Si, Ge, Sn) and ZrTiRhZ (Ge, Sn) quaternary Heusler alloys (QHAs) were investigated using density functional theory (DFT) and semi-classical Boltzmann transport theory. From these calculations, the alloys were identified as potential materials for future thermoelectric applications. Furthermore, the magnetic and spin-polarization properties of these QHAs were investigated. The total magnetic moments were found to be integer values for all QHAs. In addition, all studied QHAs except VTiRhAl possess a half-metallic behavior with a 100% spin-polarization. The half-metallic ferromagnetic behavior makes them promising materials for spintronic applications.

Moreover, the influence of the lattice anharmonicity on the lattice thermal conductivity of InTe monolayer were studied using the standard Boltzmann transport equation (BTE) approach and the self-consistent phonon with Boltzmann transport equation (SCP + BTE). The SCP + BTE approach is believed to be more valid and accurate than the standard BTE approach in predicting the κ_l value. These investigations using the SCP + BTE approach show that InTe monolayer is promising for thermoelectric applications.

Acknowledgements

First and foremost, I would like to express my gratitude to God Almighty for providing me with the chance and guidance that have enabled me to reach my goal and to be successful in this portion of my journey through life.

I am very grateful to Prof. Bothina for her great guidance, unwavering support, and patience throughout my Ph.D. studies. Her enormous expertise and vast experience have aided me throughout my academic research and daily life. I am really fortunate to have an adviser like Prof. Bothina that cared about my work and was always available to answer my inquiries. It would be impossible to express how much I owe her in suitable words. Much appreciation and love to her.

I would like to express my gratitude to Dr. Omar Manasreh, Dr. Morgan Ware, and Dr. Hugh Churchill for serving on my committee and contributing to my academic success. Also, I would like to express my heartfelt appreciation to Dr. Matthew, Dr. Wise, and Renee Jones Hearon for their unflinching and immensely helpful support during this journey. My heartfelt thanks also would go to my friends as well as my colleagues in the research group.

To my family, I want to express my gratitude for encouraging me in all of my endeavors and inspiring me to pursue my aspirations. I am thankful for my father's Hemaidee unwavering love and support, which kept me driven and self-assured. He helped me to achieve my goals and success because he believed in me. I would also like to thank my sisters Reem, Sarah, and Ghada, who without them this would have not been possible. I also appreciate all the support and encouragement that I received from my brothers Ayman, Esam, and Mohammed.

Last but not least, I would want to convey my heartfelt gratitude to my sponsor, Al-Baha University, and Saudi Arabian Cultural Mission, for financially supporting and providing me

with the opportunity to continue my education and expand my knowledge. I would like also to thank the high-performance computing of the University of Arkansas for performing our calculations.

Dedication

This dissertation is dedicated to my late lovely mother Amnah. She was instrumental in motivating me to seek a Ph.D. degree, but unfortunately, she could not see my graduation. This one is dedicated to her.

Table of contents

List of Figures

List of Tables

Chapter 1: Introduction

1.1 Motivation

The cost of energy utilized by the growing percentage of population and the resultant depletion of energy resources is associated not only with the exceeding economic cost but also social and environmental impact. Earth must be provided with sustainable energy resources if the future generations are to thrive on the same planet as scarce resources are a threat to the survival. The possible solution to this issue does not depend upon researching for alternatives such as fusion reactions or similar concepts that could solve the energy crisis problem in one attempt, but the energy sector has to be provided with incremental add-ons to harness such energy resources that have not been discovered or have not been worked upon to bring them to practical implementation. In the current scenario, the renewable energy resources are getting popular among the scientific world. Wind, solar, geo-thermal, and tidal energy are among the resources that scientists are pondering to enhance their efficiency to be utilized in the practical world.

Apart from the above-mentioned resources of renewable energy, thermoelectric solid-state materials are emerging as a promising source of clean energy. Such materials are good candidates for waste energy harvesting that can be recycled to produce electricity. For instance, in thermoelectric refrigerators, charge carriers are forced by a power source to move from one end to the other thereby creating a temperature gradient. The traditional system of electricity generation depends on compressors, pumps and gears may be replaced in the future by thermoelectric devices for the provision of durable and solid-state alternative. The only drawback of these devices is their low efficiency as compared to the conventional modes of electricity production. With the increasing power generation demand, the thermoelectric devices call for the development of their advanced generation using different materials that could provide

sustainable energy in adequate amounts capable of meeting the growing energy consumption. In order to produce energy comparable to the previous energy generation technologies, new thermoelectric materials are required to be introduced that could provide an enhanced efficiency of about three times higher than their current values [1].

By enhancing the efficiency of thermoelectric devices, it would become possible to employ the waste heat generated from currently neglected energy sources. Enhancing the efficiency of hybrid automobiles in the future requires the utilization of the generated automotive waste heat from as engines, brakes, and exhausts. The heat produced by these sources could be exploited on the industrial scale in nuclear power plants and electrical plants for provision of new energy sources. For extending the interference of humankind in space related tasks for exploration and discoveries, the thermoelectric generators based on radioisotopes could be the next generation of thermoelectric devices that would be capable of harnessing energy from waste heat released during radioactive decay. Through the implementation of thermoelectric power generation, the populations residing in underdeveloped regions struggling with energy issues could be provided with an energy source. The conversion of a burning stove into an LED lighting source could revolutionize the life in small remote villages. The dependency of humankind on energy produced by burning fossil fuels could be replaced by thermoelectric energy generation. Inexplicably intense scientific investigations would require time in developing the next generation of thermoelectric devices as prominent future energy source.

The current investigations include the search of new bulk materials as well as low-dimensional materials for thermoelectric applications. Bulk materials are being preferred by the scientific community exhibit the behavior of glass regarding their thermal conductivity which is low in contrast to the electrical conductivity which is high when the glass behaves as a crystal.

The name designated for these bulk materials is phonon glass electronic crystals. These crystals exhibit weak atomic bonding to provide phonons with scattering centers [2]. The other part is dealing with low-dimensional structures for thermoelectric energy generation. It has been shown an enhancement in the thermoelectric properties as a result of the quantum confinement. Upon lowering the dimension, the thermal conductivity would significantly decrease, which enhances the thermoelectric efficiency [3],[4],[5].

1.2 Thermoelectric Phenomenon

The discovery of thermoelectric effect is attributed to the curiosity of some individuals who invested their time in understanding the interrelationship between electrical current and heat energy. The first individual to delve into the concept of thermoelectric effect was Thomas Seebeck, a German physicist in early 19^{th} century [2]. His work revolved around the relationship between heat and magnetism, and he also explained the first ever thermoelectric generator that could convert the heat energy to voltage. However, later in 1834, another Physicist namely Jean Charles Peltier described the effect of thermoelectric refrigeration, which is the opposite mechanism of the Seebeck effect. The contribution of these two scientists to the invention of thermoelectric figure of merit ZT will be explained in the ensuing sections.

1.2.1 Seebeck Effect

Figure 1 presents the concept of heat transfer in a finite rod of a conducting material. If it is subjected to heat at only one end, thus charges tend to move from the region of high heat towards the region of low heat. Below the critical temperature (T_C), entropy is transferred along with the charge carriers in materials excluding superconductors. The charge carriers continue to travel towards the low heat side until equilibrium is established among both sides as depicted in the figure 1. When the temperature is further increased above the already established temperature

gradient, the charges will again begin their movement towards the cooler end thereby creating a new potential difference. The maximum voltage generated throughout the process is therefore restricted by the melting point of the material [2].

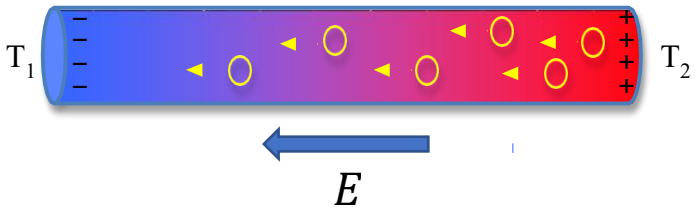

Figure 1. The movement of charge carriers down the gradient when T2 > T1.

Figure 1 depicts a thermoelectric element exhibiting the movement of charge carriers down the gradient when $T_2 > T_1$. In this figure, the yellow circles represent the electrons that move under the influence of heat energy. Due to the temperature gradient thus created, electrons continue to move to T_1 until equilibrium is established. Seebeck's coefficient can be expressed as S= μV / K.

When two different conductors are connected in such a manner that the temperature gradient exists between them when they are joined in series electrically and in parallel thermally, they produce a voltage see figure 2. This difference in potential forms the basis of Seebeck Effect. The focus of Seebeck was to investigate the power generating properties of materials forming a thermocouple and the effect thus produced was referred to as the Seebeck Effect. The voltage created in this phenomenon is dependent upon the Seebeck coefficient S and the temperature gradient existing between two dissimilar conductors forming a thermocouple. The Seebeck coefficient is the measure of the thermoelectric voltage in response to temperature gradient existing across the surface.

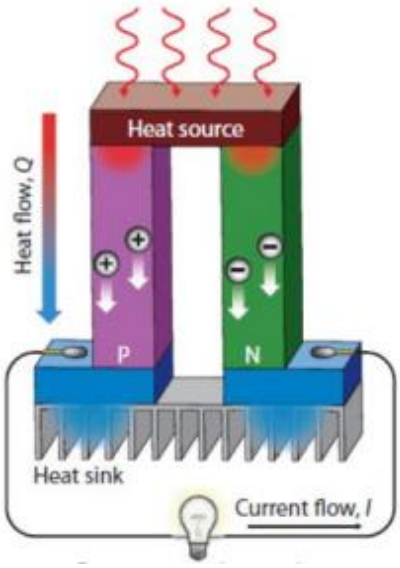

Figure 2. The Seebeck effect

1.2.2 Peltier Effect

The opposite form of Seebeck effect is referred to as the Peltier Effect, where the electromotive force is utilized for driving current in the thermocouple rather than creating a potential at different temperatures. The Peltier effect is associated with providing heat to one junction while cooling the other [2] (see Figure 3). In quantitative terms, the effect thus produced is defined by the Peltier coefficient. The ratio of Current (I) to the heating rate (q) determines the Peltier coefficient (π), which is defined as: $\pi = \frac{I}{q}$ [2].

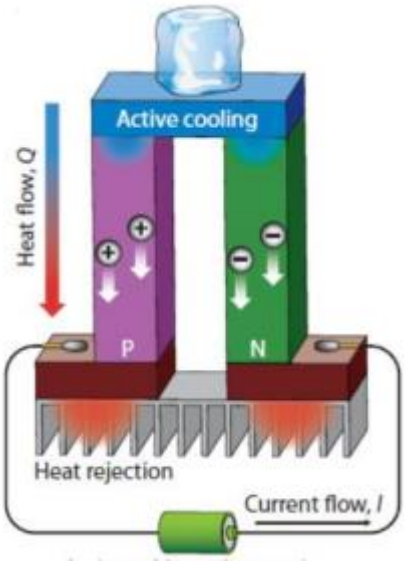

Figure 3. The Peltier effect.

1.2.3 Thermoelectric Figure of Merit

The thermoelectric properties exhibited by a material can be illustrated by employing Seebeck and Peltier effect. However, they are not capable of drawing comparison between the two materials conjoined to form a thermocouple. Thermal and electrical conductivity are not addressed by thermoelectric coefficients and are significant in determining the distinct characteristics of a certain material. When a substance exhibits a high thermoelectric efficiency, it has high Seebeck coefficient, high electrical conductivity and low thermal conductivity [3]. The relationship is thus expressed by using thermoelectric figure of merit ZT:

$$ZT = \left(\frac{S^2\sigma}{k}\right)T \qquad \text{Equation1}$$

Here, S represents the Seebeck coefficient, σ represents the electrical conductivity, κ represents the thermal conductivity, and T refers to the temperature. $S^2\sigma$ is defined as thermoelectric power.

The charge carriers (κ_e) flowing through the lattice and the vibrations of the lattice (κ_l) contribute to the thermal conductivity of the material, which is given as ($\kappa=\kappa_e+\kappa_l$).

When the concentration of charge carriers equalizes metals, the electronic thermal conductivity component exhibits more contribution to the net thermal conductivity κ. In regular thermoelectric materials, $_{Ke}$ contributes to 1/3 of the net thermal conductivity [2]. When the electrical conductivity of a bulk material is increased, the thermal conduction is also increased, and it is designated by Wiedemann-Franz law $\kappa = L\sigma T$ [6], here κ ($\kappa=\kappa_e+\kappa_l$) represents the total thermal conductivity, σ refers to electrical conductivity, L refers to the Lorenz factor, and T designates temperature.

The Lorenz factor exhibits a value of 2.44×10^{-8} conjoined [7]. This value is derived by using fundamental constants; however, the experimental values show slight variation between elements. For instance, the element Rubidium has Lorenz factor of 2.42×10^{-8} conjoined, whereas sodium has the L value 2.12×10^{-8} $W\Omega/K^2$ [7]. However, the independent increase in electrical conductivity not associated with thermal conductivity is prohibited by Wiedemann-Franz law for bulk materials. Due to this issue, drawing the figure of merit ZT becomes a problematic task.

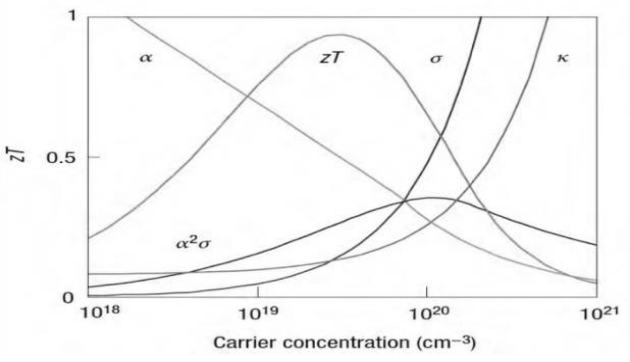

Figure 4. The ZT of Bi_2Te_3 as function of carrier concentration, where α, σ, κ represent the Seebeck coefficient, electrical conductivity, and thermal conductivity, respectively. The $\alpha^2\sigma$ value designates the power factor, and ZT represents the thermoelectric figure-of-merit [2] .

Figure 4 depicts the optimized figure of merit ZT as a function of carrier concentration of Bi_2Te_3 [2]. The maximum possible values for the figure of merit ZT lie between 10^{18} to 10^{21} cm^{-3} carrier concentration. The stated values are the same as for sufficiently doped semiconductor. Materials exhibiting these values can be potential candidates for thermoelectric devices [2].

As the constituents of ZT are quite conflicting in nature, there has been slow advancement regarding thermoelectric devices. The suitable materials available to be utilized as thermoelectric surfaces are composed of bismuth telluride alloys, which exhibit a figure-of-merit $ZT \approx 1.0$ [3]. Thermoelectric coolers exhibiting a ZT value of approximately 1 illustrate a Carnot efficient of about 10% [8], where 90% of the energy remains unutilized. Keeping into consideration that a household refrigerator is operated at a Carnot efficient of approximately 45%, the improvement in thermoelectric materials is inevitable if they are to transform into viable choices. Thus, the goal in this work is to obtain higher ZT values using different materials such as new bulk and two-dimensional materials.

Chapter 2: Background

2.1 Thermoelectric Properties of three-dimensional Materials

Most conducting materials exhibit thermoelectric effects, although such materials may not be regarded as real thermoelectric materials until their ZT value is more than 0.5. The temperature range at which the figure-of-merit is optimized classifies thermoelectric materials into three categories: low, moderate, and high. Low temperature materials are capable of operating up to 450 K, intermediate temperature materials are capable of operating between 450 and 850 K, and high temperature materials are capable of operating up to 1300 K [2]. This work focused on find low to high temperature thermoelectric materials that can be used for clean, long-lasting, and environmentally friendly energy generation and refrigeration. Bismuth telluride

alloys are currently the most effective low-temperature available thermoelectric materials. These alloys have maintained their position for the past two decades[1]. However, this study is focused on three-dimensional metal oxides and quaternary Heusler alloys to improve the performance of the thermoelectric properties at elevated temperatures.

2.1.1 The thermoelectric properties of metal oxides

The thermoelectric characteristics of many materials have been extensively explored during the last few decades. However, the majority of these materials have several disadvantages, including low antioxidation in air, scarcity of resources, high processing costs, and toxicity, such as Bi_2Te_3 and PdTe [9][10]. Oxides, on the other hand, have the potential to overcome these issues due to their outstanding thermal and chemical stability, abundance, low-cost manufacturing, and nontoxicity [11],[12]. Cobalt oxides like ($NaCo_2O_4$ and $Ca_3Co_4O_9$), transparent conductivity oxides like (In_2O_3), perovskite oxides like ($SrTiO_3$ and $CaMnO_3$), CdO, and ZnO are all considered potential thermoelectric materials. For example, CdO has a very high electrical conductivity [13] and it outperforms more than other n-type oxides at high temperatures with a ZT value of 0.34 at 1000 K [14]. Furthermore, Sc-doped ZnCdO, namely, $Zn_{0.9}Cd_{0.1}Sc_{0.01}O_{1.03}$ has a ZT value of 0.3 at 1173 K [12].

2.1.2 Thermoelectric properties of Heusler alloys

Heusler alloys have recently gained substantial interest as potential candidates for spintronics and thermoelectric applications. Heusler alloys are classified into four categories: full Heusler alloys (FHA), half-Heusler alloys (HHA), quaternary Heusler alloys (QHAs), and inverse Heusler alloys. The FHAs have the chemical formula (X_2YZ) and are composed of four interpenetrating cubic lattices in which X and Y are transition metals and Z is an *sp* element (main group element). When Y has a lower valence number than X, the corresponding alloy has

the space group $Fm\overline{3}m(no.225)$ and crystallizes in the L_{21} structure[15]. Meanwhile, they have the so-called XA crystal structure when the valence number of the X element is smaller than that of the Y element, which are referred to as inverse Heusler alloys with the space group $F\overline{4}3m$ [16]. However, the HHAs possess the chemical composition (XYZ), which consists of three interpenetrating cubic lattices and one empty lattice. They have C_{1b} crystal structure and $F\overline{4}3m$ space group [17]. QHAs, on the other hand, possess the chemical formula XX′YZ, a LiMgPdSb-type crystal structure, and a space group of $\overline{4}3m$ (#216) [18]. QHAs have garnered considerable interest owing to their unusual electrical, magnetic, and thermoelectric characteristics. Previous studies predicted power factor values of 2.3μW/mk^2 and 0.83μW/mk^2 for FeRhCrSi and FeRhCrGe QHAs, respectively[19]. Another study predicted a high *ZT* value of 0.8 for CrVNbZn QHAs in the temperature range of between 360K to 750K [20]. Additionally, some studies showed that some quaternary Heusler alloys showed a perfect spin-polarization of 100% and half-metallic behavior such as FeMnScAl, FeMnScGa, and FeMnScIn QHAs [21], which make them promising materials for spintronic application, spin injector, spin-valve application, and magnetic tunnel junction. This work is focused on some similar quaternary Heusler alloys which are presented in chapters 5, 6, and 7.

2.2 Thermoelectric Properties of two-dimensional Materials

The unusual physical and chemical features of two-dimensional monolayer materials have prompted considerable interest in recent years[22]. Due to the varied scattering mechanisms for phonons, low-dimensional materials may perform better thermoelectrically than their bulk counterparts [23], [24]. The study of low-dimensional thermoelectric materials response has become a prominent issue in the scientific world. For instance, graphene, a two-dimensional (2D) carbon material with exceptional features such as high charge carrier mobility, mechanical

strength, thermal conductivity, and chemical inertia, has been extensively utilized in a variety of relevant applications [25], [26], [27]. In the case of graphene, its functioning has been severely restricted since it possesses zero band gap. As a result, substantial research in nanoscience and nanotechnology has been conducted on the opening of the graphene band gap and the searching for novel 2D materials[28], [29], [30].

2.2.1 Thermoelectric properties of two-dimensional chalcogenide monolayers

Recently, two-dimensional (2D) chalcogenides such as GeSe, GeS, SnSe, and SnS have attracted considerable interest due to the similarity of their crystal structure and electrical characteristics to phosphorene[31]. Since one of its bulk equivalents, the intriguing prospect of studying their prospective use in the thermoelectric area has been frequently highlighted. The SnSe single crystal has an inherently low thermal conductivity of less than 0.25 $W.m^{-1}K^{-1}$ at 800 K[32] and a ZT of 1.7 [33]. Furthermore, some studies have established that the chalcogenides monolayers of GeSe and SnSe are suitable candidates for thermoelectric applications. The lattice thermal conductivity of GeSe monolayer was relatively higher than that of SnSe monolayer at room temperature. Thus, the *ZT* value of GeSe (*ZT*=1.99) monolayer was reported a little lower than SnSe (ZT=2.63) monolayer [34],[35]. The 2D chalcogenides have motivated scientists to investigate their thermoelectric properties. This work also is focused on chalcogenide monolayer materials such as InTe monolayer.

Chapter 3: Calculation Methodology

3.1 Quantum theory

Electrons are crucial for heat and electrical transmission in materials. Without quantum theory, it is difficult to study the behavior of electrons in a material. This chapter discusses the applications of quantum theory, as well as the connection between quantum mechanics and the Boltzmann transport theory.

3.1.1 Schrödinger equation

The wave function is a concept in quantum mechanics that explains the quantum states of a system of particles. The probability of a particle being at a particular position in space and time is described by the wave function of that particle. The solution of the Schrödinger equation is required to determine the wave function of a system. The time-dependent Schrödinger equation of a many-body system can be expressed as:

$$i\hbar \frac{\partial \Phi(r,R,t)}{\partial t} = -\frac{\hbar^2}{2\mu}\nabla^2\Phi(r,R,t) + V\Phi(r,R,t), \qquad \text{Equation2}$$

Here ħ, Φ, μ, and V are the Plank constant, wavefunction, reduce mass, and potential, respectively. This can be reduced to a time-independent Schrödinger equation as follows:

$$\hat{H}\Phi(r,R) = E\Phi(r,R) \qquad \text{Equation3}$$

Here $\hat{H}$ represents to the Hamiltonian operator and E refers to the energy. The Hamiltonian operator is given as $\hat{H} = \hat{T}_e + \hat{T}_N + \hat{V}_{ee} + \hat{V}_{eN} + \hat{V}_{NN}$, where $\hat{T}_e$ and $\hat{T}_N$ are the kinetic energy of an electron and the nuclei, respectively, and $\hat{V}_{ee}, \hat{V}_{eN}, and\ \hat{V}_{NN}$ are the potential energy of electron-electron, electron- nucleus, and nucleus-nucleus interactions, respectively. The $\hat{T}_e$ and $\hat{T}_N$ are given as:

$$T_e = \sum_{l=1}^{N} \frac{\hbar^2}{2m_i}\left(\frac{\partial^2}{\partial x_i^2} + \frac{\partial^2}{\partial y_i^2} + \frac{\partial^2}{\partial z_i^2}\right) \quad \text{Equation4}$$

$$T_N = \sum_{I=1}^{N} \frac{\hbar^2}{2M_I}\left(\frac{\partial^2}{\partial x_I^2} + \frac{\partial^2}{\partial y_I^2} + \frac{\partial^2}{\partial z_I^2}\right), \quad \text{Equation5}$$

Here *i* and I index are the electron and nuclei number, respectively; m_i and M_I are the mass of the electron and nucleus, respectively. Moreover, the $\hat{V}_{ee}, \hat{V}_{eN}, and\ \hat{V}_{NN}$ are expressed as:

$$V_{ee} = \frac{1}{2}\sum_i^N \sum_j^N \frac{e^2}{|r_i - r_j|} = \frac{1}{2}\sum_{i>j} \frac{e^2}{r_{ij}} \quad \text{Equation6}$$

$$V_{eN} = -\sum_l^M \sum_i^N \frac{Z_I e^2}{|R_I - r_i|} = -\sum_I^M \sum_i^N \frac{Z_I e^2}{r_{Ii}} \quad \text{Equation7}$$

$$V_{NN} = \frac{1}{2}\sum_i^N \sum_j^N \frac{e^2}{|r_i - r_j|} = \frac{1}{2}\sum_{i>j} \frac{e^2}{r_{ij}} \quad \text{Equation8}$$

Where e, and Z correspond to the electron charge, and charge of the nucleus, respectively. The Hamiltonian operator equation is a complicated equation with several components that cannot be solved precisely. However, it is only applicable to basic issues such as the hydrogen atom. The application of various approximations is therefore required in order to solve this problem. The next section will cover certain approximations to simplify the Schrödinger equation.

3.1.2 Born-Oppenheimer Approximation

The Born-Oppenheimer assumption assumes that nuclei remain static due to the fact that the mass of a proton is four orders of magnitude more than the mass of an electron. If nuclei are assumed static, the problem may be simplified to the electronic component, which theoretically implies disregarding kinetic energy of nuclei and potential energy of the nucleus-nucleus interaction due to the large mass of nuclei in their denominators. The many-body problem can be

reduced to a many-electron problem using the Born-Oppenheimer approximation, and the Hamiltonian can be reduced as:

$$\hat{H}_e = \hat{T}_e + \hat{V}_{ee} + \hat{V}_{eN} \qquad \text{Equation9}$$

where $\hat{H}_e$ is the Hamiltonian of the electronic part. Thus, the total energy of ground state (E_0) can be written as $E_0 = \langle \Psi_0 | H_e | \Psi_0 \rangle + V_{NN}$, where Ψ_0 represents the wavefunction of the electronic ground state. This equation remains difficult to solve for a system with a large number of particles due to the presence of a large number of electrons. So, two approximation techniques are utilized to address this problem. The first is Hartree-Fock theory, while the second is density functional theory.

3.1.3 Hartree and Hartree-Fock Approximations

Hartree found the first approximation for converting the many-body to a one-body problem by taking the system wavefunction as the product of the electronic wavefunctions. Therefore, the wavefunction of the many-body system is represented in its general form as: $\psi(\vec{r}_1, \dots, \vec{r}_N, S_1, \dots, S_N)$, here $\vec{r}$ and S represent to the position and the spin of electron, respectively. Consider a two-body system for simplicity, where the entire wavefunction system is expressed as:

$$\Psi(\vec{x}_1, \vec{x}_2) = \psi_1(\vec{x}_1)|S_1\rangle \psi_2(\vec{x}_2)|S_2\rangle, \qquad \text{Equation10}$$

This equation, however, is a symmetric wavefunction, which fails the Pauli exclusion principle for electrons supposed to be fermions. This failure was corrected in the development of the Hartree-Fock approximation, which addressed the problem by representing the wave function as a combination of Hartree products:

$$\Psi(\vec{x}_1,\vec{x}_2)=\frac{1}{\sqrt{2}}\{\psi_1(\vec{x}_1)|S_1\rangle\psi_2(\vec{x}_2)|S_2\rangle - \psi_1(\vec{x}_2)|S_2\rangle\psi_2(\vec{x}_1)|S_1\rangle\} \quad \text{Equation11}$$

$$\Psi(\vec{x}_1,\vec{x}_2)=\frac{1}{\sqrt{2}}\begin{vmatrix}\psi_1(\vec{x}_1)|S_1\rangle & \psi_2(\vec{x}_1)|S_1\rangle\\ \psi_1(\vec{x}_2)|S_2\rangle & \psi_2(\vec{x}_2)|S_2\rangle\end{vmatrix} \quad \text{Equation12}$$

ΨWhen the two-particle system is extended to a many-body system, the wavefunction becomes:

$$\Psi(\vec{x}_1,\vec{x}_2) = \frac{1}{\sqrt{N!}}\begin{vmatrix}\psi_1(\vec{x}_1)|S_1\rangle & \psi_2(\vec{x}_2)|S_2\rangle & \dots & \psi_1(\vec{x}_N)|S_N\rangle\\ \psi_1(\vec{x}_2)|S_2\rangle & \psi_2(\vec{x}_2)|S_2\rangle & \dots & \psi_2(\vec{x}_N)|S_N\rangle\\ \vdots & \vdots & & \vdots\\ \psi_N(\vec{x}_1)|S_1\rangle & \psi_N(\vec{x}_2)|S_2\rangle & \dots & \psi_N(\vec{x}_N)|S_N\rangle\end{vmatrix} \quad \text{Equation13}$$

ΨEvery one of these wave functions is obtained by solving the Schrödinger equation as follows:

$$\left(-\frac{\hbar^2}{2m}\nabla_i^2+V\right)\psi_i(\vec{r})=E_i\psi_i(\vec{r}) \quad \text{Equation14}$$

Here V represents to the effective potential, which encompasses the electron-electron ($V_{ee}(r)=-\frac{Ze^2}{|\vec{r}|}$), exchange ($V_x(r)=-e^2\sum_{j,i\neq j}\int\frac{\psi_i(\vec{r}_2)^*\psi_i(\vec{r}_2)}{|\vec{r}_1-\vec{r}_2|}d\vec{r}_2$) potentials and electron-ion ($V_{eN}(r)=e^2\sum_{i\neq j}\int\frac{|\psi_i(\vec{r}_2)|^2}{|\vec{r}_1-\vec{r}_2|}d\vec{r}_2$). For atoms and molecules, the Hartree-Fock approximation is helpful. It is, however, computationally costly, and less precise for materials with many electrons.

3.1.4 Density Functional Theory (DFT)

According to the basics of quantum mechanics, the wavefunction (Ψ) comprises all the information about the system such as energy, momentum, particle density and position [36]. The Ψ can be calculated by inserting a potential ν(r) into the Schrödinger equation, and then solving

for the Ψ. This is alike for both single-and many-body system: the only difference is the choice of the potential v(r) and the complexity it can create. For a single-body system, the Schrödinger equation is expressed as [37]:

$$\left[-\frac{\hbar^2\nabla^2}{2m}+v(\mathbf{r})\right]\Psi(\mathbf{r})=\varepsilon\Psi(\mathbf{r}) \qquad \text{Equation15}$$

Here ħ, m, $v(\mathbf{r})$, ε and Ψ refer to Planck's constant, the mass of particle, potential, energy, and wave function, respectively. In many- body system, the Schrödinger equation is demonstrated as[36]:

$$\left[\sum_i^N\left(-\frac{\hbar^2\nabla^2}{2m}+v(\mathbf{r}_i)\right)+\sum U\left(\mathbf{r}_i,\mathbf{r}_j\right)\right]\Psi(\mathbf{r}_1,\mathbf{r}_2\ldots,\mathbf{r}_N)= E\Psi(\mathbf{r}_1,\mathbf{r}_2\ldots,\mathbf{r}_N), \qquad \text{Equation16}$$

where N and $U\left(\mathbf{r}_i,\mathbf{r}_j\right)$ refer to the number of electrons and the electron-electron interaction. All observables can be obtained by obtaining the expectation value of an operation and utilizing the wave function provided by the Schrödinger equation.

In the case of many- body Schrödinger equation, the addition of electron-electron interactions makes it more difficult and time consuming to solve. Computational power today is unable to solve the Schrödinger equation for many- body system with more than a few hundred electrons [37]. Another approach is to use density functional theory to reduce the many- body system issue to a single- body system by removing all electron-electron interactions. To make this possible, the Hohenberg-Kohn (HK) [38] theorem and the Kohn-Sham (KS) [39] scheme are used.

According to the Hohenberg-Kohn theorem, the non-degenerate ground-state energy is a function of the ground-state charge density ($n_0(r)$). Since the wave function includes all of the

information about a system, every ground-state operation is a functional of the ground-state density:

$$O_0[n_0] = \langle \Psi_0[n_0] | \hat{O}_0 | \Psi_0[n_0] \rangle \qquad \text{Equation17}$$

Here O_0 refers to the general observable and $\hat{O}_0$ represents to the operator that utilized to get O_0. The first Hohenberg-Kohn theorem is represented by Equation 17. A more particular observation seems to be the ground-state energy of a potential system v:

$$E_{v,0} = E_v[n_0] = \langle \Psi_0[n_0] | \hat{H} | \Psi_0[n_0] \rangle \qquad \text{Equation18}$$

From this equation, the expectation value of the Hamiltonian with respect to the ground-state wavefunction Ψ_0 is used to calculate the ground-state energy E_0. The Ψ_0 must not only recreate the density of the ground state, but it must reduce the energy as follows:

$$E_{v,0} = \min_{\Psi \to n_0} \langle \Psi_0[n_0] | \hat{H} | \Psi_0[n_0] \rangle \qquad \text{Equation19}$$

The energy operation refers to the Hamiltonian ($\hat{H}$): $\hat{H} = \hat{T} + \hat{U} + \hat{V}$

$$E_{v,0} = \min_{\Psi \to n_0} \langle \Psi_0[n_0] | \hat{T} + \hat{U} + \hat{V} | \Psi_0[n_0] \rangle \qquad \text{Equation20}$$

The $\hat{T}$ and $\hat{U}$ are the kinetic energy and the electron-electron interaction, respectively, which are independent of the potential $\hat{V}$. Consequently, just the potential with regard to the particle density has to be specified. This leads to simplify equations 19 and 20:

$$E_{v,0} = \min_{\Psi \to m_0} \langle \Psi_0[n_0] | \hat{T} + \hat{U} | \Psi_0[n_0] \rangle + \int d^3 r n(\mathbf{r}) v(\mathbf{r}) \qquad \text{Equation21}$$

The right side of equation 15 is divided into two sections by the variational principle, which distinguishes the independence of the potential energy from the kinetic energy and electron-electron interactions.

The Hohenberg-Kohn theorem further asserts that computing the expectation values of the Hamiltonian with respect to Ψ other than the Ψ_0 always yields values greater than the ground state energy. This means that when the energy is determined using the trial density n′, where $n_0 \neq n'$, a value less than the energy of ground state E_0 is not attainable. Equation 16 expresses this principle, which is referred as the second Hohenberg-Kohn theorem.

$$E_v[n_0] \leq E_v[n'] \qquad \text{Equation22}$$

Due to the fact that the wavefunction and hence all observables are functionals of particle density, the Hohenberg-Kohn theorem gives a means to bypass the many-body Schrödinger equation. Even with this simplifying assumption, the electron-electron interaction issue remains. Walter Kohn and Lu Jeu Sham suggested an approach that simplifies the computation of desired observables further by translating the original interacting system onto a non-interacting system while retaining the electron density. This enables a systematic mapping of the many-body issue including U to the single-body problem omitting U [39]. The energy functional for a non-interacting system appears to be as follows:

$$E_S[n] = \langle \Psi | \hat{T}_S + \hat{V}_S | \Psi \rangle \qquad \text{Equation23}$$

Here;

$$\hat{T}_S + \hat{V}_S = \hat{T} + \hat{U} + \hat{V} \qquad \text{Equation24}$$

T_S represents to the kinetic energy of a non-interacting system and V_S refers to the external effective potential, which is known as the Kohn-Sham potential. The external effective potential is given as: $v_S = v + v_H + v_{XC}$, where v is the many-body potential, v_H is the Hartree potential that defines the electron-electron Coulomb repulsion, and v_{XC} is exchange-correlation potential, which expresses the relationship between the exchange-correlation energy and the charge density. As a result, for the single-body system, the Schrödinger equation can be written as:

$$\left[-\frac{\hbar^2\nabla^2}{2m} + v_S(\vec{r})\right]\Phi(\vec{r}) = \varepsilon\Phi(\vec{r}) \qquad \text{Equation25}$$

Here, $\Phi(\vec{r})$ is the Kohn-Sham wavefunction that depicts the electronic states of a fictional non-interacting system. The Hohenberg-Kohn theorem avoids solving the Schrödinger equation by minimizing the functional E[n], but the Kohn-Sham theorem solves a modified, non-interacting Schrödinger equation. Within DFT method, the charge density of the non-interacting system, determined with the single-body system, reproduces the charge density of the interacting system as follows:

$$n(\vec{r}) \equiv n_S(\vec{r}) = \sum_{i}^{N} f_i|\Phi_i|^2 \qquad \text{Equation26}$$

where f_i refers to the occupation of the ith orbital. This assumption enables DFT to be a highly effective method for computing binding energies in chemistry and electronic structure in physics.

The ground-state ionic structure, band structure, and electronic density-of-states are all determined in this research using density functional theory. The first step in calculating the electronic structure is to find the crystal structure with the minimum energy. The Hohenberg-Kohn theorem demonstrates the necessity of attaining the minimal energy structure; the structure that reduces energy $E_{v,0}$ corresponds to the structure that gives the ground-state charge density n_0.

The ground state electronic structure is computed using the n_0 of the minimal energy structure. After the minimal energy lattice parameters are determined, the electronic structure may be calculated using a converged self-consistent charge density. The band structure determines the energy as a function of the band number *n* and the wave vector *k*, *E*. (*n*, *k*). Vibrational energies, carrier density, and group velocity are parameters that can be extrapolated from band structure data. The band structure is analyzed in this research to determine the difference between the highest valence and lowest conduction bands (band gap). The estimated density-of-states (DOS) value indicates the amount of charge carriers contained inside a particular volume throughout the infinitesimal energy range $E + \partial E$.

Several density functional codes include implementations of the Hohenberg-Kohn theorem and the Kohn-Sham equations. The Vienna Ab-initio Simulation Package, often known as VASP (pseudopotential scheme), and WIEN2K (full-electron scheme), are two of the most widely used. In this study, VASP [40][41] and WIEN2K [39] codes are utilized to calculate the electronic structures of the investigated systems. VASP and WIEN2K are versatile codes for "ab-initio quantum-mechanical molecular dynamics simulations" that use plane wave basis sets, pseudopotentials, and full potentials, respectively. In addition, they are capable of incorporating the projector-augmented technique (PAW)[42]. The computations in this work used the PAW approach with Perdew, Burke, and Ernzerhof (PBE) generalized-gradient approximation (GGA)[43].

3.2 Boltzmann Transport Theory

The Boltzmann transport theory gives a simple approach for computing the thermoelectric transport coefficients. The theory explains how a distribution function *f*(n,k) evolves under the influence of an external electric field *E* and a temperature gradient *T*. The

chance of detecting an electron in band *n* with a wave vector *k* is given by this distribution function *f*(n,k). The Boltzmann equation is expressed as [44]:

$$-\left(\frac{\partial f^0(n,\vec{k})}{\partial \varepsilon(n,\vec{k})}\right)\vec{v}(n,\vec{k})\left[\frac{\varepsilon(n,\vec{k})}{T}\nabla T + e\vec{E} - \nabla\propto\right] = -\left(\frac{\partial g(n,\vec{k})}{\partial t}\right)_{SC} \quad \text{Equation27}$$

Here $\partial f^0(n,\vec{k})$, $\varepsilon(n,\vec{k}), \vec{v},$ T, e, E, and μ represent to the equilibrium distribution function, the electron energy in band (*n*) with wave vector $\vec{k}$, the electron velocity in band (*n*) with wave vector $\vec{k}$, the gradient temperature, the electron charge, the external electric field, and the chemical potential, respectively. The $g(n,\vec{k})$ means the $f(n,k) - f'(n,k)$. The constant relaxation time approximation (RTA) is used to further simplify the Boltzmann equation. The relaxation time is considered to be position-and velocity-independent in this approximation. The relaxation time is the time required for an electron distribution to go from a nonequilibrium condition to an equilibrium Fermi distribution. The Boltzmann transport equation can be expressed within the RTA as [44]:

$$-\left(\frac{\partial f^0(n,\vec{k})}{\partial \varepsilon(n,\vec{k})}\right)\vec{v}(n,\vec{k})\left[\frac{\varepsilon(n,\vec{k})}{T}\nabla T + e\vec{E} - \nabla\propto\right] = -\frac{g(n,\vec{k})}{\tau} \quad \text{Equation28}$$

In this instance, the RTA has been substituted for the right side. Due to the fact that $g(n,\vec{k})$= $f(n,k) - f'(n,k)$, it can be solved for $f(n,k)$. Boltzmann equation terms can be derived using the data of band structure $\varepsilon(n,\vec{k})$, where the velocity *v*(*n*,*k*) can be expressed as:

$$\vec{v}(n,\vec{k}) = \frac{1}{\hbar}\left(\frac{\partial \varepsilon(n,\vec{k})}{\partial \vec{k}}\right) \quad \text{Equation29}$$

Once the nonequilibrium distribution function $f(n,k)$ is defined, the thermoelectric parameters can be computed using the Onsager relations for electrical current density(J) and heat current density(J_Q), which can be expressed as:

$$J = -\frac{16\pi e\sqrt{2m}}{3h^3}\int E^{3/2}\tau(E)\frac{\partial f_0}{\partial E}\left(\frac{E-\propto}{T}\nabla T + \nabla\propto + eE_0\right)dE \quad \text{Equation30}$$

$$J_Q = -\frac{16\pi\sqrt{2m}}{3h^3}\int E^{3/2}(E- \propto)\tau(E)\frac{\partial f_0}{\partial E}\left(\frac{E-\propto}{T}\nabla T + \nabla\propto + eE_0\right)dE \quad \text{Equation31}$$

And the Onsager relations can be written as [7]:

$$\vec{j} = \sigma E_0 - \sigma S\nabla T \quad \text{Equation32}$$

$$\vec{j} = \sigma S T E_0 - \kappa\nabla T \quad \text{Equation33}$$

here σ, S, E_0, κ and ∇T are the electric conductivity, Seebeck coefficient, external electric field, thermal conductivity, and temperature gradient, respectively. The thermoelectric parameters such as Seebeck coefficient (S), electrical conductivity (σ) and thermal conductivity (κ) can be calculated by [7]:

$$S = -\frac{\pi^2 k_B^2}{3e}\frac{\partial}{\partial E}\ln\left[E^{1/2}\tau(E)\right]_{E=\alpha} \quad \text{Equation34}$$

$$\sigma = \frac{ne^2\tau\left(E_f\right)}{m} \quad \text{Equation35}$$

$$\kappa = \frac{\pi^2 k_B^2}{3e^2}\sigma T \quad \text{Equation36}$$

Moreover, the electric current that is influenced by an electric field, can be given by:

$$j_i = \sigma_{ij}E_j + \sigma_{ijk}E_jB_k + v_{ij}\nabla_j T \qquad \text{Equation37}$$

$$j_i = \sigma_{ij}E_j + \sigma_{ijk}E_jB_k + v_{ij}\nabla_j T \qquad \text{Equation38}$$

σ_{ij} and σ_{ijk} represent to conductivity tensors, and E, B, $v_{ij}$and $\nabla_j T$ refer to the external electric field, magnetic field, group velocity and temperature gradient, respectively. The group velocity ($v_\alpha(i,\vec{k}) = \frac{\partial\varepsilon(i,\vec{k})}{\hbar\,\partial k_\alpha}$) and inverse mass tensor ($M^{-1}_{\beta x}(i,\vec{k}) = \frac{\partial^2\varepsilon(i,\vec{k})}{\hbar^2\,\partial k_\beta\,\partial k_\alpha}$) are two parameters of the conductivity tensor that directly employ the band structure data obtained from a DFT computation.

$$\sigma_{\alpha\beta}(i,\vec{k}) = e^2\tau v_\alpha(i,\vec{k})v_\beta(i,\vec{k}) \qquad \text{Equation39}$$

$$\sigma_{\alpha\beta\gamma}(i,\vec{k}) = e^3\tau^2\zeta_{\gamma uv}v_\alpha(i,\vec{k})v_\beta(i,\vec{k})M^{-1}_{\beta u} \qquad \text{Equation40}$$

τ and $\zeta_{\gamma uv}$ are the relaxation time within RTA and the Levi-Civita symbol [45], respectively. If any of these parameters γuv are equal, the $\zeta_{\gamma uv}$equals zero otherwise equals ±1 based on the permutation direction. Following that, the transport tensors are derived using the conductivity distributions $f_\mu(T,\varepsilon)$ generated by the Boltzmann transport equation[46]:

$$\sigma_{\alpha\beta}(T;\propto) = \frac{1}{\Omega}\int \sigma_{\alpha\beta}(\varepsilon)\left[-\frac{\partial f_\alpha(T;\varepsilon)}{\partial\varepsilon}\right]d\varepsilon \qquad \text{Equation41}$$

$$v_{\alpha\beta}(T;\propto) = \frac{1}{eT\Omega}\int \sigma_{\alpha\beta}(\varepsilon)(e-\propto)\left[-\frac{\partial f_\alpha(T;\varepsilon)}{\partial\varepsilon}\right]d\varepsilon \qquad \text{Equation42}$$

$$\kappa^{\text{elec}}_{\alpha\beta}(T;\propto) = \frac{1}{e^2T\Omega}\int \sigma_{\alpha\beta}(\varepsilon)(e-\propto)^2\left[-\frac{\partial f_\alpha(T;\varepsilon)}{\partial\varepsilon}\right]d\varepsilon \qquad \text{Equation43}$$

$$\sigma_{\alpha\beta\gamma}(T;\infty) = \frac{1}{\Omega}\int \sigma_{\alpha\beta\gamma}(\varepsilon)\left[-\frac{\partial f_\alpha(T;\varepsilon)}{\partial \varepsilon}\right] d\varepsilon \qquad \text{Equation44}$$

$$S_{ij} = E_i\left(\nabla_j T\right)^{-1} = (\sigma^{-1})_{\alpha i} v_{\alpha j} \qquad \text{Equation45}$$

here κ^{elec}, Ω, and f_α are the electronic part of thermal conductivity, volume element, and distribution function.

Chapter 4: Investigations of the electronic, dynamical, and thermoelectric properties of $Cd_{1-x}Zn_xO$ alloys

1. Introduction

The increasing demand for energy resources due to the industrial leap and the limitation of fossil fuel resources as well as their environmental concerns leads to the needs of alternative resources. These resources should be renewable and environmentally friendly. One of these alternative resources is generated using thermoelectric (TE) devices that could convert thermal energy directly into electrical energy or vice versa by Seebeck and Peltier effects, respectively [47],[48]. The efficiency of these TE materials is measured by the figure of merit:

$$ZT = S^2\sigma T/(\kappa_e + \kappa_L) \quad \text{Equation46}$$

where S, σ, T, κ_e and κ_L refer to the Seebeck coefficient, electrical conductivity, absolute temperature, electronic thermal conductivity, and lattice thermal conductivity, respectively. High ZT values require high values of Seebeck coefficient and electrical conductivity, and low thermal (electronic and lattice) conductivity [49]. Unfortunately, it is a difficult task to meet all of these parameters in one material. They are interdependent since a high Seebeck coefficient requires low carrier concentrations that leads to low electrical conductivity. This behavior can be explained by the mathematical formulae that relate the Seebeck coefficient and the electrical conductivity to the carrier concentration as follows [50],[51]:

$$S = \left(\frac{8\pi^{\frac{2}{3}}k_B^2\left(r+\frac{3}{2}\right)}{3^{5/3}\,eh^2}\right)\left(\frac{m^*}{n^{2/3}}\right)T \quad \text{Equation47}$$

$$\sigma = ne\mu \quad \text{Equation48}$$

Here *S, σ, k_B, r, h, m^*, n, e, and* μ refer to the Seebeck coefficient, electrical conductivity, Boltzmann constant, scattering parameter, Planck's constant, effective mass, carrier concentration, electron charge, and carriers' mobility, respectively. Hence, the Seebeck coefficient, *S*, requires a low carrier concentration, *n*, while the electrical conductivity, is directly proportional *n*. However, the high electrical conductivity, *σ,* corresponds to a high electronic thermal conductivity, κ_e, according to Wiedemann-Franz law ($\kappa_e = L\sigma T$), where *L* is the Lorentz number [52]. Therefore, one has to search for some techniques that provide the required good parameters, which lead to a high *ZT* value. Among these techniques are alloying with other elements, lowering the dimensionality and creating vacancies. Such techniques lead to an enhancement in the phonon scattering and a reduction in the lattice thermal conductivity [53] . In addition, *n*- and *p*-type doping could enhance the Seebeck coefficient and electrical conductivity [54].

In the past few decades, the thermoelectric properties have been intensively investigated for different materials. However, most of these materials have many problems, such as poor antioxidation in air, low abundance of resources, and high-cost processing and toxicity such as Bi_2Te_3 and PdTe [9], [10]. On the other hand, oxides could overcome these problems due to their excellent thermal and chemical stability, abundancy and low-cost processing and nontoxicity [48], [55]. Cobalt oxides such as $NaCo_2O_4$ and $Ca_3Co_4O_9$, transparent conductivity oxides (TCO_s) including In_2O_3, perovskite oxides such as $SrTiO_3$ and $CaMnO_3$, CdO and ZnO are considered to be promising TE materials [50],[53],[54].

Cadmium oxide (CdO) has a simple cubic rock-salt structure with a lattice parameter of 4.77 Å [14]. It is characterized as an *n*-type semiconducting material [56], [57] with a direct band gap of 2.28 eV [9] and an indirect band gap of 0.84 eV, and high carrier mobility [58]. In

addition, CdO could be a wurtzite structure with a lattice parameter of a= 3.60 Å and c/a= 1.55 Å [59]. Moreover, CdO possesses a low phonon thermal conductivity due to its low Debye temperature ($\theta_D \sim 255$K) [58]. Furthermore, the nonstoichiometric structure of CdO exhibits an excellent electrical conductivity [60]. At a high temperature, some investigations reported an excellent TE performance of CdO as compared to other *n*-type oxides with *ZT* value of 0.34 at 1000 K [13]. The *ZT* value could be enhanced to 0.45 by doping CdO with a 3% concentration of Zn at 1000K [13]. The choice of this doping element is due to the similarity of its ionic radius (0.074 nm) with that of Cd (0.095 nm) to fit in CdO matrix without causing any dislocations in the crystal [51]. In addition, other dopants such as Ba could enhance the *ZT* value to 0.47 at about 1000 K in $Cd_{0.99}Ba_{0.01}O$ alloy, which is higher than other *n*-type oxides such as $SrTi_{0.8}Nb_{0.2}O_3$ (~ 0.35 at 1000K), $Ca_{0.96}Gd_{0.04}MnO_3$ (~ 0.24 at 973 K), $Zn_{0.98}Al_{0.02}O$ (~ 0.24 at 1273 K) and $In_{1.98}Co_{0.02}O_3$ (~ 0.26 at 1073 K) [9], [58], [14].

Zinc oxide (ZnO) is also an *n*-type semiconductor with a direct wide band gap of 3.37 eV [61], [62]. It could be crystallized in wurtzite, zincblende, and rock-salt structures [63], [64]. However, the most stable structure is the wurtzite structure [64]. In addition, it has a high melting temperature of 2000 K, a high Seebeck coefficient and a good chemical stability [65]. These properties make ZnO oxides very promising for TE applications. Ohtaki *et al.* reported a good *ZT* ~ 0.47 at 1000 K and 0.65 at 1247 K for $Zn_{0.96}Al_{0.02}Ga_{0.02}O$ [66]. Jantrasee *et al.* reported a *ZT* ~ 0.28 for $ZnAl_2O_4$ at 670 K [67], whereas Ohtaki *et al*. reported a *ZT* value of 0.2 at 1000 K for $Zn_{0.98}Al_{0.02}O$ [65]. Moreover, Han *et al.* investigated TE properties of Sc-doped ZnCdO and reported a *ZT* value of 0.3 at 1173 K for $Zn_{0.9}Cd_{0.1}Sc_{0.01}O_{1.03}$ [55].

Motivated by the above-mentioned properties of oxide materials, we present the structural, dynamical, electronic, and thermoelectric properties of $Cd_{1-x}Zn_xO$ (x=0.0 - 1.0; with

an increment of 0.125) alloys in the wurtzite and rock-salt structures. The rest of the paper is organized as follows: section 2 contains the computational details, section 3 presents the results and discussion, and the main concluding points are summarized in section 4.

2. Computational methodology

The calculations are performed using density functional theory. The structural, atomic optimization and phonon investigation are performed using the projector augmented wave (PAW) method with (VASP) code [68]. Methfessel-Paxton smearing method is used with 0.2 eV smearing width to identify the partial occupancies of each wave function [39]. The chosen plane-wave cut-off energy is 520 eV with a tolerance of the total energy convergence of 10^{-7}eV. These optimized parameters are then utilized to present total energy calculations based on full-potential linearized augmented plane wave (FP-LAPW) method with WIEN2k code [69]. The Perdew–Burke–Ernzerhof Generalized Gradient Approximation (GGA-PBE)[70] was implemented for the exchange-correlation potential for the case of the energetics and structural optimization. However, the Generalized Gradient Approximation within the modified Becker-Johnson approximation (GGA-mbj) [71] functional was utilized to obtain the electronic structures. The cut-off parameter is chosen value to be $K_{max} \times R_{MT}$=8.5, where K_{max} and R_{MT} are the largest k vector in plane wave expansion and the smallest atomic muffin tin radius, respectively. The R_{MT} values were selected to be 2.4, 2.2, and 1.5 for Cd, Zn, and O, respectively. Phonon calculations were performed using phonopy package [72] with 4×4×4 supercell in the rock-salt configuration and 4×4×2 supercell in the wurtzite configuration. The thermoelectric parameters including the Seebeck coefficient, electronic thermal conductivity, and power factor are examined by utilizing Boltzmann transport theory with the BoltzTrap code [46] under constant relaxation time.

3. Results and discussion

3.1 Structural properties

Cadmium oxide binary alloy crystalizes in rock-salt structure with $Fm\bar{3}m$ (#225) space group, while ZnO has a wurtzite structure with *P63mc* (#186) space group (see Table I). The calculations of CdO in the rock-salt configuration are performed using a unit cell of two inequivalent atoms (one atom of each element; Cd and O), whereas the wurtzite configuration of ZnO binary alloy has a unit cell of four atoms (two atoms of each element; Zn and O), see Figures. 5 (a) and (b). However, the $Cd_{1-x}Zn_xO$ ternary alloys are investigated using the rock-salt configuration for concentrations less than 0.5 and wurtzite configuration for concentrations greater than 0.5. For the case of x= 0.5, both structures were considered. These ternary alloys were investigated using a 2×2×2 supercell of 16 atoms in the rock-salt configuration (Figure 5 (c)) and a 2×2×1 supercell of 16 atoms for the case of the wurtzite configuration (see Figure 5 (d)). The space groups of these alloys vary due the change of symmetry upon alloying, see Table 1. The lattice parameter of CdO in the rock-salt configuration is 4.78 Å, which is a good agreement with the experiment value (see Table I) [58]. However, the lattice parameters of the wurtzite configuration of ZnO are a=3.28 Å and c/a = 1.61, which are in a good agreement with the experiment values (see Table I) [73]. The structural parameters of the $Cd_{1-x}Zn_xO$ ternary alloys are in agreement with previous calculations [74], [75]. The lattice parameters of $Cd_{1-x}Zn_xO$ ternary alloys in the rock-salt configuration are found to decrease as Zn concentration increases, whereas the wurtzite configuration shows an increase in the lattice parameter (see Table 1).

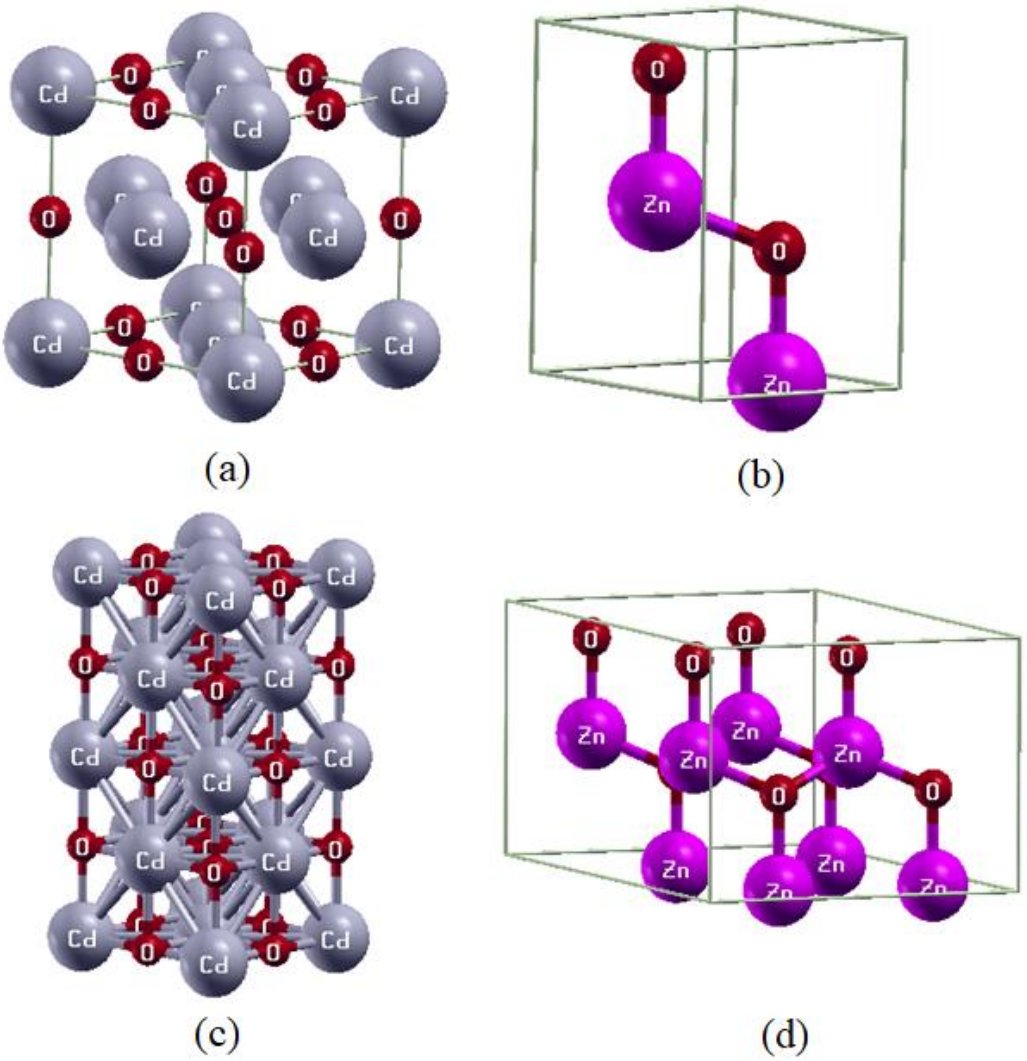

Figure 5. The unit cell of (a) CdO and (b) ZnO binary alloys. (c) The crystal structure of the 2×2×2 and (d) 2×2×1 supercell of the rock-salt and wurtzite phases.

Table 1. The structural parameters and space groups of $Cd_{1-x}Zn_xO$ (x = 0.0 – 1.0)

Structures	NaCl	WZ		Space group
	a(Å)	a(Å)	c/a(Å)	
CdO	4.78 [a]			Fm-3m(#225)
	4.79 [b]			
	4.77 [c]			
$Zn_{0.125}Cd_{0.875}O$	4.73 [a]			P4/mmm (#123)
	4.59 [b]			
$Zn_{0.25}Cd_{0.75}O$	4.72 [a]			Pm-3m (#221)
	4.55 [b]			
$Zn_{0.375}Cd_{0.625}O$	4.61[a]			Pmmm (#47)
	4.50 [b]			
$Zn_{0.5}Cd_{0.5}O$	4.54[a]			P4/mmm (#123)
	4.46 [b]			
ZnO		3.28 [a]	1.61 [a]	P63mc (#186)
		3.28 [b]	1.60 [b]	
		3.24 [c]	1.60 [c]	
$Zn_{0.875}Cd_{0.125}O$		3.33 [a]	1.60 [a]	Cm (#8)
		3.28 [b]	1.59 [b]	
$Zn_{0.75}Cd_{0.25}O$		3.35 [a]	1.62 [a]	Pm (#6)
		3.33 [b]	1.59 [b]	
$Zn_{0.625}Cd_{0.375}O$		3.41 [a]	1.62 [a]	Pm (#6)
		3.37 [b]	1.59 [b]	
$Zn_{0.5}Cd_{0.5}O$		3.44 [a]	1.65 [a]	P3m1 (#156)
		3.42 [b]	1.59 [b]	

[a] This work. [b] Theory, Ref [74], [75],[c] Exp, Ref [14], [29].

3.2 The Dynamic properties

This subsection presents the phonon dispersions relations of $Cd_{1-x}Zn_xO$ alloys in the rock-salt and wurtzite structures to investigate the dynamical stability of these alloys. The phonon dispersion curves (PDCs) of these alloys were obtained by using phonopy package as implemented in VASP code [72]. The PDCs of the binary alloys along the high symmetry path in the irreducible Brillouin zone are presented in Figure 6. The number of phonon branches in the case of CdO binary alloy are six (3N, where N=2 is the number of atoms in the unit cell) with three acoustic and three optical branches. However, the PDC of ZnO binary alloy shows twelve phonon branches (three acoustic and nine optical) due to the presence of four atoms in the

primitive unit cell. These results are in agreement with previous calculations [76]. The supercells of $Cd_{1-x}Zn_xO$ ternary alloys contain sixteen atoms in their structures that lead to 48 phonon branches (3N), see Figure7 . From this figure, one can see that most of these alloys show positive frequencies. This behavior indicates the mechanical stability of these alloys. However, the Zn concentrations of x= 0.125 and x=0.25 exhibit negative frequencies that indicates the instability of these alloys in their rock salt structure. The ternary alloy with Zn concentration of x=0.5 is found to be more stable in the wurtzite than the rock-salt configuration, which shows a small negative frequency between the Γ and X high symmetry points, see Figure 7.

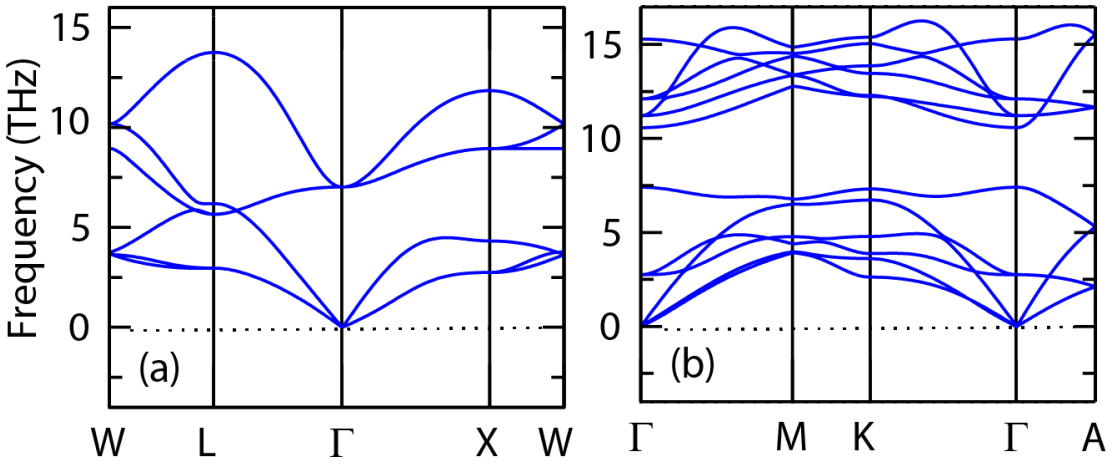

Figure 6. The phonon dispersion curves of (a) CdO and (b) ZnO binary

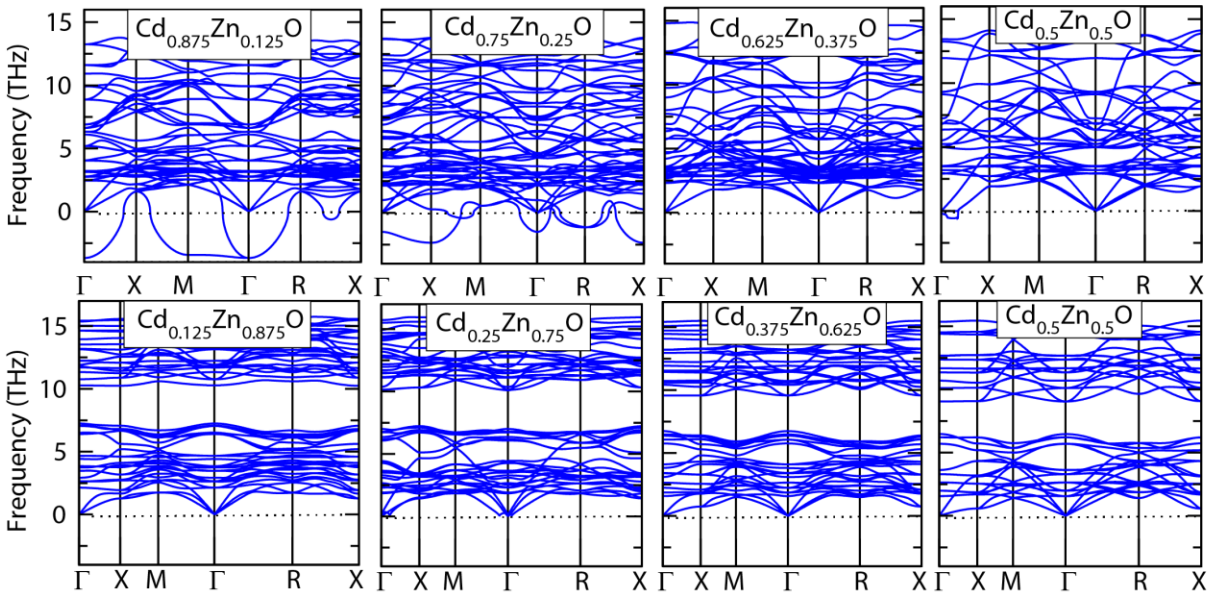

Figure 7. The phonon dispersion curves of, $Cd_{1-x}Zn_xO$ (x=0.125, 0.25, 0.375, 0.5) in its rock-salt phase (first row).and Cd1-xZnxO (x=0.5, 0.625, 0.75, 0.875) in its wurtzite configuration (second row).

3.3 The electronic properties

The electronic properties (the band structure and the density of states) were investigated for the stable structures of $Cd_{1-x}Zn_xO$ alloys. The rock-salt structure was adopted for x=0.0 and 0.375 concentrations, whereas the alloys with x= 0.5, 0.625, 0.75, 0.875, and 1.0 were investigated with the wurtzite structure. The band structures and total density of states of these alloys are presented in Figures. 8 and 9. Using the GGA-PBE functional, the rock-salt configuration of CdO shows a negative and indirect band gap of -0.501 eV between the highest valence band and the lowest conduction band at L and Γ high symmetry points, respectively (see Figure 8). However, the wurtzite configuration of ZnO exhibits a direct band gap of 0.73 eV at the Γ high symmetry point (see Figure 8). The calculated band gaps are in agreement with the previous calculations of -0.51 eV [74]and 0.75 eV [77] for CdO and ZnO alloys, respectively. However, they are underestimated as compared to the experimental values of 2.2 eV and 3.3 eV for CdO [78], and ZnO [79] respectively. The Calculations using the GGA-mbj functional,

however, shows a better agreement with the experimental values with 1.19 eV and 2.670 eV for CdO and ZnO, respectively (see Figure 8). For the case of $Cd_{1-x}Zn_xO$ ternary alloys the rock-salt structure was adopted for the concentration of x = 0.375, while the wurtzite configuration was assumed for x = 0.625, 0.75, and 0.875. The ternary alloy at the concentration of x=0.375 in the rock-salt structure exhibits a semi metallic behavior with a negative and indirect band gap of -0.074 eV, which increases to 1.62 eV using the GGA-mbj functional (see Figure. 9). However, the $Cd_{1-x}Zn_xO$ (x = 0.5, 0.625, 0.75, and 0.875) ternary alloys in the wurtzite structure exhibit a semiconducting behavior with narrow direct band gaps of 0.045, 0.178 eV, 0.332 eV and 0.526 eV at the Γ high symmetry point, respectively (see Figure 10). These band gaps are significantly increased to 1.94 eV, 2.10 eV, 2.37 eV and 2.52 eV at x = 0.5, 0.625, 0.75, and 0.875, respectively using the GGA-mbj functional (see Figure 10). Figure 6 shows that the band gap values increase upon increasing the Zn concentration. The band gap values for the stable structures of binary and ternary alloys are listed in Table 2.

The projected density of states (PDOS) of these alloys are presented in (Figures 11 and 12). Figure 11 shows a strong *p*-*d* hybridization of the most contributed O-*p* and Cd-*d* orbitals and a weak hybridization of Cd-*s* and O-*p* orbitals in the valence band in the case of CdO alloy. This is in agreement with previous calculations by Zhang *et al* [80] and Feng *et al* [80]. The valence bands of this $Cd_{0.625}Zn_{0.375}O$ alloy in the rock-salt configuration are mainly contributed by Zn-*d*, Cd-*d*, and O-*p* (see Figure 11). For the case of ZnO, the most significant contribution in the valence band comes from the Zn-*d* orbitals. The peak near the Fermi level exhibits a weak hybridization between the Zn-*s* and Zn-*d* states. These results are in a good agreement with other previous calculations [77], [75]. In the case of the wurtzite configuration the valence band of these alloys have three main regions, where the first region is mainly contributed by *d*-orbital of

Cd, followed by a second region of Zn-*d* orbital with a small contribution of different orbitals. The third region is a mixture of different orbitals (see Figure 12). The Fermi level is set to the zero point in all figures of TDOS and PDOS.

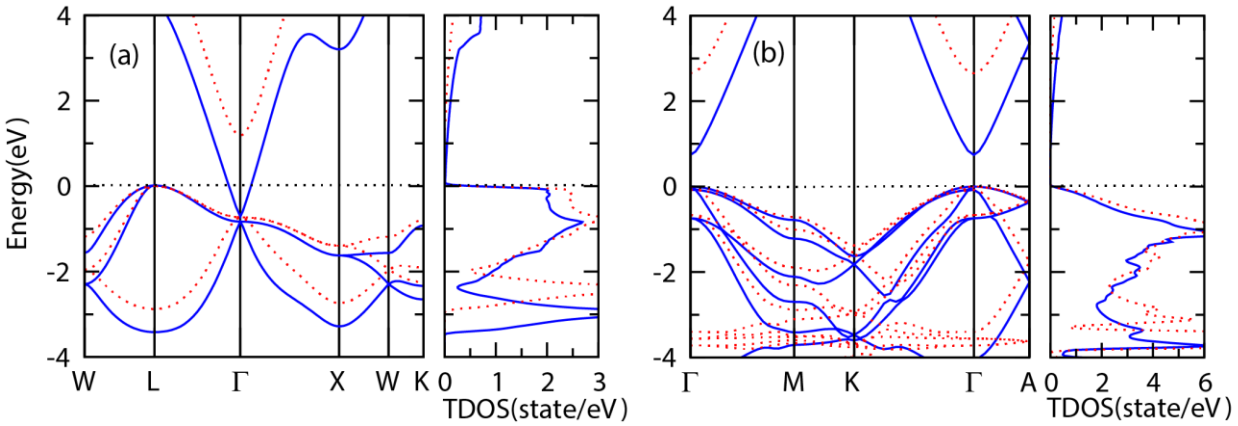

Figure 8. The electronic band structure and total density of states (DOS) of (a) CdO and (b) ZnO binary alloys using GGA-PBE (solid line) and GGA-mbj (dotted line) functionals.

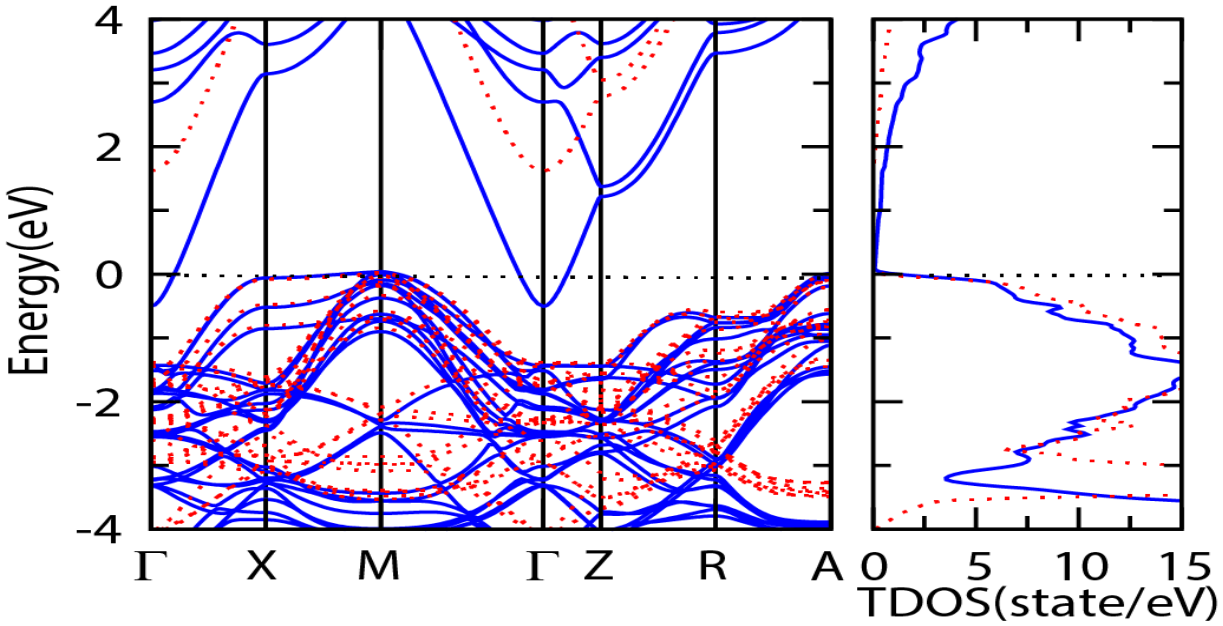

Figure 9. The electronic band structure and total density of states (DOS) of $Cd_{1-x}Zn_xO$ (x= 0.375) in its rock-salt configuration. The blue colored band indicate the GGA-PBE functional and red colored band indicate the GGA-mbj functional.

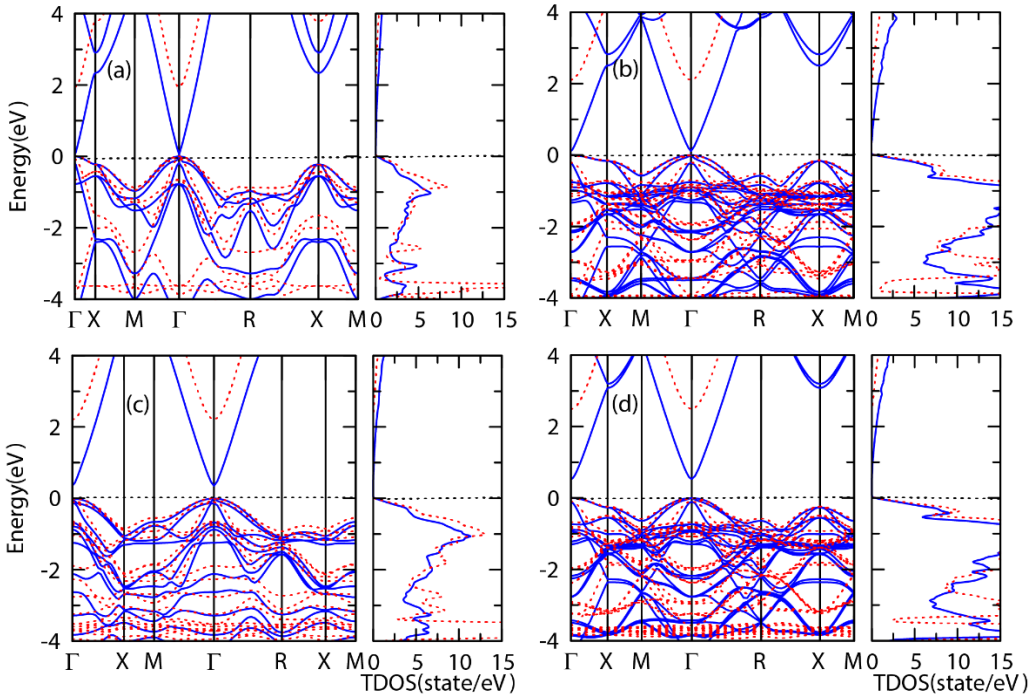

Figure 10. The electronic band structure and total density of states (DOS) of $Cd_{1-x}Zn_xO$ (x= (a) 0.5, (b) 0.625, (c) 0.75, (d) 0.875) in the wurtzite configuration using GGA-PBE (solid line) and GGA-mbj (dotted line) functionals.

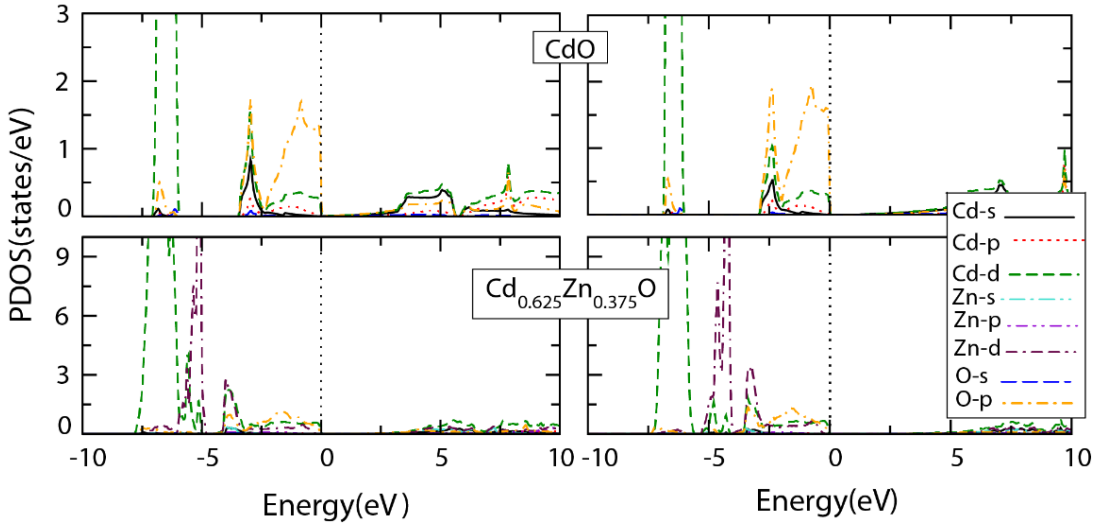

Figure 11. The projected density of states (PDOS) of $Cd_{1-x}Zn_xO$ (x=0.0, 0.375) in its rock-salt configuration using GGA-PBE functional (left column) and GGA-mbj functional (right column). The Fermi level set at zero point.

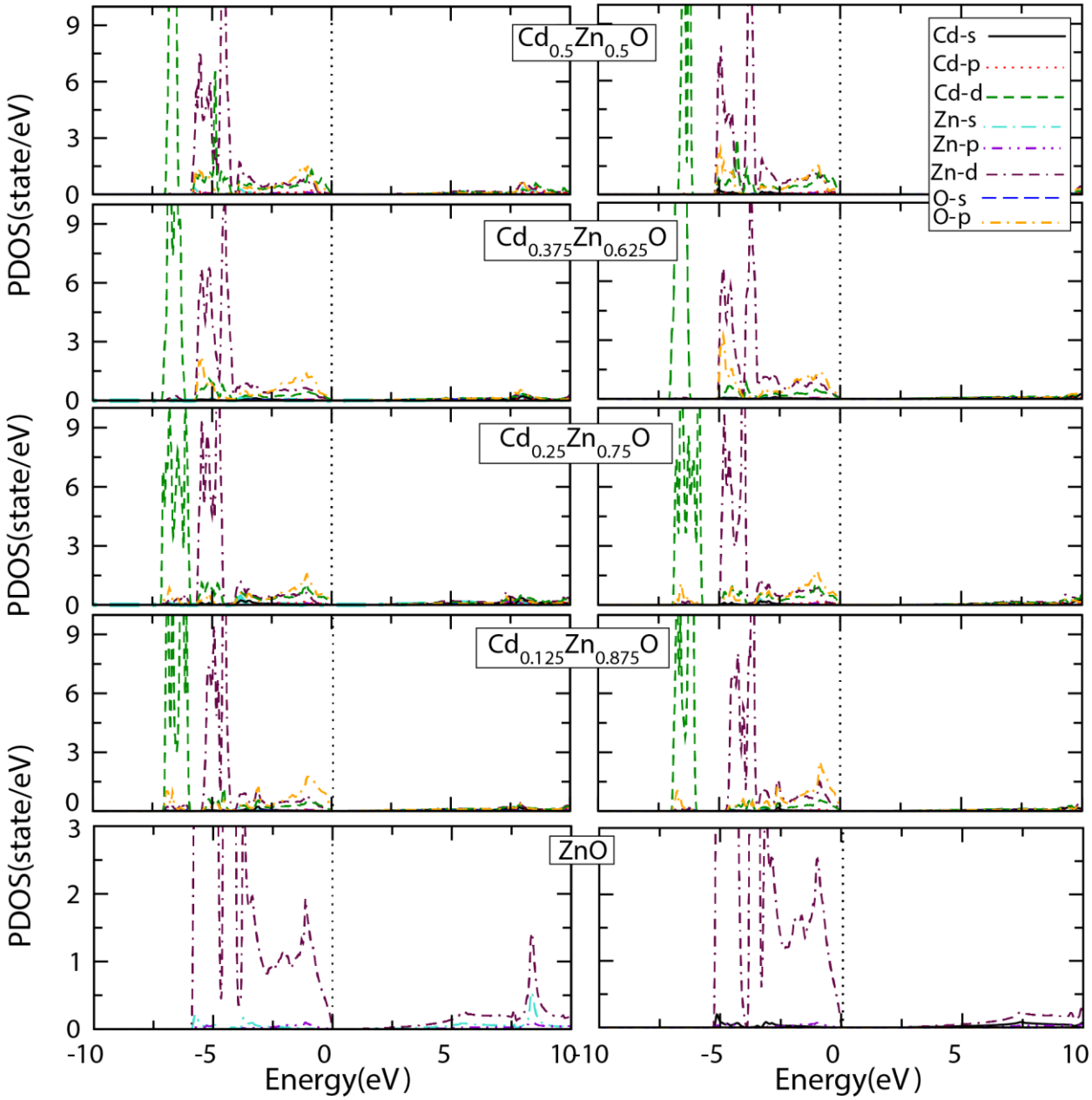

Figure 12. The projected density of states (PDOS) of ZnO and $Cd_{1-x}Zn_xO$ (x=0.5, 0.625, 0.75, 0.875, 1) in its wurtzite configuration using GGA-PBE functional (left column) and GGA-mbj functional (right column). The Fermi level set at zero point.

Table 2. The band gaps energy Eg (eV) for the stable structures of $Cd_{1-x}Zn_xO$ (x = 0.0 – 1.0) alloys.

Structures	E_g (eV)			
	Present work		Other methods	
	GGA-PBE	GGA-mbj	GGA-PBE	Experiment
CdO	-0.501	1.19	-0.51[74]	2.2 [78]
$Zn_{0.375}Cd_{0.625}O$	-0.074	1.62	----------	----------
ZnO	0.73	2.670	0.75 [77]	3.3 [79]
$Zn_{0.875}Cd_{0.125}O$	0.526	2.52	----------	----------
$Zn_{0.75}Cd_{0.25}O$	0.332	2.37	----------	----------
$Zn_{0.625}Cd_{0.375}O$	0.178	2.10	----------	----------
$Zn_{0.5}Cd_{0.5}O$	0.045	1.94	----------	----------

3.4 Thermoelectric properties:

This subsection introduces the thermoelectric properties of $Cd_{1-x}Zn_xO$ alloys in the rock-salt and wurtzite structures. The Boltzmann transport theory is used to calculate the thermoelectric properties of the Seebeck coefficient (*S*), electrical conductivity (σ/τ), electronic thermal conductivity (κ_e/τ) and power factor (PF) per relaxation time. Based on this theory, the Seebeck coefficient, electrical conductivity and electronic thermal conductivity has the following forms [81]:

$$S_{\alpha\beta}(T;\mu) = \frac{1}{eT\Omega\sigma_{\alpha\beta}(T;\mu)}\int \bar{\sigma}_{\alpha\beta}(\varepsilon)(\varepsilon - \mu)\left[-\frac{\partial f_0(T;\varepsilon)}{\partial\varepsilon}\right]d\varepsilon \qquad \text{Equation49}$$

$$\sigma_{\alpha\beta}(T,\mu) = \frac{1}{\Omega}\int \bar{\sigma}_{\alpha\beta}(\varepsilon)\left[-\frac{\partial f_0(T,\varepsilon,\mu)}{\partial\varepsilon}\right]d\varepsilon \qquad \text{Equation50}$$

$$k_{\alpha\beta}(T;\mu) = \frac{1}{e^2T\Omega}\int \bar{\sigma}_{\alpha\beta}(\varepsilon)(\varepsilon-\mu)^2\left[-\frac{\partial f_0(T;\varepsilon)}{\partial\varepsilon}\right]d\varepsilon \qquad \text{Equation51}$$

where α and β are tensor indices; μ, Ω, e, ε and f_0 are the chemical potential, unit cell volume electron charge, band energy, and the Fermi-Dirac distribution function, respectively. Here, these calculations of $S^2\sigma/\tau$, σ/τ and κ_e/τ are based on fixed relaxation time. Figures 13, and 14 present the calculated S, $S^2\sigma/\tau$ and σ/τ, values of $Cd_{1-x}Zn_xO$ alloys as a function of the chemical potential at 300 K and 1200 K for the rock-salt and wurtzite structures. Figure 13 presents the Seebeck coefficient, power factor, and electrical conductivity of $Cd_{1-x}Zn_xO$ (x=0.0, 0.375) in their stable rock-salt structures. This figure shows that the Seebeck coefficient of CdO binary alloy exhibits an *n*-type behavior, which is in a good agreement with the reported experimental result [82], whereas the $Cd_{0.625}Zn_{0.375}O$ ternary alloy possesses a *p*-type behavior. However, the power factor is found to be higher for CdO binary alloy than that of $Cd_{0.625}Zn_{0.375}O$ ternary alloy at 1200 K. In this phase, the electrical conductivity shows higher values in the *p*-type than the *n*-type doping levels. It is also noticed that the electrical conductivity exhibits high values for CdO binary alloy than those of $Cd_{0.625}Zn_{0.375}O$ ternary alloy. Figure 14 presents the Seebeck coefficient, power factor, and electrical conductivity of the $Cd_{1-x}Zn_xO$ (x= 0.50, 0.625, 0.75, 875, 1.0) in their stable wurtzite phase. From this figure, one can see that these alloys show a *p*-type behavior. It is also clear that the Seebeck coefficient has higher values at 1200 K than 300 K. In addition, the power factor per relaxation time ($S^2\sigma/\tau$) shows the higher values at 1200 K. From this figure, the electrical conductivity exhibits higher values in the *p*-type than the *n*-type doping levels. It is also noticed that the electrical conductivity is obtained to be lower for the ternary alloys. The electronic thermal conductivity κ_e/τ values of the binary and ternary alloys are presented in Figures 15 and 16. The electronic thermal conductivity values are found to be lower in the case of $Cd_{1-x}Zn_xO$ ternary alloys than those of CdO and ZnO. From the aforementioned results it is clear that the general trend of all $Cd_{1-x}Zn_xO$ structures is to have

higher values of the power factor per relaxation time ($S^2\sigma/\tau$) at higher temperatures, which indicates a higher efficiency. This behavior suggests these oxide materials as promising candidates for high-temperature thermoelectric applications.

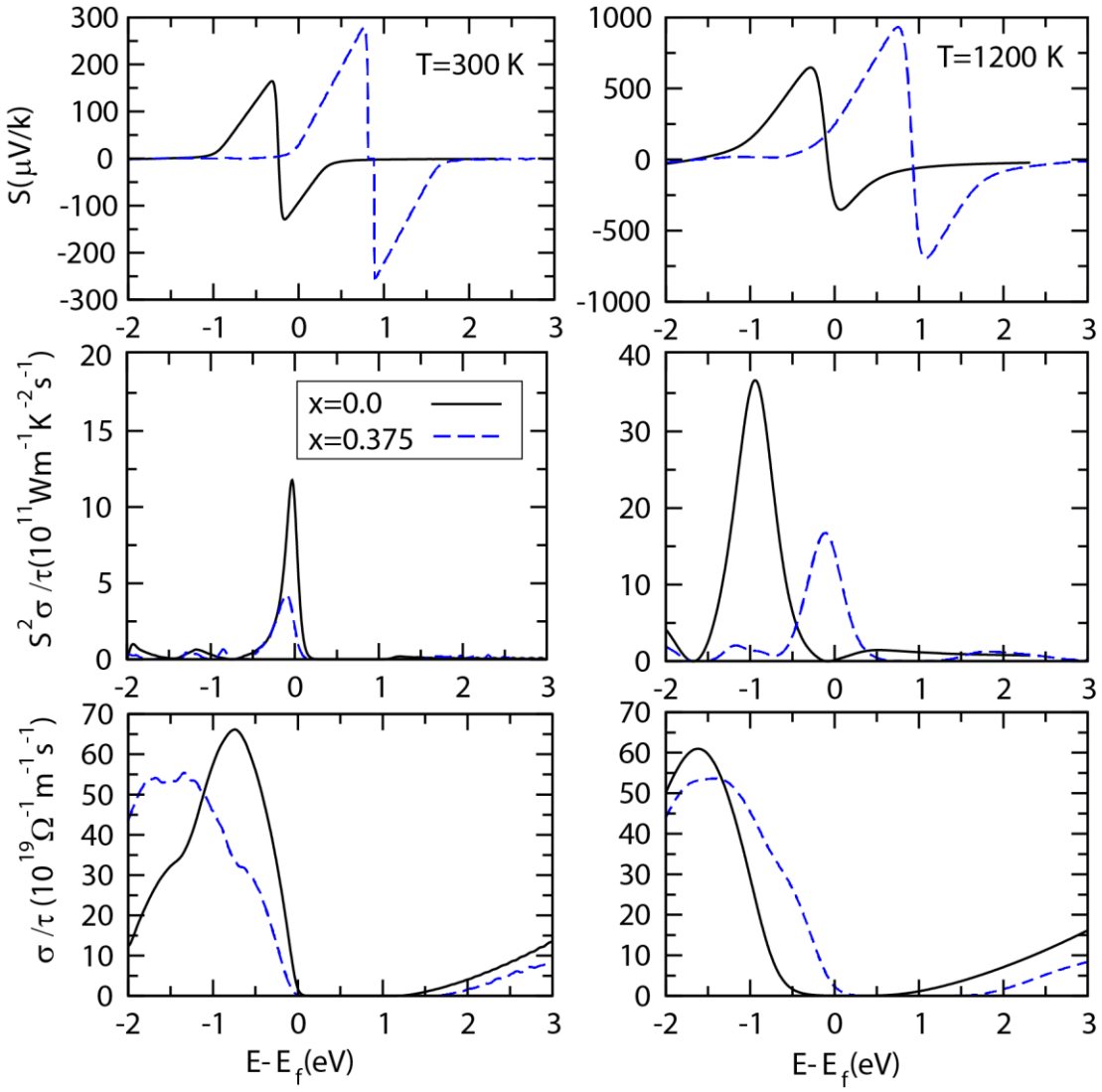

Figure 13. The Seebeck coefficient (S), power factor ($S^2\sigma/\tau$) electrical and conductivity (σ/τ) as a function of the chemical potential at 300 K and 1200 K of $Cd_{1-x}Zn_xO$ (x=0.0, 0.375) in its rock-salt structure using the GGA-mbj functional.

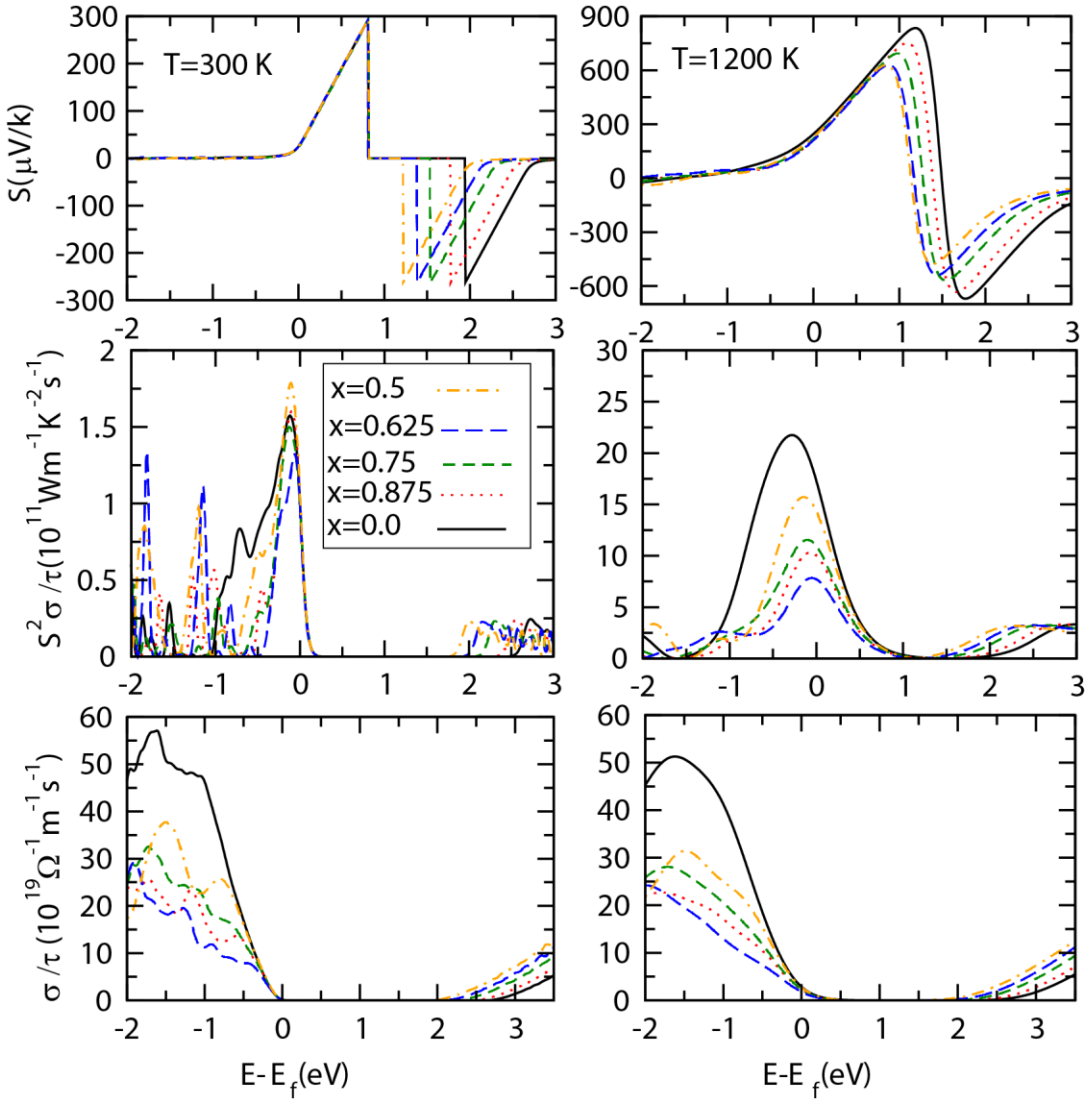

Figure 14. The Seebeck coefficient (S), power factor ($S^2\sigma/\tau$) and electrical conductivity (σ/τ) as a function of the chemical potential at 300 K and 1200 K of $Cd_{1-x}Zn_xO$ (x=0.5, 0.625, 0.75, 0.875, and 1.0) alloys in the wurtzite structure using the GGA-mbj functional.

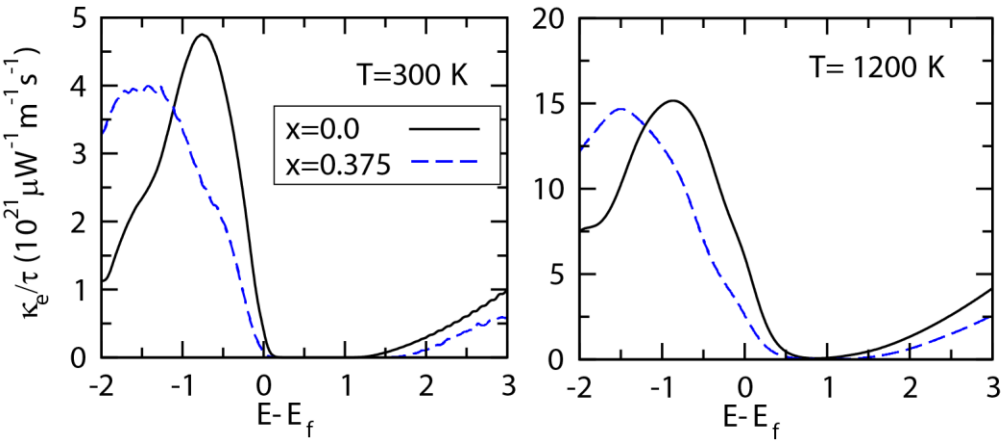

Figure 15. The electronic thermal conductivity (κ_e) as a function of energy at 300 K, and 1200 K of $Cd_{1-x}Zn_xO$ (x=0.0, 0.375) in its rock-salt configuration.

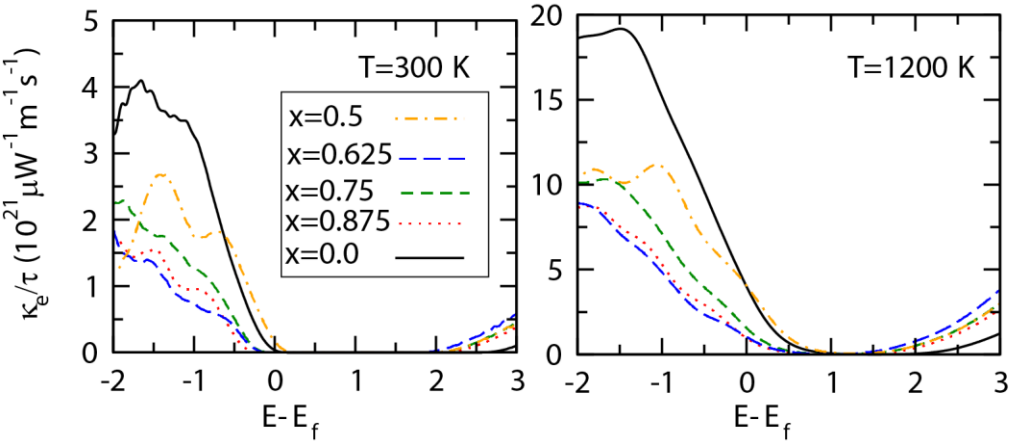

Figure 16. The electronic thermal conductivity (κ_e) as a function of the chemical potential at temperatures 300 K and 1200 K of ZnO and $Cd_{1-x}Zn_xO$ (x=0.5, 0.625, 0.75, 0.875, 1.0) in its wurtzite configuration.

4. Summary

The structural, dynamical, electronic, and thermoelectric properties of $Cd_{1-x}Zn_xO$ alloys were investigated using density functional theory in the rock-salt and wurtzite structures. The alloys were found to be semiconductors using the GGA-mbj functional for all concentrations. The band gap values were found to increase as a function of Zn concentration for both rock-slat and wurtzite structures. The thermoelectric properties were calculated using the Boltzmann transport formalism within the constant relaxation time approximation. The Seebeck coefficient

results show that CdO and ZnO have *n*-type and *p*-type behaviors, respectively, while all ternary alloys exhibit a *p*-type behavior. However, the power factor values increase as the temperature increases. The highest power factor values are obtained for the case of CdO ($36.33\times10^{11}Wm^{-1}k^{-2}s^{-1}$) binary alloy in the rock-salt structure, while the ZnO ($21.75\times10^{11}Wm^{-1}k^{-2}s^{-1}$) binary exhibits the highest power factor values in the wurtzite structure. The power factor values of alloys are found to be higher in the wurtzite structure, which are in the range 7.84×10^{11}-$15.71\times10^{11}Wm^{-1}k^{-2}s^{-1}$ at 1200 K. Therefore, the thermoelectric properties of $Cd_{1-x}Zn_xO$ alloys indicate higher efficiency at higher temperatures, which is promising for high temperature applications.

Chapter 5: investigations of the electronic, magnetic, and thermoelectric properties of VTiRhZ (Z= Al, Ga, In) Quaternary Heusler Alloys

5.1 Introduction

Recently, Heusler alloys have received a considerable attention as promising candidates in spintronics and thermoelectric applications. There are four categories of Heusler alloys that include full Heusler alloys (FHA), Half-Heusler alloys (HHA), Quaternary-Heusler alloys (QHAs) and Inverse Heusler alloys. The FHAs have the chemical formula (X_2YZ) with four interpenetrating cubic lattices, where X and Y are transitional metals (Y could be a rare-earth atom) and Z is an *s-p* element (main group element). Here, X atoms occupy the 8c (1/4, 1/4, 1/4) Wyckoff position with T_d symmetry, whereas the Y and Z atoms occupy 4a (0, 0, 0) and 4b (1/2, 1/2, 1/2) Wyckoff positions, respectively, with the O_h symmetry [15] . When the valence numbers of Y are less than X, the resulting alloy has a space group of $Fm\overline{3}m(no.225)$ and it crystallizes in the L_{21} structure [15]. Nonetheless, they have the so-called XA crystal structure when the valence number of X element is less than that of Y, which are known as the inverse Heusler alloys with the space group $F\overline{4}3m$ [16], [83]. Here, the X element occupy 4a (0, 0, 0) and 4c (1/4, 1/4, 1/4) Wyckoff positions, whereas the Y and Z elements occupy 4a (0, 0, 0) and 4b (1/2, 1/2, 1/2) Wyckoff positions, respectively. The HHAs, however, have the chemical composition (XYZ) forming three interpenetrating cubic lattices and one vacant lattice. They have a space group of $F\overline{4}3m$ with the $C1_b$ crystal structure [17]. On the other hand, QHAs have the XX′YZ chemical formula with Y-type or LiMgPdSb-type crystal structure and a space group of $F\overline{4}3m$ (#216) [18].

Heusler alloys could be metals, semiconductors, spin gapless semiconductors, or half-metallic materials. Most of these alloys demonstrate half-metallic electronic properties. These half-metallic materials (HMMs) have a unique electronic structure where one spin channel show

a metallic behavior, whereas the other spin channel is semiconducting. This behavior of HMMs leads to an excellent spin-polarization (100%) near the Fermi energy, which maximizes the efficiency of magneto-electronic devices, such as giant magnetoresistance and tunneling magnetoresistance [84]. In 1983, the half-metallic behavior of Heusler alloys such as NiMnSb was predicted by Groot *et al.* [85]. From then on, a lot of HMMs based on Heusler alloys have been investigated using first-principal calculations, where several of them have become candidate materials for applications of spintronic and thermoelectric devices [18], [86], [87]. Recently, QHAs have received a good deal of interest due to their novel electronic, magnetic, and thermoelectric properties [88], [89], [90], [91]. In addition, the electronic devices depending on the QHAs are anticipated to have lower-power dissipation [92]. Although some QHAs such as NiFeMnGa, NiCoMnGa and ZrFeVZ (Z = Al, Ga, In) compounds [93] have shown excellent half-metallic behaviors, others such as CuCoMnGa exhibited a metallic behavior [94]. Using the plane-wave pseudopotential method, Li *et al.* predicted the half-metallicity of NbX′CrAl (X′=Co, Rh) quaternary Heusler alloys [95]. They also found that NbRhCrAl alloy became more robust against the lattice thermal expansion as the temperature increase [95]. Haleoot and Hamad have performed theoretical investigation of CoFeCuZ (Z = Al, As, Ga, In, Pb, Sb, Si, Sn) QHAs [17]. They found that CoFeCuPb alloy exhibits a half-metallic ferromagnetic structure with a spin-minority band gap of 0.303 eV and a total magnetic moment of 4.00 μ_B [17]. However, the other alloys were found to be either metallic for Z = (Al, As) or nearly half-metallic for Z = (Ga, In, Sb, Si, Sn) [17]. Bainsla *et al.* have reported that the CoFeMnGe QHA has a cubic structure of Y-type, and there is no phase transition at higher temperatures up to the melting temperature (1400 K) [96]. In addition, several investigations predicted very interesting thermoelectric properties such as tunable lattice thermal conductivity, large Seebeck coefficient, and high

thermoelectric functioning for QHAs [89], [97], [98], [99], [100]. The thermoelectric efficiency of these QHAs can be inferred by the dimensionless figure of merit ($ZT = \frac{S^2\sigma T}{\kappa_e+\kappa_L}$), where *S* is the Seebeck coefficient, σ is the electrical conductivity, *T* is absolute temperature and κ_e and κ_L refer to the electronic and lattice thermal conductivities, respectively [101], [102]. The optimal thermoelectric material (TE) should have large values of *S*, and σ, that lead to the large power factor PF= $S^2\sigma$, and small values of κ_e and κ_L. Recently, Mushtag *et al.* [103] have performed a theoretical study of two new semiconducting QHAs CoCuZrGe and CoCuZrSn by using FP-LAPW technique. They predicted Seebeck coefficient values of 26.2 μV/K and 28 μV/K for CoCuZrGe and CoCuZrSn alloys, respectively with a *p*-type semiconducting behavior. Furthermore, the PF of CoCuZrGe and CoCuZrSn were found to be 1.55×10^{12} $WK^{-2}m^{-1}s^{-1}$ and 1.38×10^{12} $WK^{-2}m^{-1}s^{-1}$, respectively [103]. Moreover, Berri has performed theoretical investigation of CoCrScZ (Z=Al, Si, Ge, and Ga) Quaternary Heusler Alloys. He found that the CoCrScSi, CoCrScGe, CoCrScAl, and CoCrScGa QHAs exhibit a high *ZT* values of 0.15, 0.12, 0.77, and 0.83, respectively [104].The investigations of these QHAs also contribute to expanding the database of HMMs with optimal spin polarization (100%) and good thermoelectric properties.

In this work, the VTiRhZ (Z = Al, Ga, In) QHAs are investigated using first-principal calculations. The investigations include the structural, dynamical, mechanical, electronic, magnetic, and thermoelectric properties of VTiRhZ QHAs. The paper is arranged as follows: section 2 presents the computational details, section 3 includes the results and discussion, and section 4 summarizes the main conclusions.

5.2 Computational methodology

The calculations are based on density functional theory (DFT). The structural optimizations were performed using the projector augmented wave (PAW) method as implemented in Vienna ab initio simulation package (VASP) [41]. In these calculations, the plane-waves were expanded up to a cut-off energy of 520 eV with a total energy tolerance of 10^{-8} eV. For the formation energy calculations, the Brillouin zone integration was established with 22 × 22 × 22 k-point mesh for unit-cell structures. The phonon calculation are obtained using phonopy package as implemented in VASP code [105] with 4 × 4 × 4 supercell structures. These optimized parameters are then used to perform total energy calculations based on full-potential linearized augmented plane wave (FP-LAPW) method as implemented in WIEN2k code [71]. The exchange-correlation potential is treated by using Perdew–Burke–Ernzerhof Generalized Gradient Approximation (GGA-PBE) [43]. The wavefunctions in the interstitial region were described by plane waves with a cut-off value $K_{max} \times R_{MT}$=8.5, where R_{MT} is the smallest atomic muffin tin radius and K_{max} is the largest k vectors in plane wave expansion. The R_{MT} are chosen to be 2.4, 2.2, 2.0, and 1.9 atomic units (a.u.) for V, Ti, Rh, and Z atoms, respectively. The maximum angular momentum (l_{max}) inside the muffin-tin spheres was set to be 10 and the Fourier expansion of the charge density (G_{max}) was truncated at 12 $(Ryd)^{-1}$. In the self-consistent calculations, the total energy and charge density convergence tolerances were set to 10^{-4} Ry and 10^{-4} eV, respectively and the force tolerance was set up equal to 1 mRy/a. u. The thermoelectric parameters including the Seebeck coefficient, electrical conductivities, electronic thermal conductivity and power factor were calculated using Boltzmann transport theory, as implemented in the BoltzTrap code [106]. These TE properties are based on DFT calculations

with a high dense mesh of 5.0×10^4 k-points, which is equivalent to a $36 \times 36 \times 36$ k-mesh. The TE calculations were performed within the constant relaxation time approximation.

5.3 Results and Discussions

This section presents the structural, dynamical, mechanical, electronic, magnetic, and thermoelectric properties of VTiRhZ (Z = Al, Ga, In) alloys.

5.3.1 Structural properties

The chemical formula of VTiRhZ (Z = Al, Ga, In) QHAs is XX′YZ with 1:1:1:1 stoichiometry, where X, X′, and Y are transition metals and Z is an *s*-*p* element. The QHAs possess a face-centered cubic LiMgPdSn (Y-type) crystal structure with a space group $F\bar{4}3m$ (*no.* 216). In this type, the QHAs have three possible atomic configurations identified as LiMgPdSn (Y-type) crystal structures, see Table 3 and Figure. 17. The ground state configuration of each QHAs is identified by the standard energy minimization techniques, where the type-1 structure was found to be the most preferred structure, see Table 4. These results are in agreement with those of similar alloys such as CoFeMnZ (Z=Al, Ga, Si, Ge) [92].

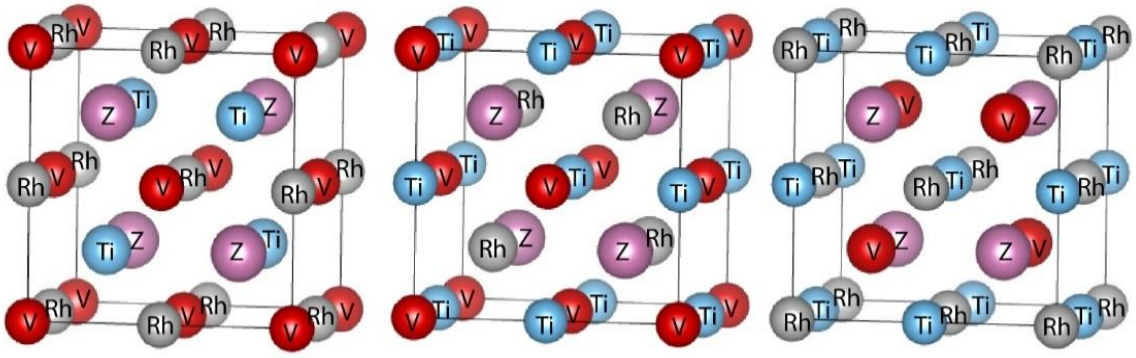

Figure 17. The conventional cells of VTiRhZ (Z=Al, Ga, In) quaternary Heusler alloys in the three types of configurations.

Table 3. The Wyckoff positions 4a (0,0,0), 4c (1/4,1/4,1/4), 4b (1/2,1/2,1/2), 4d (3/4,3/4,3/4) of the atoms in VTiRhZ, (Z= Al, Ga, In) quaternary Heusler alloys for three types of configurations.

Y-type	4a	4c	4b	4d
I	V	Ti	Rh	Z
II	V	Rh	Ti	Z
III	Rh	V	Ti	Z

Table 4. The total energy in eV of VTiRhZ (Z=Al, Ga, In) in the three types of configurations.

Alloys	Type-I	Type-II	Type-III
VTiRhAl	-30.102	-28.673	-29.316
VTiRhGa	-29.059	-27.945	-28.360
VTiRhIn	-27.820	-26.736	-26.996

The thermodynamic stability of these alloys is examined by the formation energy using the following equation [17]:

$$E_{form} = E_{tot} - \left(E_X^{bulk} + E_{X'}^{bulk} + E_Y^{bulk} + E_Z^{bulk}\right) \qquad \text{Equation52}$$

Here E_{tot} refers the total energy of the QHAs per formula unit, whereas E_X^{bulk}, $E_{X'}^{bulk}$, E_Y^{bulk} and E_Z^{bulk} refer to the total energies per atom in the alloys. The formation energy values of these alloys are presented in Table 5. All energies are found to be negative, which indicates the thermodynamic stability of VTiRhZ (Z= Al, Ga, In) QHAs in their type-I configuration. The optimized lattice parameter for each alloy is presented in Table 5.

5.3.2 Dynamical properties

This subsection presents the phonon calculations and dispersions relations to provide a better understanding of the dynamic stability of the investigated systems. The phonon dispersion curves (PDCs) of these alloys are obtained using phonopy package as implemented in VASP code [105]. The PDCs are depicted along the high symmetry k-path (W→L→Γ→X→W) in the first Brillouin zone, see Figure. 18(a, b, c). These curves show only positive frequencies without any imaginary (negative) frequencies for the three alloys, which confirms their dynamic stability

in the type-I configuration. The unit cell contains four atoms (N=4), which leads to twelve phonon branches (3N), three acoustic and nine optical branches at the lower and higher frequencies, respectively, see Figure 18. The three acoustic branches are composed of one longitudinal (LA) and two transverse (TA) modes. This figure shows that VTiRhAl, VTiRhGa, VTiRhIn alloys exhibit no phonon band gaps between acoustic and optical branches. This property is advantageous for the high power factor and low thermal conductivity [107].

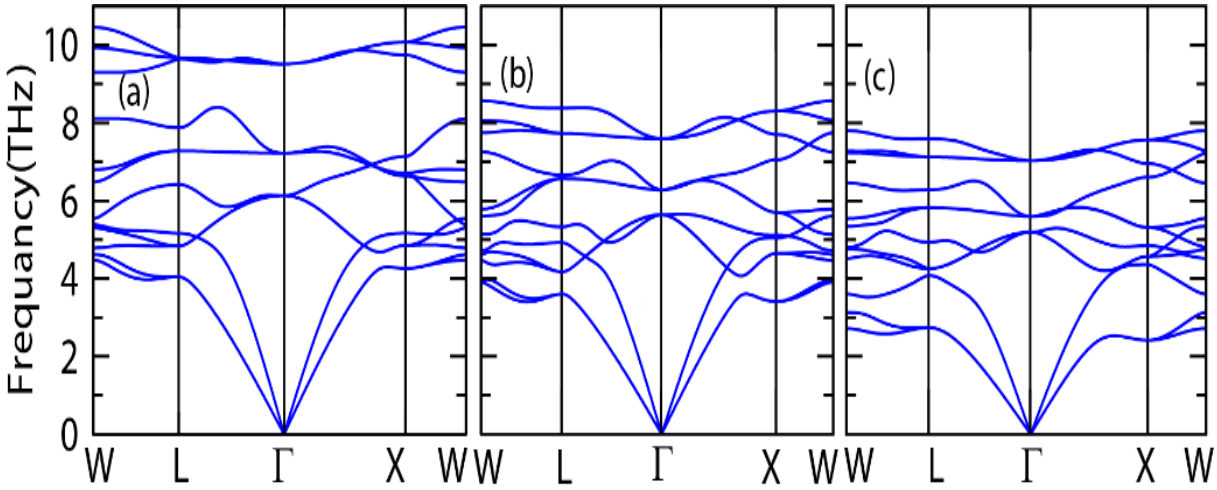

Figure 18. The phonon dispersion curves of (a) VTiRhAl, (b) VTiRhGa, (c) VTiRhIn quaternary Heusler alloys.

5.3.3 Mechanical properties

In this subsection, the elastic constants C_{ij} are calculated to provide a critical information about mechanical properties of the VTiRhZ QHAs. The cubic structure possesses three independent elastic constants, namely, C_{11}, C_{12}, *and* C_{44}, which refer to the longitudinal compression, transverse expansion, and share modulus predictor, respectively. There are three conditions of the Born and Huang criteria that should be satisfied to indicate the mechanical stability of the cubic structure given as [108]:

$$C_{44} > 0\,, (C_{11} - C_{12})/2 > 0, (C_{11} + 2C_{12})/3 > 0 \qquad \text{Equation53}$$

According to these criteria, VTiRhZ alloys are mechanically stable in the type-I structure, see Table 5. Moreover, other mechanical parameters such as the bulk modulus (*B*), Voigt-Reuss shear modulus (*G*), Young's modulus (*E*), anisotropy factor (*A*), Poisson's ratios (ν), Pugh's ratio (*B/G*) and Cauchy pressure (C_P) can be investigated by using the independent elastic constants [109], [110], [111], [112]. The calculated values of these mechanical parameters are presented in Table 5.

The bulk modulus (*B*) measures the resistance of a material to compressions and is defined as follows:

$$B = \frac{(C_{11} + 2C_{12})}{3} \qquad \text{Equation54}$$

The lowest *B* value of 152.1 GPa was predicted for the case of VTiRhIn alloy, due to its higher lattice parameter, than those of VTiRhAl (168.2GPa) and VTiRhGa (171.4 GPa) alloys, see Table 5. These results are close to previous ab initio investigations of Ti_2RhSi (166.19 GPa), and Ti_2RhGe (153.02 GPa) QHAs [113]. The shear modulus (*G*) gives information about the change of the shape due to an applied force, which is defined as the average of Voigt's shear (G_V) and Reuss's shear (G_R) moduli as follows:

$$G = \frac{(G_V + G_R)}{2} \qquad \text{Equation55}$$

where:

$$G_V = \frac{C_{11} - C_{12} + 3C_{44}}{5} \qquad \text{Equation56}$$

$$G_R = \frac{(5C_{44}(C_{11} - C_{12}))}{4C_{44} + 3(C_{11} - C_{12})} \qquad \text{Equation57}$$

The largest *G* value of 93.6 GPa was obtained for VTiRhAl alloy. In addition, Young's modulus (*E*) provides a measure of the stiffness of a material, which is expressed in terms of *G* and *B* as follows:

$$E = \frac{9GB}{3B + G} \qquad \text{Equation58}$$

The highest *E* value was obtained for the case of VTiRhAl alloy, which indicates that it is the stiffest as compared to VTiRhGa and VTiRhIn alloys, see Table 5.

Poisson's ratio (ν) provides a measure of the compressibility of the material, which is expressed as follows:

$$\nu = \frac{3B - 2G}{2(3B + G)} \qquad \text{Equation59}$$

Poisson's ratio usually ranges between 0.25 to 0.5 [114]. Materials with more than 0.26 are considered as the ductile, whereas those with values less than 0.26 [103] are brittle. In this work, the values of Poisson's ratio are 0.27, 0.28, and 0.29 for VTiRhAl, VTiRhGa and VTiRhIn, respectively, which indicate that these QHAs are stable and ductile. The results are comparable to previous calculations of similar structures such as CoCuZrSn (ν = 0.38) and CoCuMnSn (ν = 0.28) [103].

Another important quantity for the measure of stability is Cauchy pressure, which is defined as follows:

$$C_p = C_{12} - C_{44} \qquad \text{Equation60}$$

The material is considered to be ductile if its Cauchy pressure value is positive, otherwise it is brittle [115]. The Cauchy pressure of VTiRhZ (Z=Al, Ga, In) alloys are found to be positive values, which proves that these alloys are ductile in nature. In addition, the *B/G* calculation also

gives information about ductility and brittleness of materials. While ductile materials possess $B/G > 1.75$, brittle materials have $B/G < 1.75$ [116]. The values of *B/G* for VTiRhAl, VTiRhGa and VTiRhIn alloys are 1.76, 1.99 and 2.15, respectively, which further confirms the ductile nature of VTiRhZ alloys.

The elastic anisotropy factor is another important quantity, which is defined as follows:

$$A = \frac{2C_{44}}{C_{11} - C_{12}} \qquad \text{Equation61}$$

Isotropic materials have an anisotropy factor A=1, whereas, anisotropic materials exhibit A values more or less than unity [117]. Accordingly, VTiRhZ alloys are considered to be anisotropic since the anisotropy factor values are less than unity, see Table 5. This is consistent with previous calculations of the anisotropy factor for CoFeCrGe (0.62) and CoFeTiGe(0.76) QHAs[91].

The melting temperature of materials identifies the heat resistance of the material, which can be computed with following equation [115], [118]:

$$T_{melt} = \left[553\text{K} + \left(\frac{5.91\text{K}}{GPa}\right)\text{C}_{11}\right] \pm 300\text{K} \qquad \text{Equation62}$$

From this equation, the melting temperature values of VTiRhAl, VTiRhGa, and VTiRhIn are found to be 2312 K, 2268 K and 2028 K, respectively. These high melting temperatures indicate the stability of these alloys within an error of $\pm 300\text{K}$. The melting temperature was found to decrease by increasing the atomic number of Z atoms.

Table 5. The formation energy E_{form} (eV), optimized lattice constant a (Å), elastic constant C_{ij} (GPa), bulk modulus *B* (GPa), Young's modulus *E* (GPa), isotropic shear modulus *G* (GPa), Poisson's ratios ν, anisotropy factor *A*, Cauchy pressure C_p (GPa), Pugh's ratio *B/G*, and melting temperature T_{melt} (K) for the stable type-I structure of VTiRhZ alloys.

Alloys	E_{form}	a	C_{11}	C_{12}	C_{44}	B	E	G	ν	A	C_p	B/G	T_{melt}
VTiRhAl	-2.37	6.16	297.8	103.5	86.4	168.2	236.1	93.6	0.27	0.89	211.4	1.76	2312
VTiRhGa	-2.16	6.15	290.3	112.0	75.4	171.4	215.3	83.8	0.28	0.84	214.9	1.99	2268
VTiRhIn	-1.28	6.38	249.7	103.4	61.9	152.1	178.7	68.7	0.29	0.84	187.8	2.15	2028

5.3.4 Electronic properties

This subsection introduces the electronic structure of VTiRhZ (Z= Al, Ga, In) quaternary Heusler alloys. Figure 19(a, b, c) presents the band structures and total density of states (TDOS) of VTiRhZ (Z= Al, Ga, In) alloys in their stable configuration (type-I) along the high symmetry k-path. This figure shows that VTiRhAl alloy has a semiconducting behavior in both majority and minority spin channels with band gap values (0.04 and 0.62 eV), respectively. Both VTiRhGa and VTiRhIn possess a half metallic behavior (metallic majority spin channel and a semiconducting minority spin channel). The minority spin band gaps of VTiRhGa and VTiRhIn alloys are found to be indirect from the conduction band maximum (CBM) at the L high symmetry point to the valence band minimum (VBM) at the Γ high symmetry point with 0.52 and 0.19 eV, respectively. It is obvious that the band gap in the minority spin channel decreases by increasing the atomic number of the Z atom (Al, Ga, and In), see Table 6. Moreover, the flat energy levels are presented in the Γ -X symmetry line of the conduction bands. In addition, there is the extremely dispersive bands in other directions. These two properties could be a feature to increase the Seebeck coefficient value and power factor [119]. From Figure. 19 (a), one can that the valence band in the majority channel is exactly located at the Fermi level, which indicates that this alloy is classified as spin-gapless semiconductor materials. However, VTiRhGa and

VTiRhIn alloys show a shift in of the valence bands above the Fermi level at the high symmetry point. This indicates the half- metallic behavior of these two alloys, which are very close to be spin-gapless semiconductor materials. These results are in agreement with previous ab initio investigations of (PtVScAl, PtVYAl, and PtVYGa) QHAs [120]. The projected density of states (PDOS) is presented in Figures. 20 (a, b, c). From these figures, the valence band of these alloys have two main regions. The first region between -4 eV to -2 eV exhibits the main contribution of Rh-*d* orbital and small contributions of *d*- and *p*- orbitals of Ti and Z (Z= Al, Ga, In) atoms in both the majority and minority spin channels. However, the second region is between -2 eV to the Fermi level shows a mixture of different orbitals in majority spin channel, whereas the minority spin channel is mainly contributed by *d*-orbital of V atom. In the conduction band for these alloys, the most significant contribution comes from atoms of V, Ti, and Rh-d orbitals.

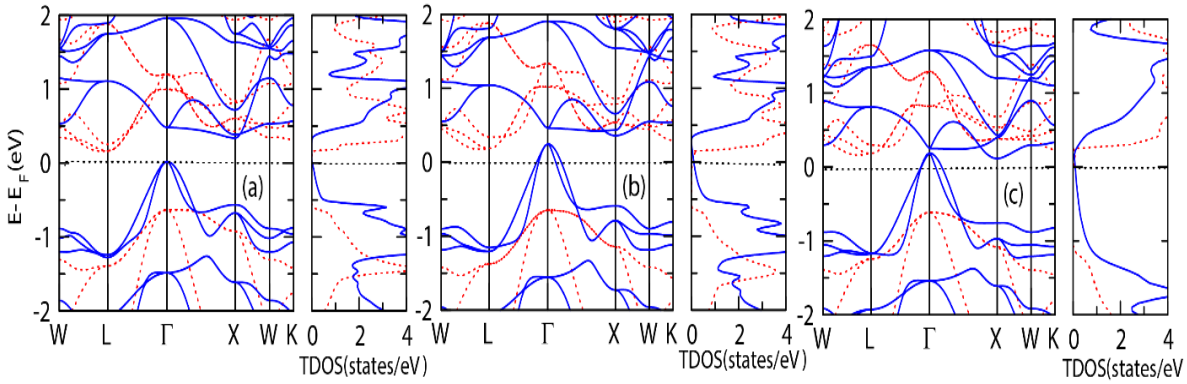

Figure 19. The electronic band structures and total density of states (TDOS) of (a) VTiRhAl, (b) VTiRhGa, (c) VTiRhIn. The solid and dotted lines represent the majority and minority spin channels, respectively.

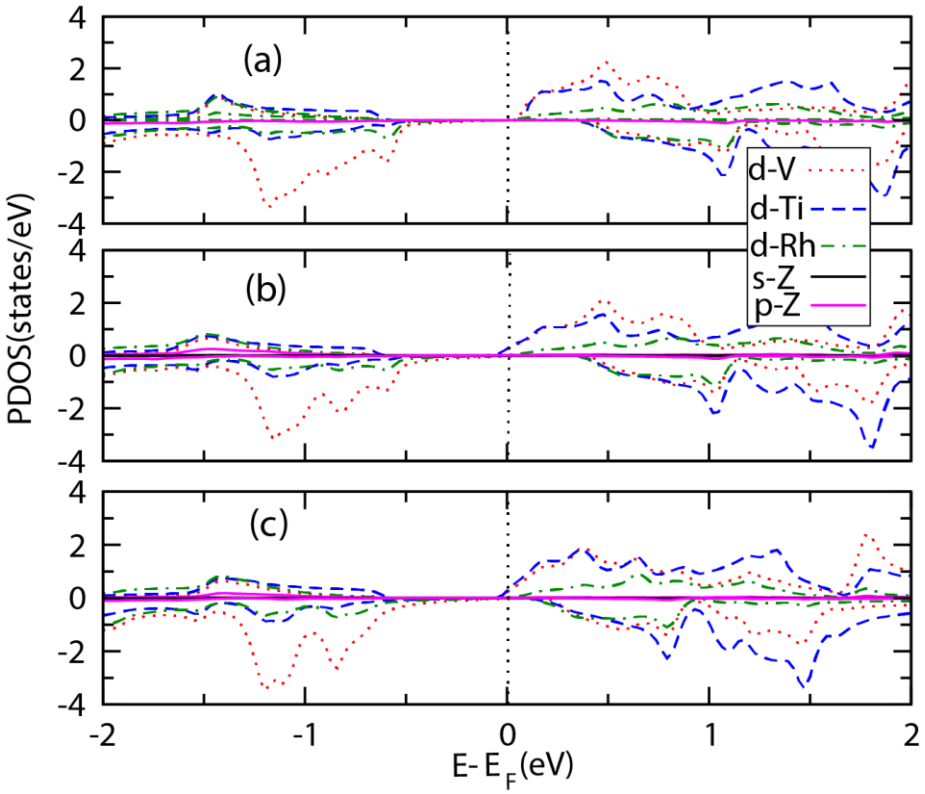

Figure 20. The projected density of state (PDOS) of (a) VTiRhAl, (b) VTiRhGa, (c) VTiRhIn for the majority and minority spin channels.

The spin polarization at the Fermi level is a key quantity that measures the half metallicity of structures, which can be calculated using the following equation [121]:

$$P = \frac{\rho_{\text{majority}}(E_f) - \rho_{\text{minority}}(E_f)}{\rho_{\text{majority}}(E_f) + \rho_{\text{minority}}(E_f)} \times 100 \qquad \text{Equation63}$$

where $\rho_{\text{majority}}(E_f)$ and $\rho_{\text{minority}}(E_f)$ correspond to the majority and minority spin density of states at the Fermi level E_f, respectively [121]. The spin polarization value of 100% is a perfect half-metallicity due to a zero density of states at the Fermi level E_f in either majority or minority spin channels. The spin polarization values of the alloys are listed in Table 6. A perfect spin polarization of 100% was obtained for both VTiRhGa and VTiRhIn alloys, which corresponds to a half-metallic behavior.

5.3.5 Magnetic properties

In this subsection, the magnetic properties are calculated for the dynamically stable VTiRhZ (Z= Al, Ga, In) QHAs. In general, half-metallic materials have integer values of magnetic moments (M) based on the slater-Pauling equation[122], [123]:

$$M_{tot} = N_{\uparrow} - N_{\downarrow} = (Z_{tot} - N_{\downarrow}) - N_{\downarrow} = Z_{tot} - 2N_{\downarrow} \qquad \text{Equation64}$$

where, M_{tot}, $N_{\uparrow}$, $N_{\downarrow}$, and $\mathrm{Z_{tot}}$ are the total magnetic moment, the majority spin valence electrons, the minority spin valence electrons, and the total valence electron number, respectively. For the cases of VTiRhAl, VTiRhGa, and VTiRhIn, the total magnetic moment was found to be $3\mu_B$, which is in agreement with those of similar alloys such as PtZrTiAl and PdZrTiAl [124]. These values can be calculated using the Slater-Pauling rule using the valence electron configurations of V ($3d^3 4s^2$), Ti ($3d^2 4s^2$), Rh ($4d^8 5s^1$) and Z = (Al($3s^2 3p^1$), Ga ($4s^2 4p^1$), and In ($5s^2 5p^1$). Therefore, the total valence electron number for VTiRhAl, VTiRhGa, and VTiRhIn is $Z_{tot} = 21$. Using the TDOS at the Fermi level (E_f), the valence electrons have 12 and 9 in the majority and minority spin channels, respectively. Thus, the total magnetic moment of VTiRhAl QHA is $\mathrm{M_{tot}} = \mathrm{N_{\uparrow}} - \mathrm{N_{\downarrow}} = 12 - 9 = 3\mu_B$, which satisfy the Slater-Pauling rule $\mathrm{M_{tot}} = \mathrm{N_{majority}} - \mathrm{N_{\downarrow}} = (\mathrm{Z_{tot}} - \mathrm{N_{\downarrow}}) - \mathrm{N_{\downarrow}} = \mathrm{Z_{tot}} - 2\mathrm{N_{\downarrow}} = \mathrm{Z_{tot}} - 18$. The local magnetic moments of V, Ti, Rh in the cases of VTiRhAl, VTiRhGa, VTiRhIn alloys are ferromagnetically coupled, where the V atoms show the highest magnetic moments of 2.19, 2.21, and 2.25 μ_B, respectively. The values of the total and local magnetic moments per atom are presented in Table 6.

The linear relation between Curie temperature (T_C) and total magnetic moments is considered to be one of the methods that has been adopted to estimate the Curie temperature by using the following equation [17], [115], [125], [126]:

$$T_C = 23 + 181\, M_{tot} \qquad \text{Equation65}$$

The value of Curie temperature for VTiRhZ alloys is found to be 566 K, which is higher than room temperature. Thus, these QHAs are appropriate for spintronics applications.

Table 6. The calculated band gap values Eg(eV), spin polarization (P%), total magnetic moment Mtotal (μB), and local magnetic moment per atom (V, Ti, Rh, Z) for VTiRhZ (Z= Al, Ga, In) alloys.

Alloys	E_g (eV)		*P*	M_{total} (μ_B)	M_V(μ_B)	M_{Ti}(μ_B)	M_{Rh}(μ_B)	M_Z(μ_B)	Interstitial(μ_B)
	Spin ↑	Spin ↓							
VTiRhAl	0.04	0.62	0	3.00	2.192	0.255	0.126	0.002	0.425
VTiRhGa	-----	0.52	100	3.00	2.213	0.287	0.121	-0.019	0.398
VTiRhIn	-----	0.19	100	3.00	2.251	0.253	0.092	-0.010	0.414

5.3.6 Thermoelectric properties

This subsection presents the thermoelectric properties of VTiRhZ quaternary Heusler alloys. The Boltzmann transport theory is applied to calculate the transport properties of the Seebeck coefficient (*S*), electrical conductivity (σ/τ), and power factor per relaxation time ($S^2\sigma/\tau$). The solution of the Boltzmann transport equation has the following form [81]:

$$\frac{\partial f_{\vec{k}}}{\partial t} = -\overrightarrow{v_{\vec{k}}} \cdot \frac{\partial f_{\vec{k}}}{\partial \vec{r}} - \frac{e}{\hbar}\left(\vec{E} + \frac{1}{c}\overrightarrow{v_{\vec{k}}} \times \vec{H}\right) \cdot \frac{\partial f_{\vec{k}}}{\partial \vec{k}} + \frac{\partial f_{\vec{k}}}{\partial t}|_{scatt} \qquad \text{Equation66}$$

where $\vec{k}$ and $\overrightarrow{v_{\vec{k}}}$ are the wave vector and the group velocity, respectively. $f_{\vec{k}}$ refers to the occupation of the quantum state (the distribution function). Based on this solution, $f_{\vec{k}}$ is based on the applied electric ($\vec{E}$) and magnetic ($\vec{H}$) fields. The Seebeck coefficient and electrical conductivity are given as[101][20]:

$$S_{\alpha\beta}(T,\mu) = \frac{1}{eT\Omega\sigma_{\alpha\beta}(T,\mu)} \int \bar{\sigma}_{\alpha\beta}(\varepsilon)(\varepsilon-\mu)\left[-\frac{\partial f_0(T,\varepsilon,\mu)}{\partial \varepsilon}\right] d\varepsilon \qquad \text{Equation67}$$

$$\sigma_{\alpha\beta}(T,\mu) = \frac{1}{\Omega} \int \bar{\sigma}_{\alpha\beta}(\varepsilon)\left[-\frac{\partial f_0(T,\varepsilon,\mu)}{\partial \varepsilon}\right] d\varepsilon \qquad \text{Equation68}$$

where α and β are tensor indices and μ, Ω, and f_0 are the chemical potential, unit cell volume and the Fermi-Dirac distribution function, respectively.

The thermoelectric properties of VTiRhZ alloys are investigated for the minority spin channel only. This is attributed to the fact that this channel exhibits a semiconducting behavior with a narrow band gap in addition to flat energy states along the Γ -X symmetry line in the conduction band. Narrow band gap semiconductors are believed to exhibit promising thermoelectric properties [127], [128], [129]. The Seebeck coefficient is plotted as a function of the chemical potential at 300 K and 800 K, see Figures. 21 (a) and (b). The Seebeck coefficient gives maximum values near the Fermi level, which decrease as the temperatures increases. At each temperature, the highest and lowest values of the Seebeck coefficient are obtained for VTiRhAl and VTiRhIn alloys, respectively. In The electrical conductivity per relaxation time (σ/τ) is plotted as a function of the chemical potential in Figures. 21 (c) and 5 (d) at 300K and 800K, respectively, which vanishes around the Fermi-level as a typical behavior of semiconductors. In addition, the *n*-type doping reveals higher values of σ/τ than the *p*-type for the investigated QHAs. The values of the power factor as a function of the chemical potential at 300 K and 800 K are also presented in Figure. 21 (e) and (f). Unlike the Seebeck coefficient, the *PF* values are found to be higher at 800K than 300K. From this figure, one can notice that the highest and lowest *PF* values at 800 K are 8.2×10^{11} W.m^{-1} K^{-2} s^{-1} and 14×10^{11} W.m^{-1} K^{-2} s^{-1} for VTiRhAl and VTiRhIn QHAs, respectively. These predicted values are higher than that obtained in a previous study for CoNbMnAl quaternary Heusler alloy of 6.9×10^{11} Wm^{-1} K^{-2} s^{-1} [123].

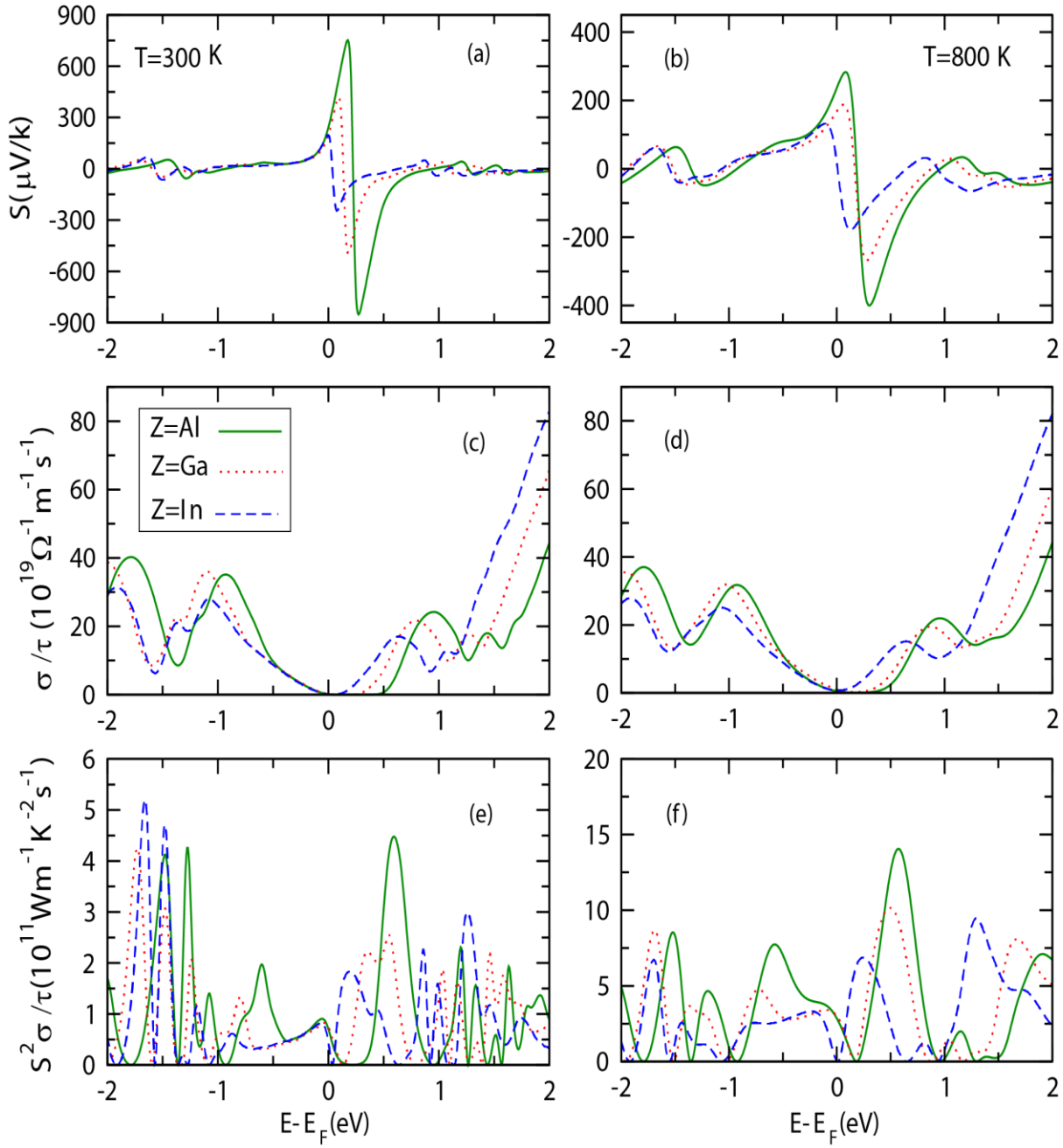

Figure 21. (a) and (b) the Seebeck coefficient (S), (c) and (d) electrical conductivity per relaxation time (σ/τ), and (e) and (f) power factor PF per relaxation time ($S^2\sigma/\tau$) as a function of the chemical potential at temperatures of 300K, and 800K for VTiRhZ (Z= Al, Ga, In).

The Seebeck coefficient is depicted as a function of the carrier concentration (*n*) for VTiRhZ QHAs at 300 K and 800 K see Figures. 22 (a and b). The *n* is selected between (10^{17} to 10^{20} cm^{-3}) for both electronic carrier concentration (*n*-type) and the hole carrier concentration (*p*-

type). From figures 22 (a and b), one can notice that the *S* values for VTiRhZ QHAs decrease as a function of *n*. In addition, the values of *S* increase as the temperature increases, in agreement with a previous study of ZrNiPb half-Heusler alloy [130]. The electrical conductivity per relaxation time (σ/τ) as function of the carrier concentration (*n*) for VTiRhZ QHAs at 300 K and 800 K is shown in Figures. 22 (c and d). The σ/τ values are found to increase by increasing *n*, whereas they decrease by increasing the temperature. These results are in agreement with previous ab initio investigations of KScX(X=Sn and Pb) and KYX(Si and Ge) half-Heusler alloys[131].

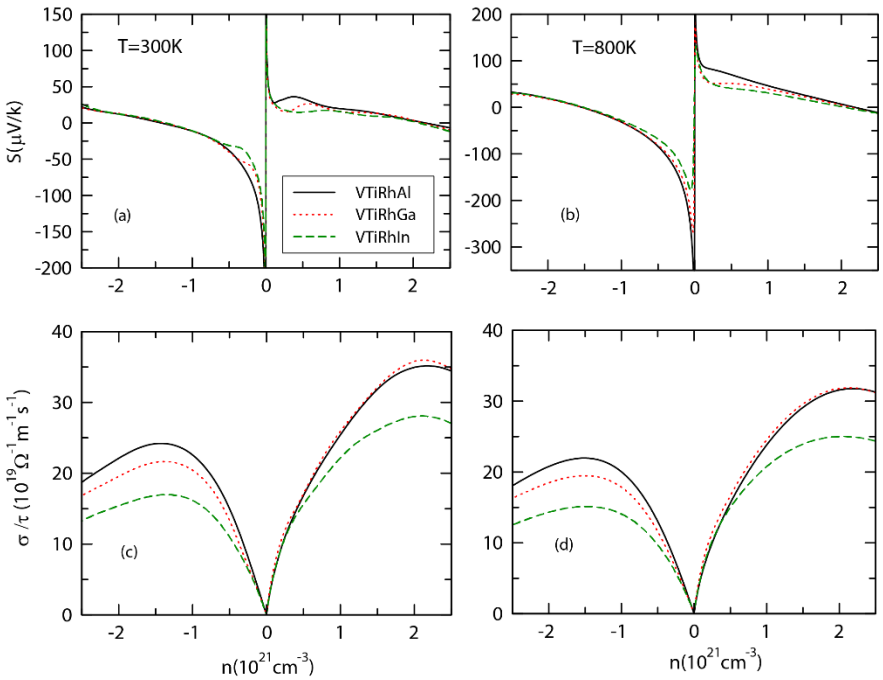

Figure 22. (a) and (b) the Seebeck coefficient (S), and (c) and (d) electrical conductivity per relaxation time (σ/τ) as a function of the carrier concentration (n) at temperatures of 300K, and 800K for VTiRhZ (Z=Al, Ga, In). The positive and negative values of n represent the holes and electron concentrations.

The lattice thermal conductivity (κ_l) is an essential quantity to obtain the figure of merit (ZT) for these investigated QHAs. Slack's formula is considered to be one of the methods that has been successfully used for similar materials[132], [133], [134], [135], [136]to calculate the κ_l value using the following equation [137]:

$$\kappa_l = A\frac{\bar{M}\Theta_D^3 V^{1/3}}{\gamma^2 n^{2/3} T} \quad \text{Equation69}$$

Here A is constant that is given by $(\frac{2.43\times10^{-6}}{1-\frac{0.514}{\gamma}+\frac{0.228}{\gamma^2}})$ [137], and $\bar{M}$, Θ_D, V, γ, n and T refer to the average atomic mass, Debye temperature, volume per atom, Grüneisen parameter, number of atoms in the primitive unit cell, and temperature, respectively. Based on the elastic constant calculations, the Debye temperature and Grüneisen parameter are calculated by using the following equations [137]:

$$\Theta_D = \frac{h}{k_B}\left(\frac{3n}{4\pi\Omega}\right)^{1/3} v_m, \quad \text{Equation70}$$

$$v_m = \left[\frac{1}{3}\left(\frac{2}{v_t^3}+\frac{1}{v_l^3}\right)\right]^{-1/3} \quad \text{Equation71}$$

$$v_l = \sqrt{\frac{3B+4G}{3\rho}} \quad \text{Equation72}$$

$$v_t = \sqrt{\frac{G}{\rho}} \quad \text{Equation73}$$

$$\gamma = \frac{9-12(v_t/v_l)^2}{2+4(v_t/v_l)^2} \quad \text{Equation74}$$

The parameters h, k_B, Ω, ρ , v_m, v_l and v_t refer to the Planck constant, Boltzmann constant, cell volume, density, average, transverse, and longitudinal sound velocities, respectively. The Debye temperature Θ_D, average, transverse, longitudinal sound velocities, density and Grüneisen parameter γ are listed in Table 7. The Debye temperature of VTiRhAl (514.11K) is found to be higher than those of VTiRhGa (447.5K) and VTiRhIn (382.8K), which indicates that the lattice thermal conductivity is higher for VTiRhAl than those of VTiRhGa and VTiRhIn alloys. From this table, one can notice that the Debye temperature decreases by increasing the atomic number of the Z atom (Al, Ga, In). These results are in agreement with other previous calculations of Co_2MnZ (Z=Al, Ga, In) [118]. The lattice thermal conductivity was calculated using the aforementioned parameters, see Figure. 23. From this figure, it is obvious that VTiRhAl has higher values of lattice thermal conductivity than those of VTiRhGa and VTiRhIn alloys. The electronic thermal conductivity κ_e and figure of merit *ZT* values are plotted as a function of the chemical potential at 300 K and 800 K, see Figure. 24. The electronic thermal conductivities of the investigated QHAs were found to be higher at 800K than 300K. The *n*-type exhibits higher $\kappa_e$values than *p*-type in both temperatures, see Figures. 24 (a) and (b). The *ZT* values of VTiRhZ (Z=Al, Ga, In) are found to be higher at 300K than 800K, which is opposite to the behavior of the lattice thermal and electronic conductivities (Figures.23 and Figures.24 (a) and (b)). There are two peaks of *ZT* values for each system. At 300K, the VTiRhAl and VTiRhGa exhibit *p*-type behavior with *ZT* values of 0.96, and 0.88, respectively, while VTiRhIn shows both *p*- and *n*-type behaviors with *ZT* values of 0.54 and 0.64, respectively, see Figure. 24 (c). However, all structures exhibit both *p*- and *n*-type behaviors at 800K. At this temperature, the two peaks of VTiRhAl show the highest *ZT* value of 0.85 and 0.69 in *p*-type and *n*-type, respectively, see Figure. 24 (d). These results of *ZT* values are higher than other similar previous calculations of

0.65 eV and 0.71 eV for CoFeTiGe and CoFeCrGe QHAs, respectively [91]. Therefore, VTiRhZ (Z=Al, Ga, In) QHAs are good candidates for further theoretical and experimental investigations in low dimensional and doped systems that may provide higher *ZT* values for promising TE applications.

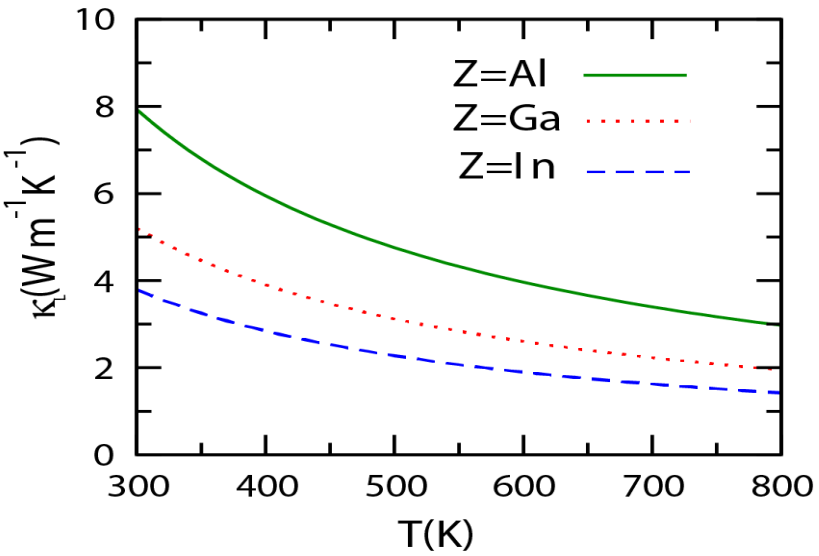

Figure 23. The lattice thermal conductivity (κl) as a function of the temperature for VTiRhZ (Z=Al, Ga, In) alloys.

Table 7. The Debye temperature Θ_D (K), average sound velocities $\boldsymbol{v_m}$ (m/s), transverse sound velocities $\boldsymbol{v_t}$ (m/s), longitudinal sound velocities $\boldsymbol{v_l}$ (m/s), density ρ (kg/m3), and Grüneisen parameter γ.

Alloys	Θ_D	v_m	v_t	v_l	ρ	γ
VTiRhAl	514.1	4226	3802	6687	6475	1.63
VTiRhGa	447.5	3674	3296	6010	7714	1.77
VTiRhIn	382.8	3257	2916	5449	8087	1.82

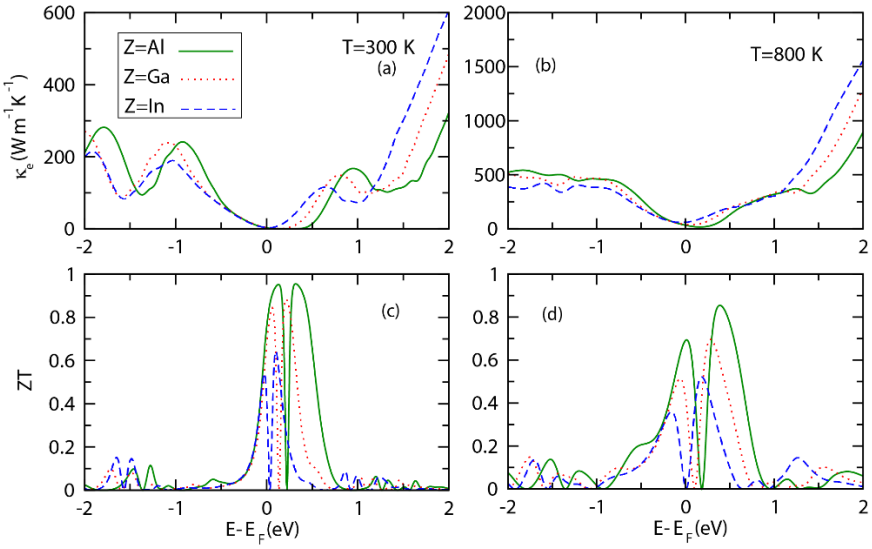

Figure 24. (a) and (b) The electronic thermal conductivity (κ_e) and (c) and (d) figure of merit (ZT) as a function of the chemical potential at 300K and 800K for VTiRhZ (Z=Al, Ga, In) alloys.

5.4 Summary

The structural, dynamical, mechanical, electronic, magnetic, and thermoelectric properties of VTiRhZ (Z = Al, Ga, In) alloys are investigated using DFT calculations. These alloys are found to be stable in the type-I structure. The GGA-PBE calculations predict a half metallic ferromagnetic behavior for VTiRhZ (Z =Ga, In) alloys with band gaps of 0.52, and 0.19, respectively. However, VTiRhAl shows a ferromagnetic behavior with a semiconducting structure in both spin channels. The VTiRhZ (Z= Ga, In) alloys possess a total magnetic moment of $3\mu_B$ and a spin polarization of 100%, which suggest them as prominent candidates for spin-injection. Using the semi-classical Boltzmann transport theory within the constant relaxation time approximation, VTiRhZ (Z=Al, Ga, In) alloys show good thermoelectric properties. The highest value of the power factor per relaxation time is 14×10^{11} Wm^{-1} K^{-2} s^{-1} for VTiRhAl. In addition, VTiRhAl, VTiRhGa, and VTiRhIn alloys show high figure of merit values of 0.96, 0.88 and 0.64, respectively at the room temperature. Thus, these alloys can find significant applications as thermoelectric materials at moderate temperatures.

Chapter 6: investigations of the electronic, magnetic, and thermoelectric properties of VTiRhZ (Z= Si, Ge, Sn) Quaternary Heusler Alloys

6.1 Introduction

The thermoelectric (TE) energy is considered to be one of the essential renewable resources, which can provide a solution to many environmental and energy issues. Thermoelectric devices consist of *p*- and *n*-type semiconductors that are connected thermally in parallel and electrically in series. They can be used to convert the thermal power into electrical power or vice versa based on Seebeck and Peltier effects, respectively [138]. The TE energy conversion efficiency η can be given as[139]:

$$\eta = \frac{\Delta T}{T_h}\frac{\sqrt{1+Z\mathrm{T}}-1}{\sqrt{1+Z\mathrm{T}}+\frac{T_c}{T_h}} \qquad \text{Equation75}$$

where ΔT refers to the difference between the hot (T_h) and cold (T_c) side temperatures ($\Delta T = T_h - T_c$) and ZT refers to the figure of merit, which is expressed as [140]:

$$ZT = (\frac{S^2\sigma T}{\kappa_e+\kappa_L}), \qquad \text{Equation76}$$

Here, S, σ, and T refer to the Seebeck coefficient, electrical conductivity and absolute temperature; κ_e and κ_L represent the electronic and lattice thermal conductivities, respectively. A good TE device should have a high Seebeck coefficient and electrical conductivity and low thermal conductivity. However, it is a tedious task to meet all these properties in one material as they are interdependent parameters. The Seebeck coefficient decreases, while the electrical conductivity increases as a function of the carrier concentration based on the following mathematical formulae [50]:

$$S = (\frac{8\pi^{\frac{2}{3}}k_B^2\left(r+\frac{3}{2}\right)}{3^{5/3}\,eh^2})(\frac{m^*}{n^{2/3}})T \qquad \text{Equation78}$$

$$\sigma = ne\mu \qquad \text{Equation79}$$

where, k_B, *r, h,* m^**, n, e, and* μ refer to the Boltzmann constant, scattering parameter, Planck's constant, effective mass, carrier concentration, electron charge, and carriers' mobility, respectively. However, based on Wiedemann-Franz law ($\kappa_e = L\sigma T$), the high electrical conductivity leads to a high electronic thermal conductivity [52], [141]. There are several methods that provide the requisite good parameters, which lead to a high figure of merit (*ZT*) value. Among these methods, the doping material with selected heavy atoms can reduce the lattice thermal conductivity and keep the electronic thermal conductivity low with a high value of the Seebeck coefficient [142].

So far, the TE properties have been extremely studied for various materials, such as PbTe, Bi_2Te_3, and Mg_2Si [9], [10]. In addition, a huge effort of research has been emphasized on Heusler alloys owing to their unique properties such as electronic, magnetic, thermal and thermoelectric properties [88]. Heusler alloys can be divided into four categories. The first two categories are the full and inverse Heusler alloys, which have the same chemical formula of X_2YZ. When the valence number of Y atom is less than that of X, the alloy is recognized as a full Heusler alloy (FHA). Otherwise, the opposite situation leads to the category of inverse Heusler alloys. The other two categories are Half-Heusler alloys (HHAs) and quaternary-Heusler alloys (QHAs) with the chemical formulae XYZ and XX′YZ, respectively. Here the X, X′, and Y are transition metal atoms, while Z is a main group element.

Among these alloys, quaternary-Heusler alloys have recently received a great deal of attention due to their promising thermoelectric and spintronic properties [94], [92]. For example, Haleoot and Hamad predicted a figure of merit (*ZT*) value of 0.71 and 0.65 for CoFeCrGe and

CoFeTiGe, respectively [91]. Moreover, previous calculations of CoRhMnAs and CoRuMnAs alloys reported high Seebeck coefficients of 53.44 μV/K and 44.3 μV/K with *ZT* values of 0.50 and 0.28, respectively [143]. In addition, promising Seebeck coefficient and power factor values of 539.2 μV/K and 7×10^{10} $Wm^{-1}K^{-2}s^{-1}$, respectively were predicted for ZnFeTiSi QHA at 300K [101]. Furthermore, density functional theory predicted a half-metallic ferromagnetic structure of CoFeMnZ (Z=Al, Ga, Si, Ge) QHAs with high Curie temperatures [92]. Half-metallic ferromagnetism with total magnetic moment of $3\mu_B$ and perfect spin-polarization of 100% were also predicted for FeMnScZ (Z=Al, Ga, In) QHAs [21].

The prime aim of this work is to present three new QHAs, namely, VTiRhSi, VTiRhGe, and VTiRhSn. Computational investigations using first-principal calculations were performed to investigate the structural, electronic, magnetic, and thermoelectric properties of these QHAs. In addition, the thermodynamic, dynamical, and mechanical properties are investigated to provide the plausible feasibility of experimental synthesis for the three new QHAs. These QHAs are found to be promising candidates for spintronic and thermoelectric applications. Their interesting magnetic and thermoelectric properties indicate promising applications in spin injection using the spin-polarized thermoelectric current. To the best of our knowledge, there are no available studies on these QHAs.

The rest of the paper is organized as follows: the computational details are given in section 2. The results and discussions are presented in section 3, and finally, section 4 contains the conclusion.

6.2 Computational methodology

The calculations are performed using density functional theory (DFT) as implemented in VASP code [41]. The cut-off energy and total energy tolerance were chosen as 520 eV and 10^{-8}

eV, respectively. The formation energy was calculated using a 22 × 22 × 22 Γ- centered *k*-point mesh for unit-cell structures. The study of dynamical stability was obtained with phonopy package [105] based on VASP code with 4 × 4 × 4 supercell structures and a 4 × 4 × 4 Γ-centered *k*-point mesh. Then, the optimized structural parameters obtained by VASP code [18] were utilized to calculate the total energy within the full-potential linearized augmented plane wave (FP-LAPW) method as implemented in WIEN2k code [71]. The exchange-correlation potential was treated using the generalized gradient approximation of Perdew–Burke–Ernzerhof (GGA-PBE) [43]. The wavefunctions in the interstitial region were defined with a cut-off value of $K_{max} \times R_{MT}$=8.5, where R_{MT} is the smallest atomic muffin tin radius and K_{max} is the largest reciprocal lattice vector of the plane wave expansion. The values of R_{MT} are picked to be 2.4, 2.2, 2.0, and 1.7 atomic units (a.u.) for V, Ti, Rh, and Z (Z=Si, Ge, Sn) atoms, respectively. The total energy, charge density convergence tolerances and force tolerance were chosen to be 10^{-4} Ry, 10^{-4} e and 1 mRy/a. u, respectively. The transport coefficients, including the Seebeck coefficient, electrical conductivities, electronic thermal conductivity, and power factor were calculated using Boltzmann transport theory, as implemented in the BoltzTrap code [46]. These TE properties are based on DFT calculations with a high dense mesh of 50000 k-points, which is equivalent to a 36 × 36 × 36 Γ- centered k-mesh. The TE calculations were performed using the constant relaxation time approximation, which is set to $0.5\times 10^{-15}s$. This value was used in similar calculations of FeRhCrSi and FeRhCrGe QHAs [19].

6.3 Results and discussions

This section presents the structural, thermodynamic, dynamical, mechanical, electronic, magnetic, and thermoelectric properties of quaternary VTiRhZ (Z=Si, Ge, Sn) Heusler alloys.

6.3.1 Structural properties

The stoichiometry of VTiRhZ (Z = Si, Ge, Sn) QHAs is 1:1:1:1 with XX′YZ chemical formula, where X, X′, and Y are transition metal elements and Z is a main group element that contains *s-p* orbitals. The QHAs are identified to crystallize in the LiMgPdSn (Y-type) face-centered cubic structure with a space group $F\bar{4}3m$ (*no.* 216). This type of structure has three atomic configurations, which are namely Y-type-I, Y-type-II, and Y-type-III, see Figure.25. The Wyckoff positions of the element in the three types are 4a (0,0,0), 4c (¼, ¼, ¼), 4b (½, ½, ½) and 4d (¾, ¾, ¾), see Table8. Based on total energy calculations, Y-type-I configuration was found to be the most favored crystal structure, see Table 9.

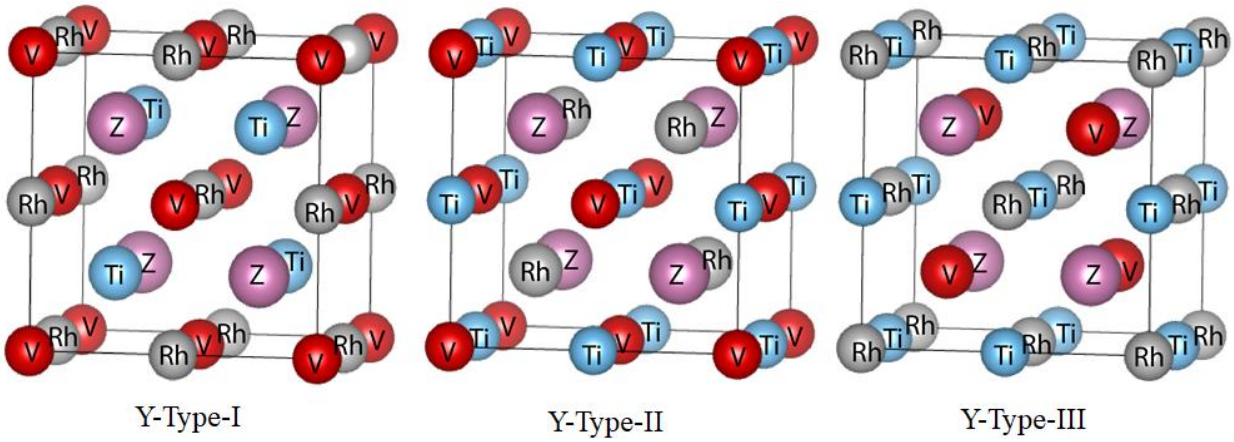

Figure 25. The conventional cells of VTiRhZ (Z=Si, Ge, Sn) quaternary Heusler alloys in the three types of configurations (Y-type-I, Y-type-II, and Y-type-III).

Table 8. The Wyckoff positions 4a, 4c, 4b, 4d of the atoms in VTiRhZ (Z= Si, Ge, Sn) quaternary Heusler alloys for three types of configurations.

Y	4a (0.0.0)	4c (¼, ¼, ¼)	4b (½, ½, ½)	4d (¾, ¾, ¾)
Type-I	V	Ti	Rh	Z
Type-II	V	Rh	Ti	Z
Type-III	Rh	V	Ti	Z

Table 9. The total energy in eV of VTiRhZ (Z= Si, Ge, Sn) QHAs in the three types of configurations.

Alloys	Y-type-I	Y-type-II	Y-type-III
VTiRhSi	-31.698	-30.808	-30.994
VTiRhGe	-30.305	-29.644	-29.672
VTiRhSn	-29.259	-28.241	-28.543

The formation energy (E_{form}) is calculated to identify the thermodynamic stability of these QHAs using the following formula [17]:

$$E_{form} = E_{tot} - \left(E_V^{bulk} + E_{Ti}^{bulk} + E_{Rh}^{bulk} + E_{Z=Si,Ge,Sn}^{bulk}\right), \qquad \text{Equation80}$$

where E_{tot} corresponds to the equilibrium total energy per formula unit of VTiRhSi, VTiRhGe, VTiRhSn alloys and $E_{\mathrm{V}}^{bulk}, E_{\mathrm{Ti}}^{bulk}, E_{\mathrm{Rh}}^{bulk}, E_{Z=\mathrm{Si,Ge,Sn}}^{bulk}$ are the equilibrium total energies per atom in their individual bulk structures. The formation energy values are found to be negative, which indicate that VTiRhZ (Z= Si, Ge, Sn) QHAs are thermodynamically stable, see Table 10. Moreover, Table 10 presents the optimized lattice parameter for each alloy. From this table, it is clear that the lattice parameters are increasing by increasing the atomic number of Z (Z=Si, Ge, Sn) atom. The lattice parameter values are found to be close with experimental result [144] as shown in Table 10.

6.3.2 Dynamical phonon properties

This subsection is devoted to confirming the structural stability of the energetically stable Y-type-I configuration of VTiRhZ alloys obtained in section 3.1. The phonon dispersion curves (PDCs) provide another measure of the dynamical stability of the studied systems. From Figure. 26, it is obvious that these VTiRhZ alloys have positive frequencies (no imaginary modes), thereby emphasizing that VTiRhZ alloys are dynamically stable. As the primitive unit cell consists of four atoms (N=4), there are twelve vibrational modes (3N), where three of them are

acoustic and nine optical modes at the lower and higher frequencies, respectively. One of the three acoustic modes is longitudinal acoustic (LA), while the other two are transverse acoustic (TA). However, the nine optical modes are composed of three longitudinal optical (LO) and six transverse optical (TO) modes. Similar results of PDCs were reported in a previous calculations for CoFeCrGe and CoFeTiGe quaternary-Heusler alloys [91].

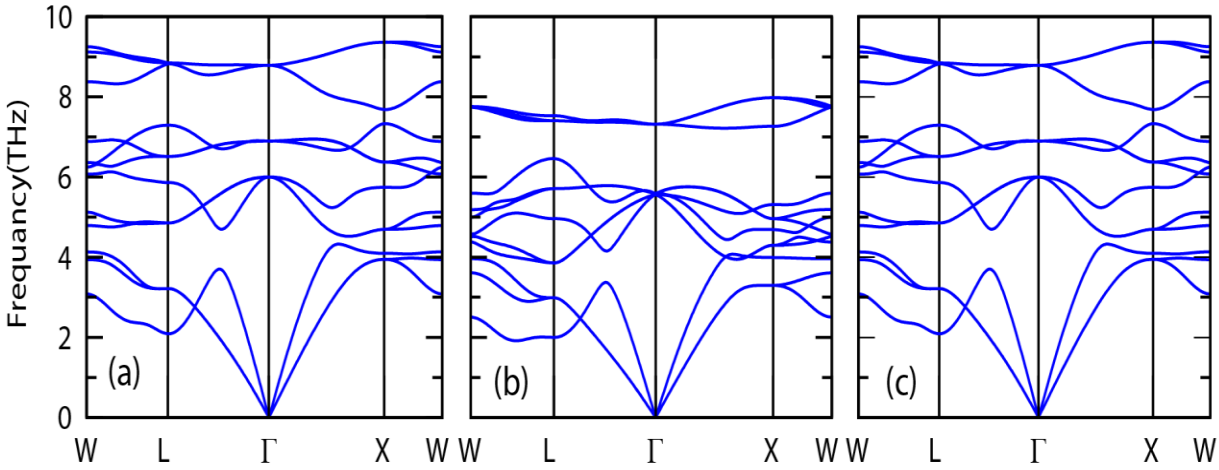

Figure 26. The phonon dispersion curves of (a) VTiRhSi, (b) VTiRhGe, (c) VTiRhSn quaternary Heusler alloys.

6.3.3 Mechanical properties

The mechanical properties are investigated to provide more information about the mechanical stability of the alloys. The structure of VTiRhZ alloys is cubic, which means that these alloys have only three independent elastic constants, namely the longitudinal compression (C_{11}), transverse expansion (C_{12}), and share modulus predictor (C_{44}). In general, any material is mechanically stable if it fulfils the conditions of Born and Huang criteria, which are given as [108]:

$$C_{44} > 0\ , (C_{11} - C_{12})/2 > 0,\ B > 0,\ C_{12} < B < C_{11} \qquad \text{Equation81}$$

From Table 10, one can see that Born and Huang criteria are satisfied for VTiRhZ alloys, which indicates their mechanical stability.

Additionally, from these three independent elastic constants, various mechanical parameters can be calculated such as the bulk modulus (*B*), Voigt(G_V) -Reuss(G_R) shear modulus (*G*), Young's modulus (*E*), Cauchy pressure (C_p), Pugh's ratio (*B/G*), and anisotropy factor (*A*), which can be expressed as follows [109]:

$$B = \frac{(C_{11}+2C_{12})}{3} \quad \text{Equation82}$$

$$G = \frac{(G_V + G_R)}{2} \quad \text{Equation83}$$

$$G_V = \frac{C_{11}- C_{12}+3C_{44}}{5} \quad \text{Equation84}$$

$$G_R = \frac{(5C_{44}(C_{11}- C_{12}))}{4C_{44}+3(C_{11}- C_{12})} \quad \text{Equation85}$$

$$E = \frac{9GB}{3B+G} \quad \text{Equation86}$$

$$C_p = C_{12} - C_{44} \quad \text{Equation87}$$

$$A = \frac{2C_{44}}{C_{11}- C_{12}} \quad \text{Equation88}$$

The calculated mechanical parameters for VTiRhZ alloys are listed in Table 10. The values of Young's modulus, *E*, are 188.5, 165.7, and 160.7 *GPa* for VTiRhSi, VTiRhGe, and VTiRhSn, respectively. The results indicate that VTiRhSi is stiffer than VTiRhGe and VTiRhSn alloys. The bulk and shear moduli are calculated to obtain Pugh's ratio. Both Pugh's ratio (*B/G*) and Cauchy pressure (C_p) are utilized to describe the ductility and brittleness of materials. If *B/G* is more

(less) than 1.75, the materials are ductile (brittle) in nature [116]. In addition, if the C_p value is positive (negative), the material is considered to be ductile (brittle) in nature [115]. The values of *B/G* ratio are 2.7, 2.9 and 2.6 for VTiRhSi, VTiRhGe, and VTiRhSn, respectively. In addition, the Cauchy pressure (C_p) values are 68.5, 67.0 and 50.4 *GPa* for VTiRhSi, VTiRhGe, and VTiRhSn, respectively. The values of *B/G* ratio are found to be higher than 1.75 and C_p values are positive, which indicate the ductile nature of these alloys. These results are consistent with similar QHAs such as CoFeYGe (Y=Ti, Cr) [91]. The value of the anisotropy factor (*A*) is a measure of the anisotropy of the material. Materials with *A*=1 are considered isotropic, while those with *A* values less or more than 1 are anisotropic [117]. Our calculations predict an anisotropy factor less than unity, which indicates that VTiRhZ (Z=Si, Ge, Sn) alloys are anisotropic materials, see Table 10.

Another important quantity is the melting temperature, which gives information about the heat resistance of the material, which can be calculated using the following equation [115], [118], [145]:

$$T_{melt} = \left[553\text{K} + \left(\frac{5.91\text{K}}{GPa}\right)\text{C}_{11}\right] \pm 300\text{K} \qquad \text{Equation89}$$

The melting points of VTiRhSi, VTiRhGe, and VTiRhSn alloys are found to be 2296 K, 2169 K and 2053 K, respectively. The high values of the melting temperature, T_{melt}, indicate the mechanical stability of these QHAs within an error of $\pm 300\text{K}$. The calculations show that a lower longitudinal compression (C_{11}) of the alloys corresponds to a lower melting point value (see Table 10), which are comparable to those of CoFeCrGe (2584K) and CoFeTiGe (2484K) [91].

6.3.4 Electronic and magnetic properties

This subsection presents the band structure, total density of states (TDOS), projected density of states (PDOS) and magnetic properties of VTiRhZ (Z= Si, Ge, Sn) quaternary Heusler alloys. Figure 27 presents the band structure and TDOS of VTiRhZ (Z= Si, Ge, Sn) alloys. The calculations predict a half-metallic behavior for the cases of VTiRhSi, VTiRhGe, and VTiRhSn alloys. In these structures the majority spin channel exhibits a semiconducting behavior with band gap values of 0.42, 0.25, and 0.12eV along the Γ -X symmetry line, respectively, whereas the minority spin channel exhibits a metallic behavior. These results are in a good agreement with previous ab initio investigations of CoFeCuZ (Z=Al, As, Ga, In, Pb, Sb, Si, Sn) quaternary Heusler alloys [5]. Moreover, the presence of flat energy levels in the conduction bands along Γ - X symmetry line and the highly dispersive bands along other directions could be a signature of a high Seebeck coefficient and thermoelectric properties [33].

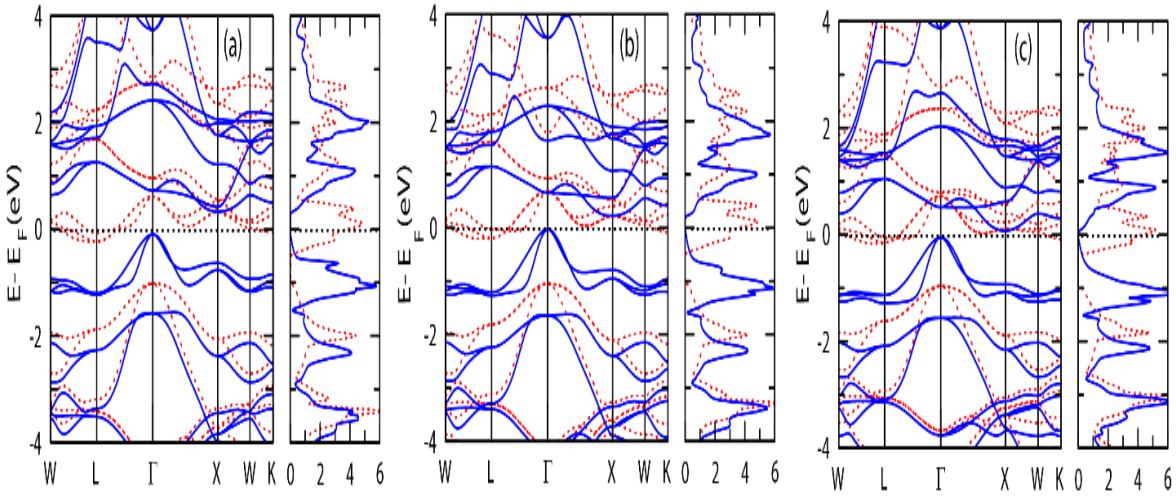

Figure 27. The electronic band structures and total density of states (TDOS) of (a) VTiRhSi, (b) VTiRhGe, (c) VTiRhSn. The solid and dotted lines represent the majority and minority spin channels, respectively.

Table 10. The formation energy E_{form} (eV), optimized lattice constant a (Å), elastic constants C_{ij} (GPa), bulk modulus B (GPa), isotropic shear modulus G (GPa), Young's modulus E (GPa), Pugh's ratio B/G, Cauchy pressure Cp (GPa), anisotropy factor A, and melting temperature T_{melt} (K) for the stable Y-type-I structure of VTiRhZ alloys.

Physical parameter	VTiRhSi		VTiRhGe	VTiRhSn
E_{form}(eV)	-2.28		-1.82	-1.18
a (Å)	6.04 5.8[a]		6.13	6.35
C_{11} *(GPa)*	295.0		273.5	253.9
C_{12} *(GPa)*	131.7		121.0	103.1
C_{44} *(GPa)*	63.2		54.0	52.7
B (GPa)	190.2		176.8	158.4
G (GPa)	70.6		61.7	60.4
E (GPa)	188.5		165.7	160.7
B/G	2.7		2.9	2.6
C_P *(GPa)*	68.5		67.0	50.4
A	0.77		0.70	0.69
T_{melt} *(K)*	2296		2169	2053

[a] Ref. [144] Exp.

Figure 28 presents the projected density of states (PDOS) of VTiRhZ alloys. This figure shows that the lower region of valence bands from -4 eV to -2 eV is formed mostly by Ti, V, and Rh *d* orbitals in both the majority and minority spin channels. However, the main contribution in the upper region of the valence bands from -2 eV to the Fermi level 0 eV comes from V *d* orbital in the majority spin channel, while the main contribution in the minority spin channel comes from the strongly hybridized V, Ti and Rh *d* orbitals. On the other hand, the density of states in the conduction bands of these alloys is a mixture of different orbitals in both the majority and minority spin channels.

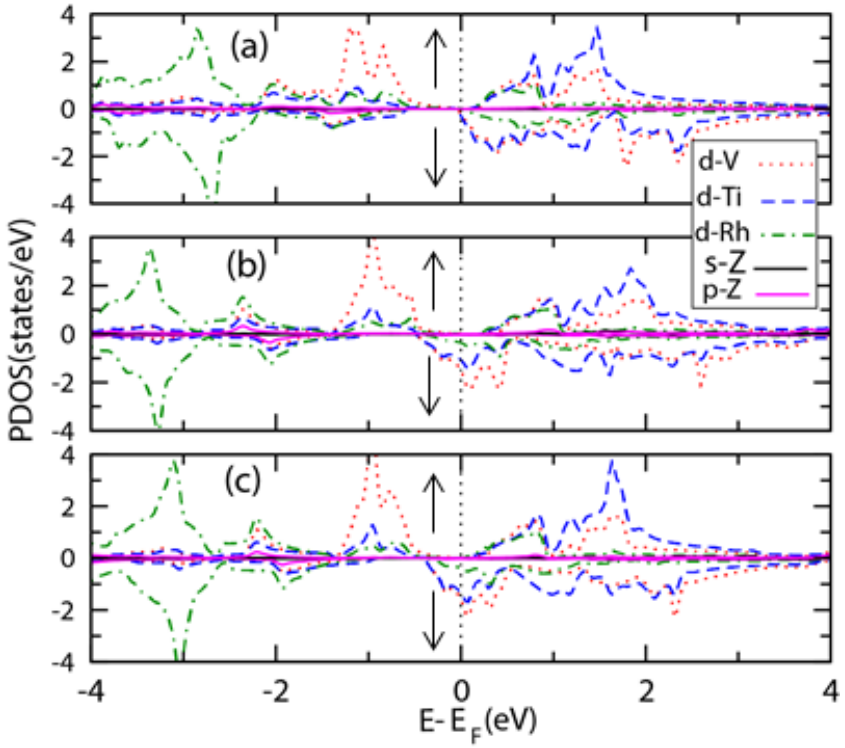

Figure 28. The projected density of state (PDOS) of (a) VTiRhSi, (b) VTiRhGe, (c) VTiRhSn for the majority (↑) and minority (↓) spin channels.

The spin polarization can be measured using the following formula [121]:

$$P = \frac{\rho_{\uparrow}(E_f) - \rho_{\downarrow}(E_f)}{\rho_{\uparrow}(E_f) + \rho_{\downarrow}(E_f)} \times 100 \qquad \text{Equation90}$$

where $\rho_{\uparrow}(E_f)$ and $\rho_{\downarrow}(E_f)$ correspond to the majority and minority spin density of states at the Fermi level E_f, respectively [121]. From Table 11, one can see that VTiRhSi, VTiRhGe and VTiRhSn alloys have a perfect spin-polarization of 100%, which corresponds to a half-metallic behavior. A similar high spin-polarization value is reported for CoFeMnGe QHAs [96].

The total and local magnetic moments for VTiRhZ alloys are presented in Table 11. The integer values of the total magnetic moments of QHAs are found to obey the Slater-Pauling equation for half-metallic materials [122]. [123]:

$$M_{tot} = (Z_{tot} - 20)\,\mu_B \qquad \text{Equation91}$$

where, M_{tot} refers to the total magnetic moment and Z_{tot} is the number of the total valence electrons (Z_{tot} = 22 for the three alloys). This table shows that VTiRhZ (Z=Si, Ge, Sn) alloys exhibit integer values of $2\mu_B$, which confirm the half-metallic behavior of these QHAs. Thus, these QHAs are promising for future spintronic applications [146] . However, the Ti atoms show local magnetic moments of $0.03\mu_B$, -0.03 μ_B, and $-0.11\mu_B$ in the cases of VTiRhSi, VTiRhGe, and VTiRhSn alloys, respectively. The coupling between the local magnetic moments of Ti atoms with those of V and Rh atoms is ferromagnetic in the case of VTiRhSi alloy, while it is antiferromagnetic for VTiRhGe and VTiRhSn alloys. The main contribution of the magnetic moment is attributed to V atoms in VTiRhSi, VTiRhGe, and VTiRhSn with local magnetic moments of 1.57, 1.66, and 1.74 μ_B, respectively.

The linear relation between Curie temperature (T_C) and total magnetic moments is considered to be one of the methods that has been adopted to estimate the Curie temperature by using the following equation [17], [115], [125], [126]:

$$T_C = 23 + 181\ M_{tot} \qquad \text{Equation92}$$

The value of Curie temperature for VTiRhZ alloys is found to be 385 K, which equals that of Co_2TiSi alloy in a previous calculation [147].

Table 11. The calculated band gap values E_g(eV), spin-polarization *P* (%), total magnetic moment M_{total} (μB), local magnetic moments per atom M_i (μB) (i = V, Ti, Rh, Z) for VTiRhZ (Z= Si, Ge, Sn) alloys.

Alloys	E_g (eV)		*P%*	$M_{total}(\mu_B)$	$M_V(\mu_B)$	$M_{Ti}(\mu_B)$	$M_{Rh}(\mu_B)$	$M_Z(\mu_B)$
	Spin↑	Spin↓						
VTiRhSi	0.42	-----	100	2.00	1.57	0.03	0.12	-0.01
VTiRhGe	0.25	-----	100	2.00	1.66	-0.03	0.11	-0.03
VTiRhSn	0.12	-----	100	2.00	1.74	-0.11	0.11	-0.02

6.3.5 Thermoelectric properties

This subsection presents the thermoelectric properties of VTiRhZ quaternary Heusler alloys. These alloys were found to be very interesting for thermoelectric applications as they exhibit narrow band gaps of 0.42, 0.25, and 0.12 eV in the majority spin channel (see section 3.4). A narrow band gap semiconductor is believed to show a good thermoelectric performance[127]. The semiclassical Boltzmann transport theory within the constant relaxation time approximation is utilized to investigate the transport coefficients of VTiRhZ alloys as implemented in BoltzTraP package [148]. The Seebeck coefficient (S), electrical conductivity (σ), and electronic thermal conductivity (κ_e) are calculated using the following equations [101]:

$$S_{\alpha\beta}(T;\mu) = \frac{1}{eT\Omega\sigma_{\alpha\beta}(T;\mu)}\int \bar{\sigma}_{\alpha\beta}(\varepsilon)(\varepsilon - \mu)\left[-\frac{\partial f_0(T;\varepsilon)}{\partial\varepsilon}\right]d\varepsilon \qquad \text{Equation93}$$

$$\sigma_{\alpha\beta}(T,\mu) = \frac{1}{\Omega}\int \bar{\sigma}_{\alpha\beta}(\varepsilon)\left[-\frac{\partial f_0(T,\varepsilon,\mu)}{\partial\varepsilon}\right]d\varepsilon \qquad \text{Equation94}$$

$$k_{\alpha\beta}(T;\mu) = \frac{1}{e^2T\Omega}\int \bar{\sigma}_{\alpha\beta}(\varepsilon)(\varepsilon-\mu)^2\left[-\frac{\partial f_0(T;\varepsilon)}{\partial\varepsilon}\right]d\varepsilon \qquad \text{Equation95}$$

Here α and β are tensor indices; μ, Ω, and f_0 are the chemical potential, unit cell volume and the Fermi-Dirac distribution function, respectively. In these calculations, the relaxation time was set to $\tau \sim 0.5 \times 10^{-15} s$, which was also used for similar systems such as FeRhCrSi and FeRhCrGe QHAs [19]. Here, the two-current model was used to compute the total Seebeck coefficient and electrical conductivity of the majority and minority spin channels, which is given as [149]:

$$S = \frac{S_\uparrow\,\sigma_\uparrow + S_\downarrow\,\sigma_\downarrow}{\sigma_\uparrow + \sigma_\downarrow} \qquad \text{Equation96}$$

where $S_{\uparrow}$ ($S_{\downarrow}$) and $\sigma_{\uparrow}$ ($\sigma_{\downarrow}$) refer to the Seebeck coefficient and electrical conductivity for the majority (minority) spin channels, respectively.

The total Seebeck coefficient (*S*) as a function of the chemical potential at 300 K and 800 K is presented in Figures. 29(a, b). From this figure, one can notice that the total Seebeck coefficient values increase as the temperatures increases. The maximum values of *S* are obtained at 800 K with values of 42.8 μV/K and -52.5 μV/K for the *p*-type VTiRhSn and *n*-type VTiRhSi alloys, respectively. Figures 29 (c, d) present the electrical conductivity (σ) as a function of the chemical potential at 300 K and 800 K. The values of the *n*-type electrical conductivity, σ, are found to be higher than those of the *p*-type. In addition, the effect of temperature on σ values are found to be marginal. Moreover, Figures. 29 (e, f) show that κ_e has a similar behavior to σ (*n*-type κ_e values are higher than those of the *p*-type). This is ascribed to the direct relation between the electrical conductivity and electronic thermal conductivity (κ_e), which is estimated by Wiedemann-Franz equation ($\kappa_e = L\sigma T$). However, κ_e values are found to increase by increasing the temperature. The power factor (*PF*) is depicted in Figures. 29(g, h), where the values are found to increase by raising the temperature. The maximum *PF* values are found to be 16.1×10^{11}, 9.2×10^{11} and 5.4×10^{11} $Wm^{-1}K^{-2}$ at 800 K for VTiRhSi, VTiRhGe, and VTiRhSn alloys, respectively. The *PF* values of VTiRhSi, VTiRhGe alloys are found to be higher than that of CoNbMnAl QHA (6.9×10^{11} Wm^{-1} K^{-2} s^{-1}) [123].

To find the figure of merit (*ZT*) of the studied alloys, the lattice thermal conductivity (κ_l) was calculated using Slack's formula, which is one of the reliable techniques to compute κ_l value as follows [132]:

$$\kappa_l = A\frac{\bar{M}\Theta_D^3 V^{1/3}}{\gamma^2 n^{2/3} T} \qquad \text{Equation97}$$

Here $A = \frac{2.43\times10^{-6}}{1-\frac{0.514}{\gamma}+\frac{0.228}{\gamma^2}}$ [137], and $\bar{M}$, Θ_D, V, γ, n and T are the average atomic mass, Debye temperature, volume per atom, Grüneisen parameter, number of atoms in the primitive unit cell, and temperature, respectively. Based on the elastic constant calculations, the Debye temperature and the Grüneisen parameter are calculated using the following equations [137], [150]:

$$\Theta_D = \frac{h}{k_B}\left(\frac{3n\rho N_A}{4\pi M}\right)^{1/3} v_m \qquad \text{Equation98}$$

$$v_m = \left[\frac{1}{3}\left(\frac{2}{v_t^3}+\frac{1}{v_l^3}\right)\right]^{-1/3} \qquad \text{Equation99}$$

$$v_l = \sqrt{\frac{3B+4G}{3\rho}} \qquad \text{Equation100}$$

$$v_t = \sqrt{\frac{G}{\rho}} \qquad \text{Equation101}$$

$$\gamma = \frac{9-12(v_t/v_l)^2}{2+4(v_t/v_l)^2} \qquad \text{Equation102}$$

The parameters h, ρ, N_A, k_B, and M refer to the Planck constant, density, Avogadro's number, Boltzmann constant, molecular weight, respectively, while v_m, v_l and v_t refer to the average, transverse, and longitudinal sound velocities, respectively. The Debye temperature of VTiRhZ (Z=Si, Ge, Sn) alloys are found to be 445.1 K, 384.2 K and 357.3 K, respectively, see Table 12. From this table, one can see that the Debye temperature decreases by decreasing the average sound velocities, in agreement with previous calculations of Co_2MnAl, Co_2MnGa, and Co_2MnIn [118].

Table 12. The Debye temperature $\boldsymbol{\Theta_D}$ (K), average sound velocity $\boldsymbol{v_m}$ (m/s), transverse sound velocity $\boldsymbol{v_t}$ (m/s), longitudinal sound velocity $\boldsymbol{v_l}$ (m/s), density ρ (kg/m3), and Grüneisen parameter γ for VTiRhZ (Z= Si, Ge, Sn) QHAs.

Alloys	Θ_D	v_m	v_t	v_l	ρ	γ
VTiRhSi	445.1	3586	3196	6415	6910	2.06
VTiRhGe	384.2	3140	2795	5728	7895	2.13
VTiRhSn	357.3	3028	2700	5372	8281	1.99

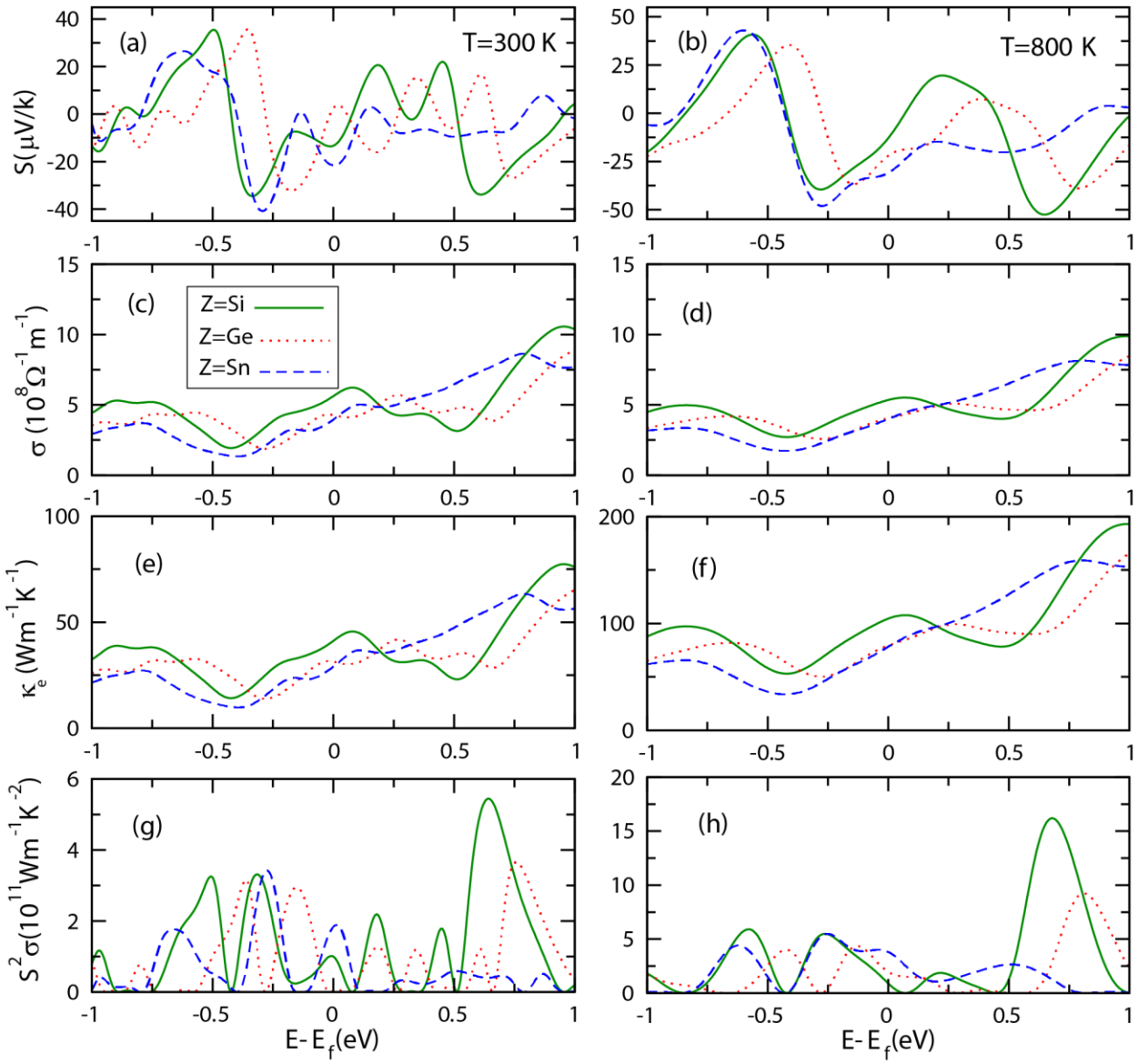

Figure 29. (a, b) the Seebeck coefficient (S), (c, d) electrical conductivity (σ), (e, f) electronic thermal conductivity ($\boldsymbol{\kappa_e}$) and (g, h) power factor PF ($S^2\sigma$) as a function of the chemical potential at temperatures of (300K, 800K) for VTiRhZ QHAs.

The lattice thermal conductivity (κ_l) was computed by utilizing the aforementioned parameters, see Figure. 30 (a). This figure shows that the lattice thermal conductivity of VTiRhZ alloys decreases as a function of temperature. The values of the lattice thermal conductivity at 300 K (800 K) are 2.77 (1.04), 2.06 (0.77) and 2.40 (0.90) $Wm^{-1}K^{-1}$ for VTiRhSi, VTiRhGe, and VTiRhSn, respectively. These values are less than those of similar structures such as CoFeCrGe

(11.01 W m^{-1} K^{-1}) and CoFeTiGe (12.26 W m^{-1} K^{-1}) at 300K [91]. The figure of merit *ZT* values are plotted as a function of the chemical potential at 300 and 800 K, see Figures. 30(b, c). This figure shows that VTiRhZ alloys exhibit higher *ZT* values at 800 K. The highest *n*-type *ZT* values of 1.13 and 0.62 were predicted for VTiRhSi and VTiRhGe, respectively, while VTiRhSn shows the highest *p*-type *ZT* value of 0.92 at 800 K. These values of *ZT* are higher than other similar previous computations of 0.45 eV and 0.41 eV at 800 K for FeRhCrSi and FeRhCrGe QHAs, respectively [19].

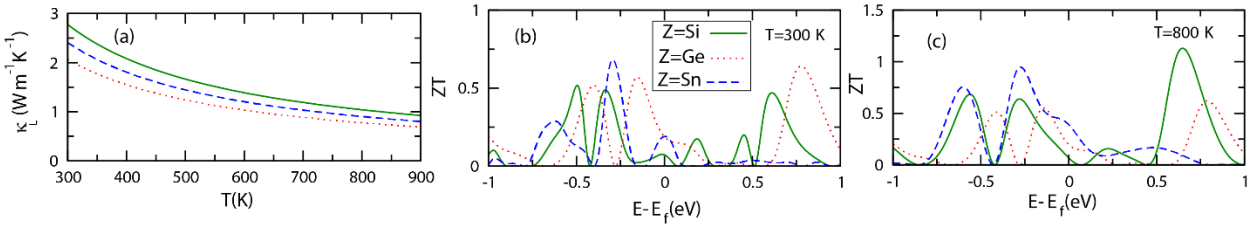

Figure 30. (a) the lattice thermal conductivity ($\boldsymbol{\kappa_L}$) as a function of the temperature for VTiRhZ alloys, and (b, c) the figure of merit (ZT) as a function of the chemical potential at (300K, 800K) for VTiRhZ alloys.

6.4 Summary

The structural, thermodynamic, dynamical, mechanical, electronic, magnetic, and thermoelectric properties of VTiRhZ (Z=Si, Ge, and Sn) quaternary Heusler alloys are investigated using DFT calculations. Based on total energy calculations, the most stable configuration for these QHAs was found to be the Y-Type-I structure. These VTiRhSi, VTiRhGe, and VTiRhSn alloys are found to exhibit a half metallic behavior with band gaps of 0.42, 0.25, and 0.12eV for, respectively. They show a ferromagnetic behavior with an integer total magnetic moment of $2\mu_B$ and a spin polarization of 100%. This half-metallic ferromagnetic behavior suggests them as prominent candidates for spintronic applications. Calculations using the semi-classical Boltzmann transport theory within the constant relaxation time approximation show that VTiRhZ (Z=Si, Ge, and Sn) QHAs possess good thermoelectric properties. The

maximum values of the power factor are 16.18×10^{11}, 9.2×10^{11} and 5.4×10^{11} $Wm^{-1}K^{-2}$ for of VTiRhSi, VTiRhGe, and VTiRhSn QHAs, respectively, at 800 K. The calculations predict the highest *ZT* values of 1.13 and 0.62 for *n*-type VTiRhSi and VTiRhGe, respectively, whereas VTiRhSn exhibits the highest *p*-type *ZT* value of 0.92 at 800 K. Thus, these alloys are also promising for potential thermoelectric applications at high temperatures.

Chapter 7: Investigations of Zr-based Quaternary Heusler Alloys for spintronic and thermoelectric applications

7.1 Introduction

With the growing need to address the energy shortage and reducing pollution, it is critical to seek for new energy resources that are progressive, clean, and environmentally friendly. The thermoelectric materials are one of the alternatives to conventional materials, which can directly convert heat into electricity[151]. The efficiency of thermoelectric materials is often measured in terms of the dimensionless figure of merit (ZT), which can be represented as[141]:

$$ZT = \frac{S^2 \sigma T}{\kappa_e + \kappa_L} \qquad \text{Equation103}$$

where S, σ , T, κ_e, and κ_L refer to the Seebeck coefficient, electrical conductivity, absolute temperature, electronic conductivity, and lattice thermal conductivity, respectively. To improve the efficiency of thermoelectric materials, the ZT value should be high enough. The high ZT materials require a high-power factor (PF= $S^2\sigma$) as well as a low thermal conductivity. However, meeting all of these parameters in one material is a challenging undertaking because a high S demands a low carrier concentration, which results in low σ [102][50]. Moreover, the high σ correlates to high κ_e, based on the Wiedemann-Franz law ($\kappa_e = L\sigma T$), where L refers to the Lorentz constant [52]. Finding the optimal balance between these parameters is essential to have a satisfactory thermoelectric response of materials. Many thermoelectric materials have been studied for their ability to operate at different temperatures. Exceptionally, the Heusler alloys have attracted significant attention for its potential use in different applications such as solar cell devices, fuel cells and thermoelectric devices. These Heusler alloys comprise of full Heusler alloys (FHAs), half Heusler alloys (HHAs) and quaternary Heusler alloys (QHAs). The three FHAs, HHAs, and QHAs groups have the chemical formulas of X_2YZ, XYZ, and XX′YZ,

respectively, where X, X′, and Y are the transition metal atoms and Z represents a main group element.

Among these alloys, the QHAs with narrow band gap energies exhibit a variety of unique physical features, including a high Curie temperature, high melting point, high Seebeck coefficient and integral magnetic moments[[100],[152],[153],[154]]. The QHAs can be crystallized in the LiMgPdSn (Y-type) structure with a space group $F\bar{4}3m$ (*no.* 216). Recently, QHAs have attracted attention due to their interesting electronic, magnetic and thermoelectric properties such as CoZrMnX (X =Al, Ga, Ge, and In) [155], CoFeCrAs [156], FeRhCrX(X=Si and Ge) [19] and CoNbMnX(X=Al, and Si)[123]. According to Fu et al. the ZT value of p-type $FeNb_{0.88}Hf_{0.12}Sb$ and $FeNb_{0.86}Hf_{0.14}Sb$ alloys are found to be 1.5 at 1200 K. Another theoretical study of CoFeCrGe and CoFeTiGe predicted ZT values of 0.71 and 0.65, respectively [91]. Based on prior computations, the Seebeck coefficient values of CoRhMnAs and CoRuMnAs alloys were reported to be 53.44 μV/K (0.50) and 44.3 μV/K (0.28), respectively [143]. Moreover, a previous calculation of CoFeMnGe alloy stated that this alloy possesses a face-center cubic structure and exhibits no phase transition beyond the melting point (1400K)[157]. In addition, FeMnScX(X=Al, Ga, and In) QHAs were predicted to have a total magnetic moment of 3 μ_B as well as a prefect spin polarization of 100% [21]. The QHAs are suggested to be the most attractive choices for thermoelectric applications due to their abundance and favorable thermoelectric properties.

The primary goal of this study is to provide two novel QHAs, namely ZrTiRhGe and ZrTiRhSn. First-principal simulations are used to study the structural, electronic, thermodynamic, mechanical, and thermoelectric properties of these two QHAs. The semi-classical Boltzmann theory is performed to study the transport coefficients (S, σ, $\kappa_e$and PF),

while the Slack model is used to compute the κ_L value. As far as we know, there have been no studies undertaken on these two novel QHAs. The remainder of the paper is arranged as follows: Section 2 contains the computational methodology. Section 3 provides the results and discussions. Finally, the conclusion is delivered in section 4.

7.2 Computational methodology

The Vienna ab initio simulation code (VASP) with projector augmented wave technique is used in these calculations [41]. The cutoff energy is chosen to be 500 eV, while the total energy tolerance is set as 10^{-8} eV. To compute the formation energy for the structure, we used a 20 × 20×20 *k*-point mesh. The results of the investigations of dynamical stability are achieved using the phonopy package [105], which is based on VASP code, and used a supercell structure of 4×4×4 with a *k*-point mesh of 4×4×4. The optimized structural parameters obtained by VASP code are then utilized to calculated the total energy by using the full-potential linearized augmented plane wave (FP-LAPW) technique as performed in the WIEN2K code [71]. The Perdew-Burke-Ernzerhof(PBE) of generalized gradient approximation (GGA) is used to address the exchange- correlation potential [43]. The total energy is selected as 10^{-4}Ry and force tolerance is set to be 1mRy/a.u. The electronic transport parameters (*S*, σ, κ_e and *PF*) of ZrTiRhZ (Z=Ge and Sn) QHAs are calculated using the BoltzTrap code [46]. The *S*, σ, κ_e parameters can be calculated as follows [101][20]:

$$S_{\alpha\beta}(T;\mu) = \frac{1}{eT\Omega\sigma_{\alpha\beta}(T;\mu)}\int \bar{\sigma}_{\alpha\beta}(\varepsilon)(\varepsilon - \mu)\left[-\frac{\partial f_0(T;\varepsilon)}{\partial\varepsilon}\right]d\varepsilon \qquad \text{Equation104}$$

$$\sigma_{\alpha\beta}(T,\mu) = \frac{1}{\Omega}\int \bar{\sigma}_{\alpha\beta}(\varepsilon)\left[-\frac{\partial f_0(T,\varepsilon,\mu)}{\partial\varepsilon}\right]d\varepsilon \qquad \text{Equation105}$$

$$k_{\alpha\beta}(T;\mu) = \frac{1}{e^2 T\Omega}\int \bar{\sigma}_{\alpha\beta}(\varepsilon)(\varepsilon-\mu)^2\left[-\frac{\partial f_0(T;\varepsilon)}{\partial\varepsilon}\right]d\varepsilon \qquad \text{Equation106}$$

where α and β are tensor indices; Ω, f_0, e, and μ refer to unit cell volume, the Fermi-Dirac distribution function, electronic charge, and the chemical potential, respectively. These electronic transport coefficients are calculated by using a *k*-point mesh of 36×36×36 and carried out by utilizing the constant relaxation time approximation(τ) of 0.5×10^{-15}s. This τ value was utilized in similar computations[[100], [19], [158]].

To calculate the κ_L, we used the Slack model which is given as [[132], [133], [137]]:

$$\kappa_l = A\frac{\bar{M}\Theta_D^3 V^{1/3}}{\gamma^2 n^{2/3} T} \qquad \text{Equation107}$$

Here *A*, $\bar{M}$, Θ_D, V, γ, *n* and *T* represent the anisotropy constant ($A = \frac{2.43\times10^{-6}}{1-\frac{0.514}{\gamma}+\frac{0.228}{\gamma^2}}$) [137], average atomic mass, acoustic-mode Debye temperature, volume per atom, Grüneisen parameter, number of atoms in the primitive unit cell, and absolute temperature, respectively. We employ the PBE functional by using VASP code to calculate the elastic constant of ZrTiRhZ (Z=Ge and Sn) QHAs to obtain the Θ_D and γ parameters. The Θ_D and γ parameters are found using the following equations[137] [158]:

$$\Theta_D = \frac{h}{k_B}\left(\frac{3n\rho N_A}{4\pi M}\right)^{1/3} v_m \qquad \text{Equation108}$$

$$\gamma = \frac{9-12(v_t/v_l)^2}{2+4(v_t/v_l)^2} \qquad \text{Equation109}$$

The parameters h, ρ, N_A, k_B, and M refer to the Planck constant, density, Avogadro's number, Boltzmann constant, molecular weight, respectively, while v_m, v_l and v_t refer to the average, transverse, and longitudinal sound velocities, respectively, given by Ref. [158]:

$$v_m = \left[\frac{1}{3}\left(\frac{2}{v_t^3} + \frac{1}{v_l^3}\right)\right]^{-1/3} \quad \text{Equation110}$$

$$v_l = \sqrt{\frac{3B+4G}{3\rho}} \quad \text{Equation111}$$

$$v_t = \sqrt{\frac{G}{\rho}} \quad \text{Equation112}$$

After finding the Θ_D and γ parameters, these finding can be used to plug into Equation (5) to obtain the κ_l.

7.3 Results and discussion

In this section, the structural, phonon, elastic, thermodynamic, electronic, magnetic, and thermoelectric properties are investigated for ZrTiRhZ (Z=Ge, Sn) quaternary Heusler alloys.

7.3.1 Structural properties

The crystal structure of the QHAs is a face-centered cubic Y-type structure (LiMgPdSn) and these alloys have the space group of $F\bar{4}3m$ (*no.* 216). Based on the symmetry, there are three types of the lattice structure in QHAs, namely Y-Type-I, Y-Type-II, Y-Type-III. The site occupations for ZrTiRhZ (Z=Ge and Sn) QHAs are calculated using the same method as the previous investigations [[91], [158], [17]] which are exhibited in Table 13 and Figure 31. Standard energy minimization approaches were used to determine the ground state structures, where Type-III structure was found to be the most stable structure for these two alloys, see Table 14.

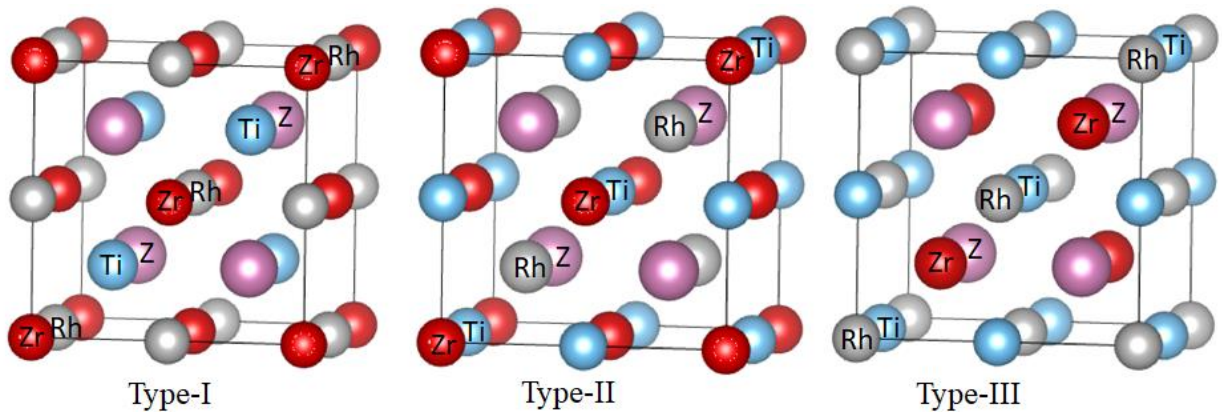

Figure 31. The conventional cells in the three types of structures (type-I, type-II, and type-III) of ZrTiRhZ (Z=Ge, Sn) quaternary Heusler alloys.

Table 13. The Wyckoff positions 4a (0,0,0), 4c (1/4,1/4,1/4), 4b (1/2.1/2,1/2), 4d (3/4,3/4,3/4) of the atoms in ZrTiRhZ quaternary Heusler alloys for three types of structures.

Y-Type	4a (0,0,0)	4c (1/4,1/4,1/4)	4b (1/2,1/2,1/2)	4d (3/4,3/4,3/4)
Type (I)	Zr	Ti	Rh	Z (Ge and Sn)
Type (II)	Zr	Rh	Ti	Z (Ge and Sn)
Type (III)	Rh	Zr	Ti	Z (Ge and Sn)

The formation energy of these two alloys is used to investigate their thermodynamic stability using the following equation:

$$E_{form} = E_{tot} - \left(E_{Zr}^{bulk} + E_{Ti}^{bulk} + E_{Rh}^{bulk} + E_{Z=Ge,Sn}^{bulk}\right) \qquad \text{Equation113}$$

Here E_{tot} refers to the total energy per formula unit of ZrTiRhGe, ZrTiRhSn alloys and $E_{\mathrm{Zr}}^{bulk}, E_{\mathrm{Ti}}^{bulk}, E_{\mathrm{Rh}}^{bulk}, E_{Z=\mathrm{Ge,Sn}}^{bulk}$ are the equilibrium total energies per atom in their individual bulk structures. The results show that ZrTiRhZ QHAs are thermodynamically stable since all of energies are negative in their type-III structure, see Table 14. The lattice parameters of ZrTiRhGe, ZrTiRhSn alloys were found to be 6.43 Å and 6.64 Å. These results are in agreement with previous theoretical calculations of VTiRhGe (6.13 Å) and VTiRhSn (6.35 Å)[100]. These results show that the lattice parameter increase as the atomic number of Z (Z=Ge and Sn) increases.

Table 14. The total and formation energies in eV of ZrTiRhZ quaternary Heusler alloys in the three types of structures.

	Y-Type-(I)	Y-Type-(II)	Y-Type-(III)
ZrTiRhGe			
Total energy (eV)	-29.47	-30.02	-30.11
Formation energy (eV)	-1.67	-1.66	-2.13
ZrTiRhSn			
Total energy (eV)	-28.40	-28.75	-29.24
Formation energy (eV)	-1.58	-1.57	-2.04

7.3.2 Phonon calculations

This subsection presents the phonon dispersion curves (PDCs), partial density of states (PDOS) of phonon and the group velocity of ZrTiRhZ (Z=Ge, Sn) in their stable Y-type-III structure, see Figure 32. The PDCs are important in understanding the dynamical stability of structures [159][160]. The four atoms of these two QHAs in their unit cell produce three acoustic and nine optical branches, resulting in a total of twelve phonon branches. The three acoustic branches have two transversal (TA1 and TA2) and one longitudinal (LA) branches. Both ZrTiRhGe and ZrTiRhSn QHAs exhibit no imaginary (negative) frequency in their PDCs. Thus, the positive phonon frequency in the PDCs reveal that these two QHAs are mechanical stability, see Figures. 32 (a) and (d). The PDOS of phonon in Figures 32 (b) and (e), which show that the low- frequency region is dominated by Rh , Zr, and Z (Z=Ge and Sn) atoms, whereas the Ti atom exhibits a higher contribution in the high frequency region of ZrTiRhZ alloys. The group velocity of these two QHAs is shown in Figures 32 (c) and (f). From these figures, one can notice that the group velocity values in the low-energy region (acoustic branches) are greater than those of the high-energy region (optical branches). Based on the relation between the lattice thermal conductivity and the group velocity ($\kappa_l \propto v_g$), the contribution of low-energy region to the κ_l should be greater than that of high-energy region.

7.3.3 Elastic properties

The elastic constants are critical quantities that can explain the material properties. These constants are inextricably linked to a variety of fundamental solid-state phenomena, including interatomic bonding, and phonon spectra. Additionally, they can describe the thermodynamic properties of materials such as the specific heat, Debye temperature, and thermal expansion. Most significantly, understanding these constants are necessary for a wide variety of applications using the mechanical properties[161].

Due to the cubic symmetry of ZrTiRhZ (Z=Ge, Sn) QHAs, there are three independent elastic parameters, namely C_{11}, C_{22}, and C_{44}. Based on these parameters, the mechanical stability of these two QHAs in their stable structure are investigated. The following formula define the Born and Huang mechanical stability criteria for cubic crystals of materials[108]:

$$C_{44} > 0\,, (C_{11} - C_{12}) > 0,\ (C_{11} + 2C_{12}) > 0, \text{and } C_{12} < B < C_{11} \qquad \text{Equation 114}$$

According to the aforementioned formula, the material is considered to be mechanically stable if these conditions are fulfilled by its elastic constants [162]. The calculated C_{11}, C_{22}, and C_{44} elastic constants are listed in Table 15, which show that both ZrTiRhGe and ZrTiRhSn QHAs are mechanically stable.

High bulk, Shear and Young's moduli indicate that the materials are strong enough to resist volume deforming or direct compressing when influenced by external stress. The bulk (Shear) modulus values of ZrTiRhGe and ZrTiRhSn alloys are found to be 142.3 (58.5) *GPa* and 135.7 (48.4) *GPa*, respectively, see Table 15. From these results, the bulk and Shear moduli of ZrTiRhGe alloy are higher than those of ZrTiRhSn, which means that ZrTiRhGe alloy is a stiff material. The Pugh's ratio (B/G) values of ZrTiRhGe and ZrTiRhSn alloys are 2.42 and 2.80, respectively, which are more than the standard value (B/G > 1.75 [116]), see Table 15. These

results indicate that these materials have a ductile nature behavior, which are in good agreement with other previous calculations [91][163]. In addition, Cauchy pressure (C_p) is calculated as $C_p=C_{12}-C_{44}$. When the material has a positive (negative) C_p value, it means that it has a metallic (covalent) bonding. The C_p values of the two QHAs are found to be positive, which means that these alloys have a metallic bonding, see Table 15. Moreover, the anisotropy (A) of these QHAs are calculated by using the cubic symmetry formula: $A=2C_{44}/(C_{11}- C_{12})$. The material is considered to be isotropic if its A value equals 1, otherwise it is anisotropic. The calculated A of ZrTiRhGe and ZrTiRhSn alloys are found to be 0.87 and 0.76, respectively, see Table 15, which means that both alloys are anisotropic.

Melting temperature (T_m) is another essential parameter, which can be obtained from the elastic constant C_{11}. The T_m can be calculated as [145][118]: $T_{melt} = \left[553\ K + \left(\frac{5.91\ K}{GPa}\right) C_{11}\right] \pm 300\ K$. The T_m values are $1794 \pm 300\ K$ and $1871 \pm 300\ K$ for ZrTiRhGe and ZrTiRhSn QHAs, respectively, see Table 15. From this table, one can notice that the T_m values increase with increasing C_{11}.

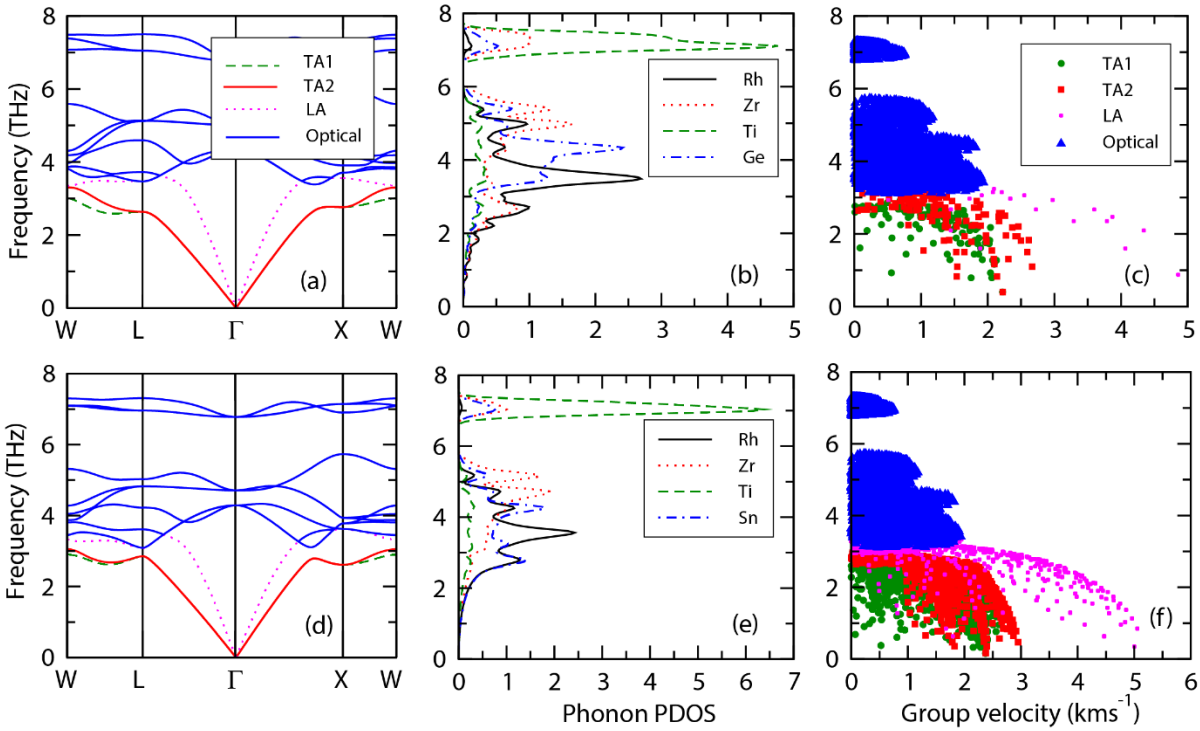

Figure 32. The phonon dispersion curves (PDCs), partial density of states (PDOS) of phonon and the group velocity of ((a)-(c)) ZrTiRhGe and ((d)-(f)) ZrTiRhSn quaternary Heusler alloys.

Table 15. The elastic constants C_{ij} (*GPa*), bulk modulus *B* (*GPa*), isotropic shear modulus *G* (GPa), Young's modulus *E* (*GPa*), Pugh's ratio *B/G*, Cauchy pressure *Cp* (*GPa*), anisotropy factor *A*, and melting temperature T_{melt} (K) for the stable Y-type-III structure of ZrTiRhZ quaternary Heusler alloys.

Physical parameter	ZrTiRhGe	VTiRhSn
C_{11} *(GPa)*	210.1	223.1
C_{12} *(GPa)*	106.4	86.8
C_{44} *(GPa)*	45.4	52.3
B (GPa)	142.3	135.7
G (GPa)	58.5	48.4
E (GPa)	153.6	130.4
B/G	2.42	2.80
C_P *(GPa)*	61	43.5
A	0.87	0.76
$T_{melt} \pm 300$(K)	1794	1871

7.3.4 Thermodynamic properties

The thermodynamic properties can provide detailed information about the materials behavior when subjected to extreme condition such as high temperatures. Here, we calculated the acoustic-mode Debye temperature (Θ_D), and Grüneisen parameter (γ) of ZrTiRhZ (Z=Ge, Sn) in their stable structure by using elastic constants, see Table 16. Moreover, the heat capacity (C_v) of ZrTiRhZ (Z=Ge, Sn) QHAs in their stable structure is calculated by using the quasi-harmonic Debye model [72], in the temperature range (0-800K), see Figure 33.

Generally, a higher Θ_D value refers to a higher thermal conductivity[161]. The Θ_D values of ZrTiRhGe and ZrTiRhSn are estimated to be 325.7 K and 338.2 K. These results are smaller than the similar QHAs investigated previously[158][161]. Another parameter is γ, which is a dimensionless parameter that determines the thermal state of material and the presence of convection. The γ values are found to be 2.13 and 1.87 for ZrTiRhGe and ZrTiRhSn, respectively. The C_v parameter can provides information about the phase transition and lattice vibrations. It is also useful in determining the nature and increase of atomic vibration owing to heat absorption. Figure 33 show that C_v (at about 300K) has the same behavior for both ZrTiRhGe and ZrTiRhSn QHAs. which increases until reaching a constant value known as the Dulong-Petit limit. These results are in agreement with previous calculations of TiVFeX(X=Al, Si, and Ge)[164]. Additionally, Table 16 presents the average (v_m), transverse (v_t), and longitudinal (v_l) sound velocities and density (ρ) of both ZrTiRhGe and ZrTiRhSn QHAs. The present finding can be used to anticipate future experiments.

Table 16. The Debye temperature $\boldsymbol{\Theta_D}$ (K), average sound velocity $\boldsymbol{v_m}$ (m/s), transverse sound velocity $\boldsymbol{v_t}$ (m/s), longitudinal sound velocity $\boldsymbol{v_l}$ (m/s), density ρ (kg/m3), and Grüneisen parameter γ for ZrTiRhZ quaternary Heusler alloys.

Physical parameter	ZrTiRhGe	VTiRhSn
Θ_D	325.7	338.2
v_m	2797	2994
v_t	2489	2677
v_l	5147	5115
ρ	7810	8176
γ	2.13	1.87

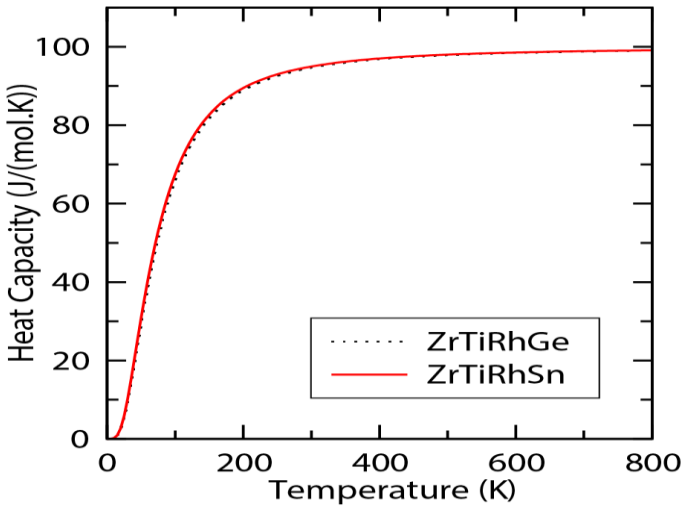

Figure 33. The heat capacity as a function of temperature for ZrTiRhZ (Z=Ge, Sn) quaternary Heusler alloys.

7.3.5 Electronic and magnetic properties

The predicted band structures and total density states (TODS) of ZrTiRhZ(Z=Ge, Sn) for majority and minority- spin channels in the stable Y-type-III structure are plotted in Figure 34. Figures 34 (a) and (c) show that the majority-spin channels in both alloys exhibit a metallic behavior, whereas the minority-spin channel is semiconducting with indirect band gaps, where the conduction band maximum is located between Γ and X points, while the valence band minimum is at Γ point. Therefore, these alloys are considered to be half-metallic, in agreement with similar ZrTiCrX(X=Al, Ga, and In) alloys [165]. The electronic structure and the energy

band gap in minority-spin channel are presented in Table 17. Figures. 34(b) and (d) depict the computed TDOS of these two QHAs, which can help to provide a better understanding of the electronic properties. From these figures, one can see that there is an absence of the electronic states at the Fermi level in the minority-spin channel unlike the case of the majority-spin channel for both alloys. Thus, these two alloys exhibit excellent spin polarization of 100%, which is calculated as:

$$P = \frac{N_{\uparrow}(E_f) - N_{\downarrow}(E_f)}{N_{\uparrow}(E_f) + N_{\downarrow}(E_f)} X\ 100 \qquad \text{Equation115}$$

Here $N_{\uparrow}(E_f)$ and $N_{\downarrow}(E_f)$ are TDOS of the majority and minority-spin density at the Fermi energy (E_f), respectively. These results confirm that these two alloys are a half-metallic behavior, which can be promising for the spintronic applications.

Table 17 presents the total and local magnetic moment of ZrTiRhZ (Z=Ge, Sn) in the stable Y-type-III structure. The total magnetic moment value was found to be 3 μ_B. These two alloys have 21 valence electrons and their total magnetic moment of 3 μ_B, which obey the Slater-Pauling equation as follows:

$$M_{tot} = (Z_{tot} - 21)\,\mu_B \qquad \text{Equation116}$$

Here M_{tot} is the total magnetic moment and Z_{tot} refers to the number of the total valence electrons. The values of local magnetic moment of Zr, Ti, Rh, Ge and Sn were found to be ferromagnetically coupled. In addition, the Ti atom in two ZrTiRhGe and ZrTiRhSn alloys exhibits the highest local magnetic moment of 1.59 μ_B and 1.58 μ_B, see Table 17.

One of the approaches for estimating the Curie temperature is to use the linear relationship between Curie temperature and total magnetic moments, as shown in the following equation [[125],[115],[126]]:

$$T_C = 23 + 181M_{tot} \qquad \text{Equation117}$$

The ZrTiRhZ(Z=Ge, Sn) in the stable Y-type-III structure have a Curie temperature of 566K, which is greater than the ambient temperature. As a result, these two alloys are suitable for spintronic devices.

Table 17. The band gap values E_g(eV), spin-polarization *P* (%), total magnetic moment M_{total} (μB), local magnetic moments per atom M_i (μB) (i = Zr, Ti, Rh, Z) and the electronic structure of ZrTiRhZ (Z= Ge, Sn) quaternary Heusler alloys.

Alloys	E_g	*P%*	M_{total} (μ_B)	M_{Zr} (μ_B)	M_{Ti} (μ_B)	M_{Rh} (μ_B)	M_Z (μ_B)	Electronic structure
ZrTiRhGe	0.98 (Minority)	100	3.00	0.40	1.59	0.18	0.01	Half-metallic
ZrTiRhSn	0.99 (Minority)	100	3.00	0.39	1.58	0.16	0.004	Half-metallic

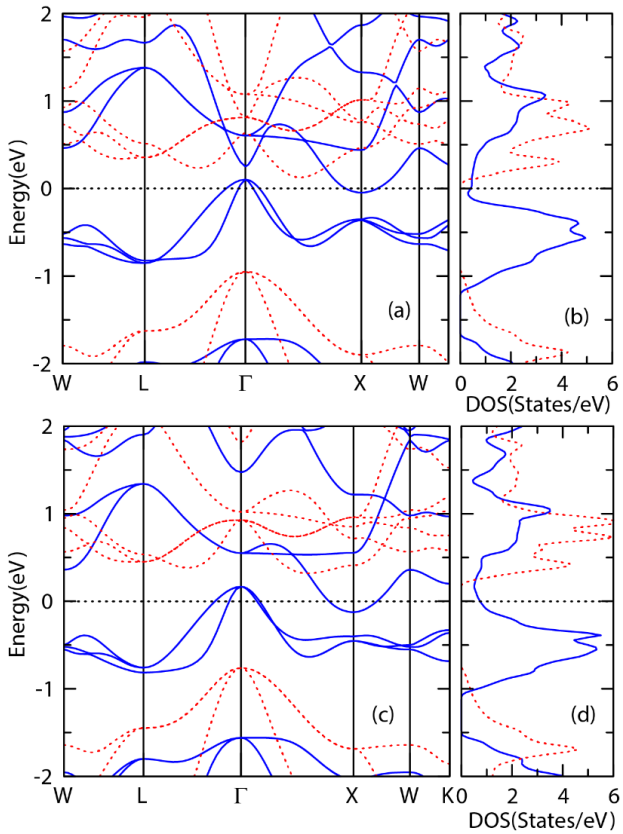

Figure 34. The electronic band structures and total density of states (TDOS) of ((a), (b)) ZrTiRhGe, and ((c), (d)) ZrTiRhSn quaternary Heusler alloys. The solid and dotted lines correspond to the majority and minority spin channels, respectively.

7.3.6 Thermoelectric properties

This subsection discusses the thermoelectric properties of ZrTiRhZ (Z=Ge, Sn) in their stable structure. The total S and σ of the majority and minority- spin channels were calculated using the two-current theory, which are represented as [149]: $S = \frac{S_\uparrow \sigma_\uparrow + S_\downarrow \sigma_\downarrow}{\sigma_\uparrow + \sigma_\downarrow}$, here $S_\uparrow$ ($S_\downarrow$) and $\sigma_\uparrow$ ($\sigma_\downarrow$) describe the Seebeck coefficient and electrical conductivity for the majority (minority) spin channels, respectively.

Figures 35 (a) and (b) show the total S as a function of the chemical potential at T=300K and 800K. These figures show that the total S values increase at a higher temperature. Around Fermi level, the ZrTiRhGe alloy has the highest S values at two the temperatures. The total σ as

a function of the chemical potential at 300K and 800K is depicted in Figures 35 (c) and (d). From these figures, one can notice that the total σ values of the *n*-type are observed to be greater than that of the *p*-type. Additionally, it is revealed that temperature has a minor influence on the total σ values. Figures 35 (e) and (f) illustrate the power factor (*PF*) as a function of the chemical potential at (T=300K and 800K). As noticed in these figures, the values of the *PF* increase with increasing temperatures. The ZrTiRhGe alloy exhibited the highest *PF* values of 33.8×10^{11} $Wm^{-1}K^{-2}$, and 27.7×10^{11} $Wm^{-1}K^{-2}$ for the *p* and *n*-types, respectively at 800K, which are higher than those of VTiRhSi (16.18×10^{11} $Wm^{-1}K^{-2}$), VTiRhGe(9.2×10^{11} $Wm^{-1}K^{-2}$), VTiRhSn(5.4×10^{11} $Wm^{-1}K^{-2}$)and CoNbMnAl(6.95×10^{11} $Wm^{-1}K^{-2}$) [100][123].

As seen in Figures 36 (a) and (b), the κ_e values behave similar to the σ values, which means that κ_e in *n*-type has higher values than the case of the *p*-type. This behavior can be related to the direct relationship between the σ and κ_e as calculated using the Wiedemann-Franz equation ($\kappa_e = L\sigma T$). However, the κ_e values are found to be higher for the higher temperature. The κ_l of ZrTiRhZ (Z=Ge, Sn) is plotted as a function of different temperatures in Figure 36 (c). From this figure, the κ_l values are found to decrease as the temperature. The κ_l values fof ZrTiRhGe alloy are found to be 2.32 W/mK and 0.87 W/mK at 300K and 800K, respectively. However, the κ_l values of ZrTiRhSn are 3.06 W/mK and 1.14 W/mK at 300K and 800K, respectively. These values are lower than those of comparable structures such as CoFeTiGe (κ_l=12.26 W/mK)[91].

Finally, the *ZT* values of ZrTiRhZ (Z=Ge, Sn) are calculated as a function of the chemical potential at two different temperatures (300K and 800K), see Figure 37 (a) and (b). Both QHAs alloys have higher values of *ZT* at 800K than those at 300K. The highest values of *ZT* at 300K (800K) are 0.81(2.92) for ZrTiRhGe alloy, while the lowest values of *ZT* at 300K

(800K) are 0.37 (0.51) are predicted for ZrTiRhSn alloy. These results are higher than that obtained for CoFeTiGe QHAs (*ZT*=0.57) in previous ab initio calculation [91]. From these results, we can predict that these two QHAs are promising materials for high-temperature thermoelectric devices.

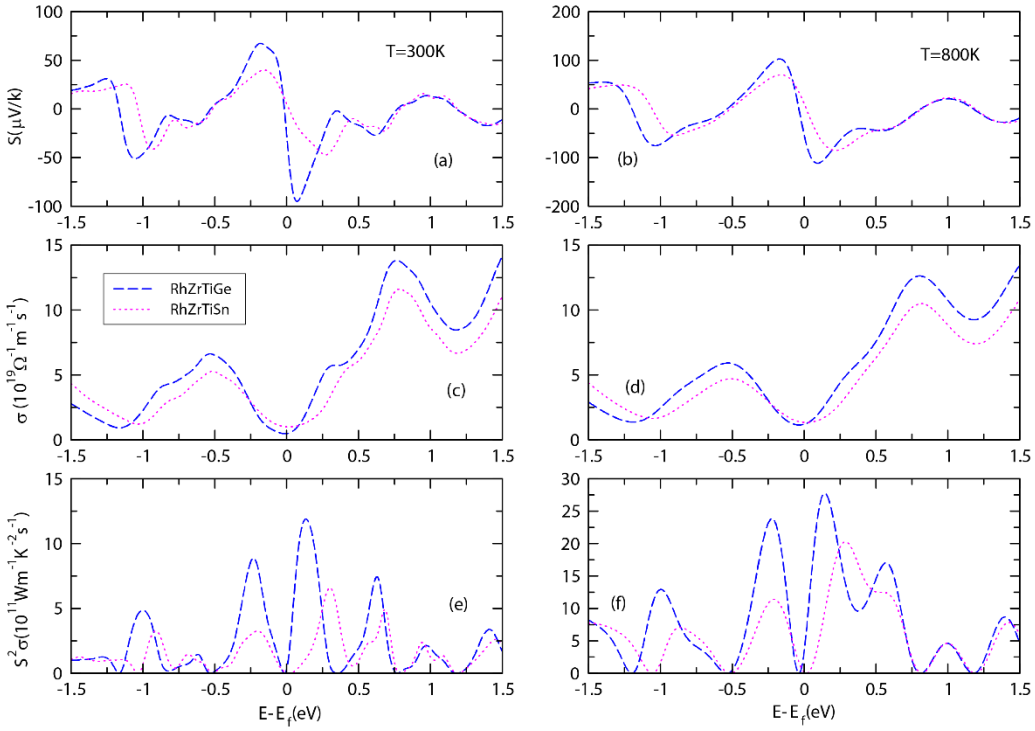

Figure 35. ((a), (b)) the Seebeck coefficient (S), ((c),(d)) electrical conductivity (σ), and ((e),(f)) power factor PF (S2σ) as a function of the chemical potential at temperatures of 300K and 800K for ZrTiRhZ quaternary Heusler alloys.

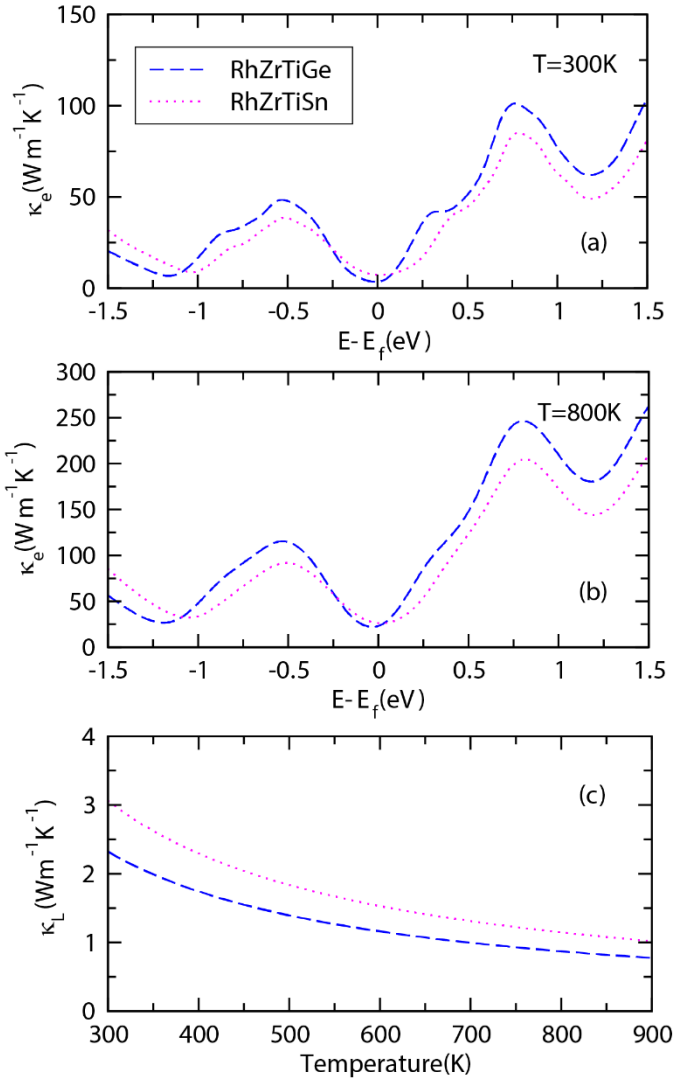

Figure 36. (a), (b) electronic thermal conductivity (κ_e) as a function of the chemical potential at 300K and 800K and (c) the lattice thermal conductivity (κ_L) as a function of the temperature for ZrTiRhZ quaternary Heusler alloys.

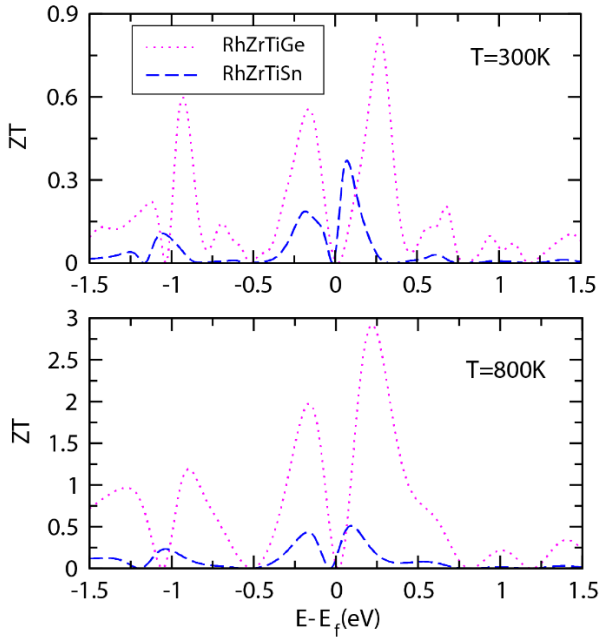

Figure 37. The figure of merit (ZT) as a function of the chemical potential at 300K and 800K for ZrTiRhZ quaternary Heusler alloys.

7.4 Summary

DFT calculations are performed to study the structural, dynamic, elastic, thermodynamic, electronic, magnetic, thermoelectric properties of ZrTiRhZ (Z=Ge, Sn) QHAs. These QHAs alloys are found to be stable in Type-III structure**.** The formation energies for these QHAs were calculated to confirm the stability and capability of experimental realization. The phonon dispersion curves (PDCs) show only positive frequencies, which mean that these alloys are dynamical stability. In addition, they are mechanically stability based on the Born and Huang criteria. The electronic structure of these two alloys shows a semiconductor behavior of 0.98 and 0.99 in minority-spin channel for ZrTiRhGe and ZrTiRhSn alloys, respectively. The ZrTiRhSn and ZrTiRhGe alloys have *ZT* values of 0.51 and 2.92 at 800K, respectively. These two new ZrTiRhZ (Z=Ge, Sn) QHAs can be a promising candidate for high-temperature thermoelectric devices.

Chapter 8: Anharmonic effects on lattice dynamics and thermal transport of two-dimensional InTe Monolayer

8.1 Introduction

Lattice vibrations are considered to be one of the frontier research topics in materials science owing to their success in predicting the dynamic, thermodynamic and thermoelectric properties of crystalline solids [166],[167]. The fundamentals of harmonic approximation (HA) have been very successful in the last few decades for predicting the thermodynamic properties. This method utilizes the second-derivative of the Born-Oppenheimer (BO) energy surface with the assumptions of relatively small atomic displacements [168]. The HA was sufficient for explaining the phonon dispersion curves, elastic properties, and lattice vibrations, but it fails to illustrate the anharmonic aspects such as the thermal expansion and the lattice thermal conductivity in crystalline solids [169].

The anharmonic effects are introduced by the cubic and the higher-order terms of the BO surface energy. These terms describe the phonon-phonon scattering, the relationship between phonon dispersion and finite temperature, the lifetimes of phonons [170],[171] as well as the lattice thermal conductivity [170]. The anharmonic effects could be implemented using the density functional perturbation theory (DFPT) [169] and finite-displacement method [172], where cubic and higher order terms in finite-displacement method can be extracted from the force-displacement data. However, this method turns to be computationally expensive when the anharmonic order is increased due to the increase in range of adjacent atomic interactions [173],[174]. In contrary, the anharmonic self-energies are considered as small perturbations in the DFTP method. This method is found to be valid only in the presence of small self-energies and it is unlikely to produce reliable results for variously anharmonic systems. Because of the

imaginary frequencies of harmonic phonons, the DFPT fails in the high-temperature phase of ferroelectric materials [[175],[176],[177],[178]].

To surmount this constraint, the anharmonic effects can be treated using the nonperturbative ab initio molecular dynamic (AIMD) methods [179],[180]. However, the drawback of these methods is due to the fact that most of them are based on Newton's equation of motion, which cannot account for the zero-point vibrations. Therefore, these methods cannot be used at low temperatures. One type of AIMD methods is the temperature-dependent effective potential (TDEP) method [181],[182], which optimizes the effective harmonic force constants at finite temperatures. This method is efficient at elevated temperatures because it permits anharmonic terms to affect the phonon eigenvectors and the internal coordinate system. Although the TDEP works properly at finite temperatures, it fails in considering the zero-point vibrations at low temperatures. An alternative method of such AIMD methods is the self-consistent phonon (SCP) theory, which includes the anharmonic effects by incorporating the quantum effect of phonons in a nonperturbative approach [[183],[184],[185]]. The development of the effective implementation of SCP theory was achieved by employing force constants of higher order harmonics that are derived by the application of compressive sensing lattice dynamics (CSLD) approach [186].

The two-dimensional group III-VI monolayers have acquired a significant attention due to their promising thermoelectric properties at high temperatures [[187],[188],[189]]. For example, Mishra, *at.al.* predicted figure of merit (ZT) values of 1.01, 0.97, 0.90 for BSe, BS, BTe monolayers, respectively[190]. Moreover, a promising ZT value of 0.85 at 1100 K was predicted for GeTe hexagonal structure monolayer[191]. In addition, the transport properties of InTe two-dimensional monolayer were investigated using semiclassical Boltzmann Transport

Equation (BTE) [192]. In this study, Çınar et al predicted a lattice thermal conductivity and a ZT value of $0.31 WK^{-1}m^{-1}$ and 3.94, respectively, at 1000K [192]. These values are promising for thermoelectric applications at high temperatures. However, lack of knowledge regarding the anharmonicity of lattice and its impact on the phonon dispersion curves and κ_l values might lead to misleading information about the thermoelectric properties. The influence of lattice anharmonicity and finite temperature on thermal transport as well as the κ_l of the InTe monolayer has not been addressed yet, which is the motivation of the current work. We utilized an effective computational method based on SCP theory [[193],[194],[195]] to compute the temperature-dependent phonon frequencies and κ_l within a supercell by utilizing the interatomic force constants (IFCs).

The paper is arranged as follows: a brief information about the methodology is presented in section 2. Section 3 presents the computational methods. The results and discussions of the temperature dependence of the anharmonic phonon, lattice dynamics, and thermodynamic parameters are presented in section 4 and conclusion is presented in section 5.

8.2 Methodology

8.2.1 Potential energy expansion:

The Hamiltonian defines the dynamic of interacting nuclear system under the Born-Oppenheimer approximation, which is given as $H=T+U$, where T and U refer to kinetic and potential energies of the system, respectively. The potential energy (U) of the system can be expanded in Taylor series with regard to the atomic displacements (u) as follows [[170],[193],[196]]:

$$U = U_0 + U_2 + U_3 + U_4 + \cdots \qquad \text{Equation118}$$

$$U_n = \frac{1}{n!}\sum_{\langle \ell,k,\mu \rangle} \Phi_{\mu_1 \ldots \mu_n}(\ell_1\kappa_1; \ldots; \ell_n\kappa_n) \times u_{\mu_1}(\ell_1\kappa_1) \cdots u_{\mu_n}(\ell_n\kappa_n) \quad \text{Equation119}$$

Here, U_n, $u_\mu(\ell k)$, and $\Phi_{\mu_1 \ldots \mu_n}(\ell_1\kappa_1; \ldots; \ell_n\kappa_n)$ are the nth-order contribution to the potential energy, the atomic displacement of the atom k in the ℓth cell along the μ direction, and is the nth-order interatomic force constant (IFC), respectively. The linear term U_1 is neglected from Eq. (1) owing to the zero atomic forces at equilibrium. Only the quadratic term U_2 is considered in the HA, whereas cubic, quartic, and higher-order terms are omitted. As a result, the Hamiltonian $U_0 = T + U_2$ can be expressed in terms of the harmonic phonon frequency ω. The dynamical matrix can be constructed to calculate the ω as [193]:

$$D_{\mu\nu}(\kappa\kappa'; \boldsymbol{q}) = \frac{1}{\sqrt{M_k M_{k'}}}\sum_{\ell'} \Phi_{\mu\nu}(\ell\kappa; \ell'\kappa') e^{iq \cdot r(\ell')} \quad \text{Equation120}$$

Here, M_k refers to the mass of atom κ, $\Phi_{\mu\nu}(\ell\kappa; \ell'\kappa')$ represents the harmonic interatomic force constant, and $r(\ell')$ represents the primitive translation vector of the lattice. The Harmonic phonon frequency can be determined by diagonalizing the dynamical matrix, which is given as [193],[72]:

$$D(q)e_{qj} = \omega_{qj}^2 e_{qj} \quad \text{Equation121}$$

Here the q and j represent the wave vector and the phonon modes index, respectively, and the ω_{qj} and e_{qj} are the phonon frequency and polarization vector of the phonon mode qj, respectively.

8.2.2 Anharmonic self-energy and self-consistent theory

The anharmonic contribution to the energy must be considered to explain the intrinsic scattering processes of phonon and the dependence of phonon frequency on temperature. The

anharmonic terms can be treated as a perturbation H' if they are small in comparison to the harmonic terms ($H_0 = T + U_0 + U_2$), which can be written as [[171],[193],[183]]:

$$H = H_0 + H' \approx H_0 + U_3 + U_4 \qquad \text{Equation122}$$

The higher-order terms (n>4) are eliminated because of their negligible contribution as compared to the cubic- and quartic-order terms. Nonetheless, nonperturbative treatment is required while drawing comparison between anharmonic and harmonic terms. The SCP theory defines a nonperturbative technique for dealing with anharmonic renormalization of phonon frequencies [[197],[193],[183]]. The Hamiltonian in Eq. (5) is modified to get the SCP equation as:

$$H = \mathcal{H}_0 + (H_0 - \mathcal{H}_0 + U_3 + U_4) = \mathcal{H}_0 + \mathcal{H}' \qquad \text{Equation123}$$

where $\mathcal{H}_0$ is the effective harmonic Hamiltonian ($\mathcal{H}_0 = \frac{1}{2}\sum_q \hbar\Omega_q \mathcal{A}_q \mathcal{A}_q^{\dagger}$) and Ω_q is phonon frequency after renormalization, $\mathcal{A}_q$ is the displacement operator, ħ refers to the Planck constant, and q represents crystal momentum vector. The calculation of free energy system can be performed as the cumulative expansion of the term $\mathcal{H}'$. In addition, the principle of variation can be implemented using the first-order of SCP theory [171],[195]. The SCP equation can therefore be obtained as follows:

$$\Omega_q^2 = \omega_q^2 + 2\Omega_q I_q \qquad \text{Equation124}$$

$$I_q = \sum_{q_1} \frac{\hbar\Phi(q;-q;q_1;-q_1)}{4\Omega_q\Omega_{q_1}} \frac{[2n(\Omega_{q_1})+1]}{2} \qquad \text{Equation125}$$

Here, $\omega_q, and\ \Phi(q;-q;q_1;-q_1)$ represent to the harmonic phonon frequency and the fourth-order IFC, and $\tilde{n}_{q_1} = \frac{1}{e^{\frac{\hbar\Omega_{q1}}{k_B T}}-1}$ represents Bose–Einstein (BE) distribution function, k_B represents

Boltzmann constant and *T* represents absolute temperature. The anharmonic phonon frequencies Ω_q can be found by using equations. (7) and (8).

8.2.3 Lattice thermal conductivity

The lattice thermal conductivity, κ_l, plays a significant role in improving the figure of merit *ZT* in thermoelectric materials. It can be calculated using the Boltzmann transport equation within the relaxation time approximation (RTA) [171],[198] as follows:

$$\kappa_l^{\mathrm{BTE}} = \frac{\hbar^2}{N_q V k_{\mathrm{B}} T^2} \sum_q \omega_q^2 v_q \otimes v_q n_q (n_q + 1) \tau_q \qquad \text{Equation126}$$

Here, $v_q = \frac{\partial \omega_q}{\partial q}$, is the group velocity, n_q is distribution function of BE, τ_q is lifetime of quasi-particle accompanying phonon frequency, and V is volume of the unit cell. The anharmonic effects are treated perturbatively. However, within the SCP theory the κ_l can be written as[171],[193]:

$$\tilde{\kappa}_l^{SCP+BTE} = \frac{\hbar^2}{N_q V k_{\mathrm{B}} T^2} \sum_q \Omega_q^2 \bar{v}_q \otimes \tilde{v}_q \tilde{n}_q (\tilde{n}_q + 1) \tilde{\tau}_q \qquad \text{Equation127}$$

$$v_q = \frac{\partial \Omega_q}{\partial q} \qquad \text{Equation128}$$

$$\tilde{n}_{\mathrm{q}} = n_q(\Omega_q) \qquad \text{Equation129}$$

v_q and $\tilde{n}_{\mathrm{q}}$ are the terms illustrating the renormalized phonon frequency Ω_q, and $\tilde{\tau}_q$ represents the renormalized lifetime illustrating the three-phonon scattering processes.

8.3 Computational methodology

The calculations are performed using the density functional theory (DFT) as implemented in VASP package [41]. The Perdew-Burke-Ernzerhof (PBE) approximation with generalized gradient approximation (GGA) was used to treat the exchange correlation functional [40]. In these computations, the plane waves were expanded up to cut-off energy of 520 eV with a total energy tolerance of 10^{-6} eV. A k-point mesh of 20 × 20 × 1 is used with the van der Waals interactions included [199]. Along the *z*-direction, a 25 Å vacuum is included to avoid interactions between adjacent layers. These optimized parameters are then utilized for the electronic band structure calculations.

The IFCs were extracted using a 5 × 5 × 1 supercell of InTe monolayer with 100 atoms. The finite-displacement method was utilized to extract the harmonic IFCs. Each atom is displaced from its equilibrium location by 0.01Å, which considers all potential nearest-neighbor interactions. The calculations were performed up to the nineth nearest neighboring atomic interaction for the cubic IFCs. The cubic interaction force constants were obtained by employing the ordinary least squares (OLS) fitting technique with the harmonic interaction force constants, as applied in the ALAMODE package[[193],[171],[200]], after the atomic forces on each of the displaced configurations were computed. The CSLD method [186] is used to extract the fourth-order IFCs. This method is based on machine learning programs that have been addressed and applied in references [171],[193]. A 5× 5 ×1 supercell of InTe monolayer was used to perform the AIMD calculations at room temperature for 14000 MD steps with a 1.5 fs time step. fifty equally spaced atomic structures were obtained from the trajectory of AIMD models. Afterwards, all of the atoms in each of the atomic structures were randomly displaced by 0.1 Å. The atomic forces for these structures were then estimated through density functional theory

calculations. These computed atomic forces were then utilized to obtain the fourth-order of interaction force constants depending on the least absolute shrinkage and selection operator (LASSO) method [170] as follows:

$$\widetilde{\Phi} = \arg\ min_{\Phi} \| A\Phi - \mathcal{F}_{\mathrm{DFT}} \|_2^2 + \alpha \parallel \Phi \parallel_1, \qquad \text{Equation130}$$

where, $\Phi = [\Phi_1, \Phi_2, \ldots, \Phi_M]^{\mathrm{T}}$ is a vector composed of *M* linearly independent IFCs, $\mathcal{F}_{\mathrm{DFT}}$ and *A* refer to the vector of atomic forces and the matrix of atomic displacements, respectively. The ideal value of the hyperparameter α is obtained by using the cross-validation (CV) method. The harmonic term of interaction force constants is fixed to the values determined by the OLS approach, where the anharmonic term of interaction force constants is optimized by the LASSO regression step. After solving Eqs. (7) and (8), the predicted fourth-order IFCs were utilized to derive the anharmonic phonon frequency(Ω_q). Thermodynamic parameters are calculated with Ω_q in this case. The specific heat capacity (Cv) is computed using the following formula:

$$C_V = \frac{k_{\mathrm{B}}}{N_q} \sum_{q,j} \left(\frac{\hbar\Omega_{q_j}}{2k_{\mathrm{B}}T}\right)^2 \mathrm{cosec}\, h^2 \left(\frac{\hbar\Omega_{q_j}}{2k_{\mathrm{B}}T}\right) \qquad \text{Equation131}$$

Here, N_q is the number of q-points.

8.4 Results and discussions

8.4.1 Structural and electronic properties

The two-dimensional InTe monolayer possesses a hexagonal crystal configuration with a space group $P\bar{6}m2$ (*no.* 187) containing four atoms in the primitive cell, as shown in Figure 38. The optimized lattice constant for this monolayer is found to be 4.39 Å, which is in agreement with previous ab initio investigations [201],[202], see Table 18. The vertical distance between telluride atoms ($d_{Te\text{-}Te}$), the distance between indium and telluride atoms (d_{In-Te}), and the vertical

distance between indium atoms (d_{In-In}) of InTe monolayer are also presented in Table18. These results are comparable to other previous calculations [201],[202]. Figure 39 presents the electronic band structure along the high symmetry k-path and the Brillouin zone used in these calculations. Figure 39 (a) shows that InTe monolayer has an indirect band gap of 1.32 eV. The valence band maximum is found to be between *K* and *Γ* high- symmetry points, whereas the conduction band minimum is located at the *Γ* high- symmetry point. The calculated band gap value (1.32 eV) is found to be in agreement with previous theoretical investigations of 1.34eV [192], 1.32eV [202] and 1.29eV [203]. Moreover, the Figure 39 (b) presents the Brillouin zone with labeled high-symmetry points.

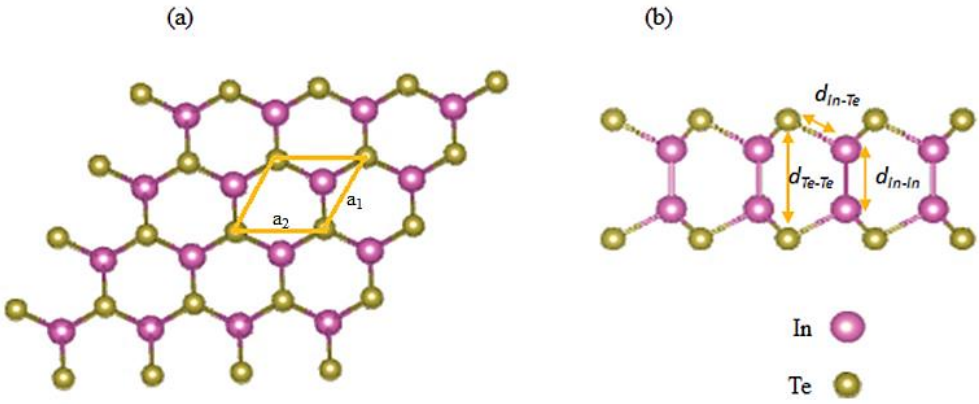

Figure 38. Crystal structure of InTe monolayer: (a) top view, the primitive unit cell is indicated in yellow, where a1=a2. (b) side view.

Table 18. The lattice constants (a), the distance between telluride atoms (d_{Te-Te}), the distance between Indium and telluride atoms (d_{In-Te}), and the distance between Indium atoms (d_{In-In}) for the InTe monolayer.

InTe monolayer	a(Å)	d_{Te-Te} (Å)	d_{In-Te} (Å)	d_{In-In}(Å)
This work	4.39	5.65	2.90	2.82
Previous calculations	4.38[201][202]	5.57[201], 5.59[202]	2.88[201], 2.88[202]	2.81[201], 2.82[202]

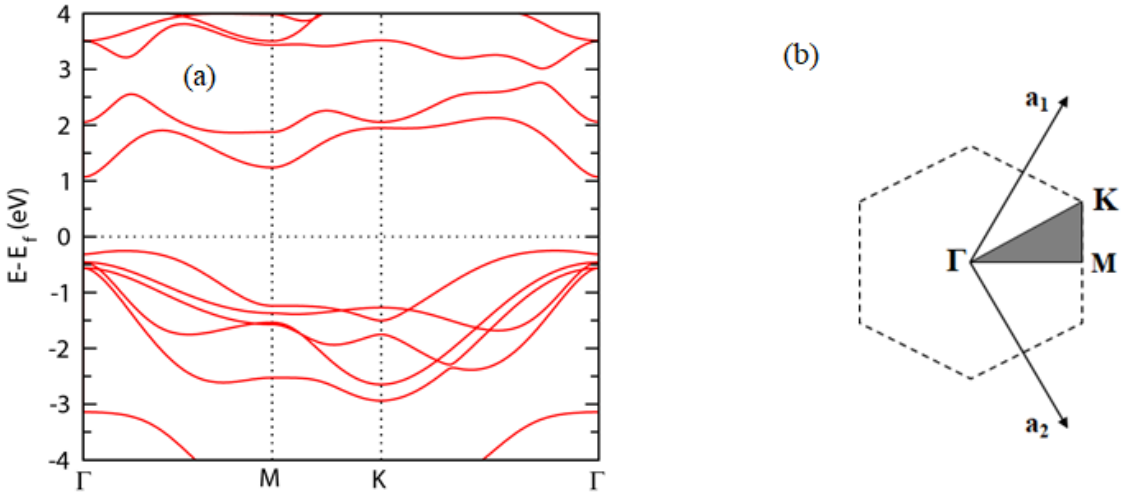

Figure 39. (a)Electronic band structure for InTe monolayer along the high-symmetry points in the first Brillouin zone (Γ–M–K–Γ) (b) The Brillouin zone with labeled high-symmetry points.

8.4.2 Anharmonic force constants using LASSO

The SCP calculations were performed using the harmonic and fourth-order IFCs. The fourth-order IFCs were determined using the LASSO technique. For these calculations, 60 displacement-force data sets were set employing AIMD. The four-fold cross-validation (CV) technique was used to examine the predictive accuracy of LASSO regression [204]. Figure 40(a) presents the relative error of the atomic forces as the hyperparameter (α) function. From this figure, one can see that the difference between the training and CV errors is negligible at large α. In addition, the CV error decreases by decreasing α and reaches to its minimum value of 1.31×10^{-6}. The value of α is represented by the dotted vertical line in the figure, which is selected as an estimate of the fourth-order IFCs to provide the optimal accuracy for the data sets. The number of non-zero fourth-order IFCs is presented in Figure. 40(b). With the optimal α value, the total number of non-zero fourth-order IFCs is found to be 4104, which is about 84% of the total number of fourth-order IFCs.

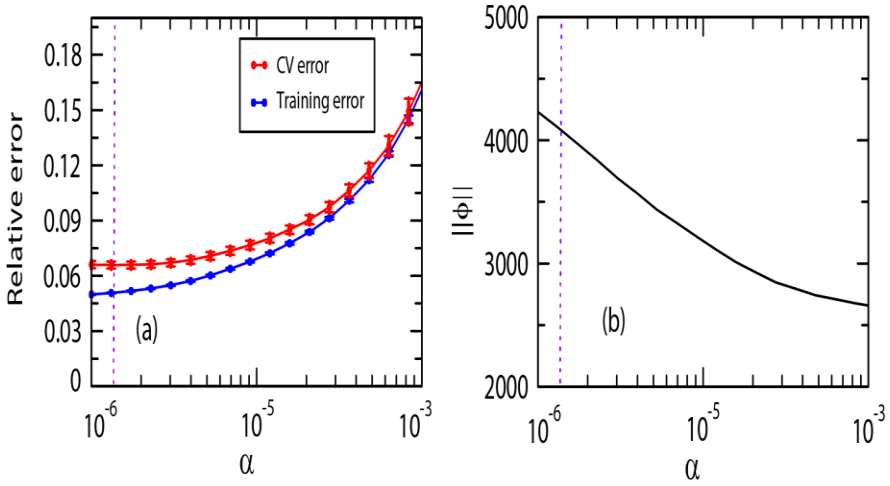

Figure 40. (a) Relative errors in the atomic forces and (b) the number of non-zero quartic IFCs with the hyperparameter (α). The dotted vertical line refers to the value of hyperparameter (α).

8.4.3 SCF at finite temperature

This subsection presents the phonon dispersion relation and total density of states (TDOS) of InTe monolayer with the Harmonic and SCF methods, see Figure 41. The calculations of the anharmonic frequencies were obtained using a 5 × 5 × 1 *q*-point grid. Through the SCP calculations, the dielectric constants and Born effective charges were used to account for the non-analytic correction. The unit cell of InTe monolayer has four atoms, which gives twelve phonon modes with three acoustic modes at lower frequencies, and nine optical modes at the higher frequencies, see Figure 41(a). The three acoustic modes consist of two in-plane (longitudinal (LA), and transverse (TA)), and one out-of-plane (flexural acoustic (FA)) modes. Near the Γ point, the LA and TA modes are linear, but the FA mode is flexural, which is comparable to other 2D monolayer materials such as ZrS_2 [170], graphene [205] InY (Y= Se, Sn, and Te) [201] and phosphorene [206]. This flexural characteristic is common in two-dimensional structures [207]. These HA findings are in a good agreement with previous theoretical results [201]. The inclusion of the fourth order IFCs in the SCP technique leads to an increase in acoustic and optical modes of InTe monolayer. The HA phonon frequency of the low-energy

optical mode at *M* point is 48.54 cm^{-1}, which increases to 50.23 cm^{-1} when the fourth order IFCs is included in the SCP method at 0 K. The phonon frequency reaches 50.71 cm^{-1} at room temperature as shown in Table 19 due to the temperature-dependent factor I_q that is included in the SCP calculations, see equations (7) and (8). Figure 41(b) presents the phonon TDOS as a function of frequency. In general, the contribution of the individual atomic masses to the lattice vibrations in a compound is crucial. The heavier atom contributes more to the phonon frequency of low-energy acoustic mode, and the lighter atom contributes more to the phonon frequency of the high-energy optical mode [208]. As seen in Figure 41 (b), there are two peaks one in the phonon frequency of low-energy acoustic mode and another in the phonon frequency of high-energy optical mode, which belong to the heavier atom of Te and the lighter atom of In, respectively.

Table 19. Phonon frequencies (cm^{-1}) of the low-energy optical modes for InTe monolayer investigated utilizing different methods.

Phonon branches	HA	SCP (at 0 K)	SCP (at 300 K)
4	48.54	50.23	50.71
6	91.34	92.15	92.22

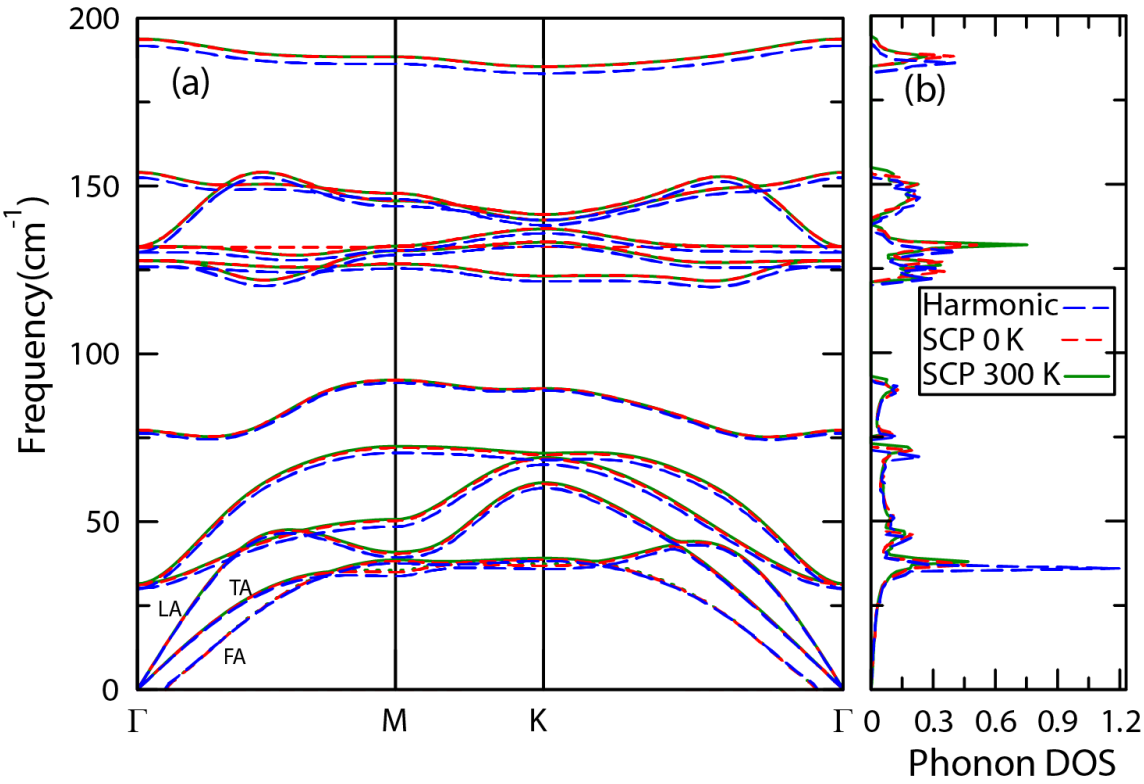

Figure 41. (a) Phonon dispersion relation and (b) the phonon DOS for the InTe monolayer obtained with the harmonic and SCP lattice dynamics.

8.4.4 Thermodynamic parameters

This subsection presents the specific heat capacity (C_v), mean-square displacement (*MSD*), total vibrational free energy (E_{total}), phonon mode-dependent Grüneisen parameter (γ_{qj}), cumulative phonon group velocities (v_g), and phonon lifetime (τ) of InTe monolayer. The C_v is a significant thermodynamic variable that contributes directly to the κ_l ($\kappa_l \propto C_v$). Figure 42(a) depicts the change in C_v with temperature using the SCP method. This figure shows low C_v values at low temperatures, which indicates a lower contribution to the κ_l. A similar behavior was reported for $BaZrS_3$ chalcogenide perovskite [209]. The *MSD* of atoms in a system is an essential parameter that indicates their divergence from the equilibrium position. The average mean-square displacement tensor of atom *k* is calculated as follows [170]:

$$\langle u_{\mu}^{2}(k)\rangle = \frac{\hbar}{M_k N_q}\sum_{q,j}\frac{1}{\Omega_{qj}}\left|e_{\mu}(k;q_j)\right|^{2}\left(\tilde{n}_{q_j}+\frac{1}{2}\right) \qquad \text{Equation132}$$

Here, M_k, and $e_{\mu}(k;q_j)$ refer to the atomic mass of atom *k*, and the corresponding atomic polarization. Figure 42(b) shows that the *MSD* value increases with temperature, which can be attributed to the enhanced heating impact at higher temperatures. This increase in *MSD* of thermal vibrations leads to a reduction in the thermal transport. The *MSD* value of In atom is found to be higher than that of Te atom due to the inverse proportionately between the mass and atomic displacement as shown in equation 13. This behavior can be more prominent when the temperature increases. In Figure 42 (c), the effect of the SCP correction on the free energy (E_{Total} = E_{QHA} + E_{SCP}) is found to be insignificant at low temperatures (below 200 K), while it becomes more pronounced at higher temperatures. For example, the SCP correction energy, decreases from -2.2×10^{-4} eV at room temperature K to -1.9×10^{-3} eV at 800K. This reduction of the total vibrational free energy upon applying the SCP correction means that the system is more stable when the quartic anharmonicity is considered. This observation emphasizes the significance of anharmonic frequency renormalization in terms of thermal properties.

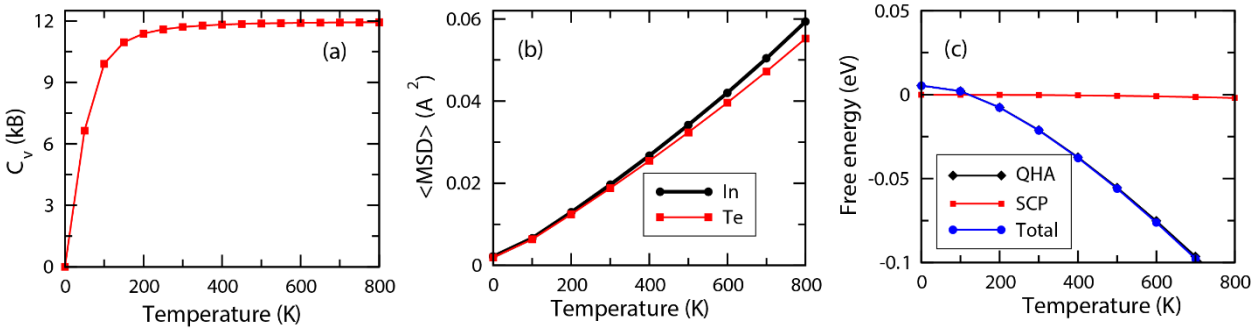

Figure 42. (a) The specific heat capacity (Cv) and (b) the MSD for the In and Te atoms, and (c) free energies within the QHA and SCP correction for the InTe monolayer with the temperature.

Another significant parameter that evaluates the anharmonicity of the structure is the γ_{qj}. Using cubic IFCs, this parameter is calculated as [170]:

$$\gamma_{qj} = -\frac{\partial(\log \omega_{qj})}{\partial(\log\ \mathrm{V})} \qquad \text{Equation133}$$

where V refers to the volume. From equation 14, a positive value of γ_{qj} means that the frequency of the phonon mode decreases as a function of volume. Figure 43 (a) shows the computed γ_{qj} of InTe monolayer as a function of phonon frequency. For the harmonic lattice dynamics, γ_{qj} has negative and positive values in the low-energy region (acoustic phonon modes), while it has a positive value in the high-energy region (optical phonon modes). This trend of γ_{qj} in the case of InTe monolayer is similar to those of other systems such as Cu_2O [210]. For the SCP, the value of γ_{qj} has a negative value in the low-frequency region and a positive value in the high-frequency region. This implies that phonon anharmonicity is greater in the case of acoustic phonon modes. According to the continuum theory [211],[210], this nature has a strong influence on the κ_l via phonon lifetime (τ) as $\tau_{qj}^{-1} \propto \gamma_{qj}^2$ [170]. Figure 43 (b) shows the v_g of InTe monolayer as a function of phonon frequency. The v_g values in the low-energy region are found to be greater than those of the high-energy region. As a result of the relation $\kappa_l \propto v_g$, the contribution of low-energy region to the κ_l should be greater than that of high-energy region. Another important variable is the phonon lifetime (τ), which is proportional to the κ_l according to $\kappa_l \propto \tau$ [171],[198]. Figure 43 (c) presents τ of InTe monolayer as a function of frequency at room temperature. From this figure, one can notice that the acoustic modes exhibit a longer phonon lifetime than that of the optical modes owing to the ratio of low phonon–phonon scattering. This indicates that the acoustic modes have a large impact in transporting most of the heat in InTe monolayer. This also plays a substantial contribution to the κ_l. The average value of τ is found to

be 13.49 ps using SCP approach, while it is found to be 1.76 ps by using the harmonic approach. This can be attributed to the three-phonon scattering processes contained in the SCP lattice dynamics [170].

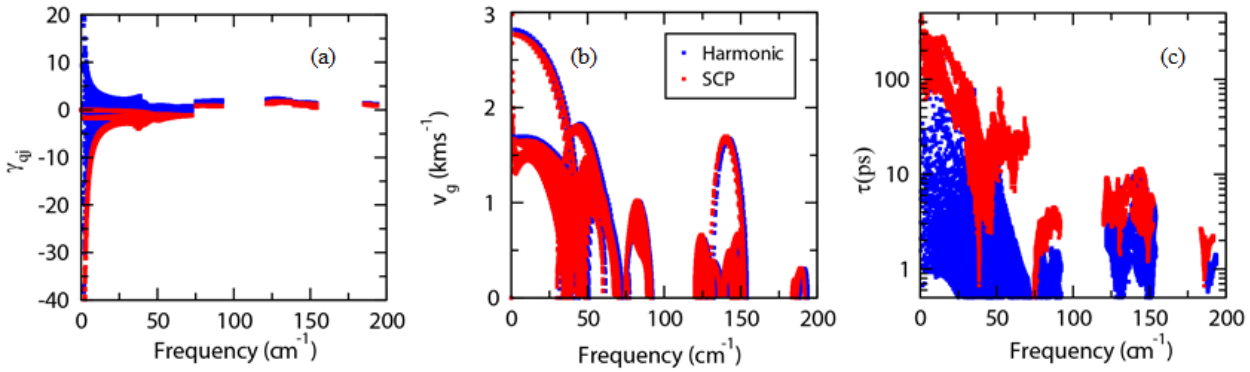

Figure 43. (a) Grüneisen parameter, (b) the cumulative phonon group velocity, and (c) the phonon lifetime of InTe monolayer with phonon frequency achieved with the harmonic and SCP lattice dynamics.

8.4.5 Lattice thermal conductivity

Figure 44 presents the lattice thermal conductivity (κ_l) spectrum and cumulative κ_l with phonon frequency of InTe monolayer at room temperature using the BTE and SCP + BTE approaches. The spectrum of thermal conductivity in Figure 44 (a) shows that there are two peaks of phonons below 70 cm^{-1}. These two peaks are located in the acoustic and low energy of optical modes. Figure 44 (b) presents the cumulative κ_l as a function of phonon frequency. This figure shows that the contributions of phonons to the total thermal conductivity are about 91% and 97% using BTE and SCP + BTE approaches, respectively with frequencies lower than 70 cm^{-1}. However, the effect of higher frequency phonons (greater than 70 cm^{-1}) is almost negligible. This indicates that the acoustic and low energy optical modes of InTe monolayer play a significant role in the κ_l value. This finding is in agreement with similar structures such as

InSe, GaSe and GaS monolayers[212] as well as silicon and germanium two-dimensional systems [213].

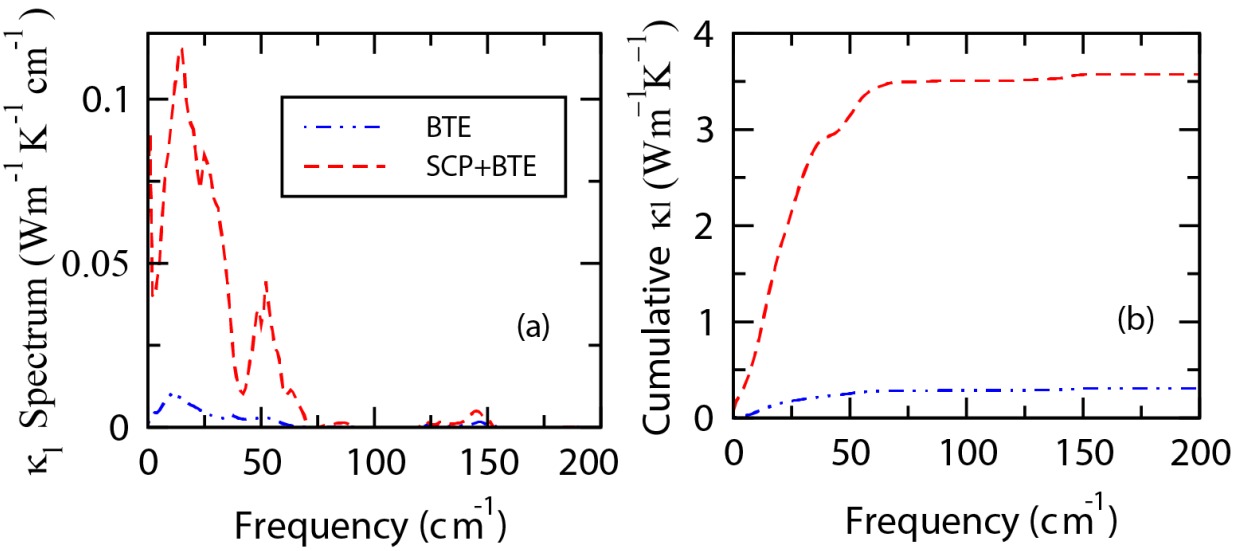

Figure 44. (a) lattice thermal conductivity (κ_l) spectrum and (b) cumulative κ_l as with the phonon frequency of InTe monolayer at room temperature K achieved with the BTE and SCP + BTE approaches.

Figure 45 depicts the contribution of several phonon branches to the κ_l values. The acoustic phonon modes (1 to 3 modes) and low energy optical modes (4 and 5 modes) have more contributions to the κ_l value than those of higher optical modes from 6 to 12 in both BTE and SCP + BTE approaches. Figure 46 presents the temperature dependence of κ_l value estimated by the standard BTE and SCP + BTE techniques of InTe monolayer. The κ_l computations were performed using a 100 ×100×1 q- points grid. The κ_l value is found to decrease as a function of temperature. in conformity with the conventional relationship ($\kappa_l \propto \frac{1}{T}$). In the case of the BTE method, the average κ_l value of InTe monolayer at room temperature was found to be 0.30 Wm^{-1} K^{-1}. This results is in agreement with a previous theoretical value of 0.31 Wm^{-1} K^{-1} using the same BTE approach [192]. The computed κ_l values using the SCP + BTE approach are found to

be significantly higher (91%) than those found using the standard BTE approach. At room temperature, the value of average κ_l is found to be 3.58 Wm^{-1} K^{-1} by using the SCP + BTE approach, which is larger than that of the experimental value of InSe (about 1.6 Wm^{-1} K^{-1})[214]. These difference in the κ_l values come from the difference in their phonon lifetime values. The higher τ values lead to the higher κ_l values, see equations (9) and (10). The SCP+BTE approach with the higher τ values also show higher κ_l values. These findings are consistent with previous anharmonic lattice dynamics calculations of $SrTiO_3$ [193], $Ba_8Ga_{16}Ge_{30}$[194], Ba_8Si_{46} [215] and SCF_3 [216] using the SCP + BTE technique, where the computed findings were in agreement with the experimental results.

The SCP + BTE technique is considered to be more reliable than the standard BTE approach to estimate the κ_l value, which leads to a more accurate prediction of the thermoelectric figure of merit and power efficiency. This can be related to the fact that the standard BTE method ignores the temperature reliance of phonon frequency and eigenvector. Therefore, it is unable to estimate the κ_l value of high-temperature phase transitions due to the imaginary modes within the HA.

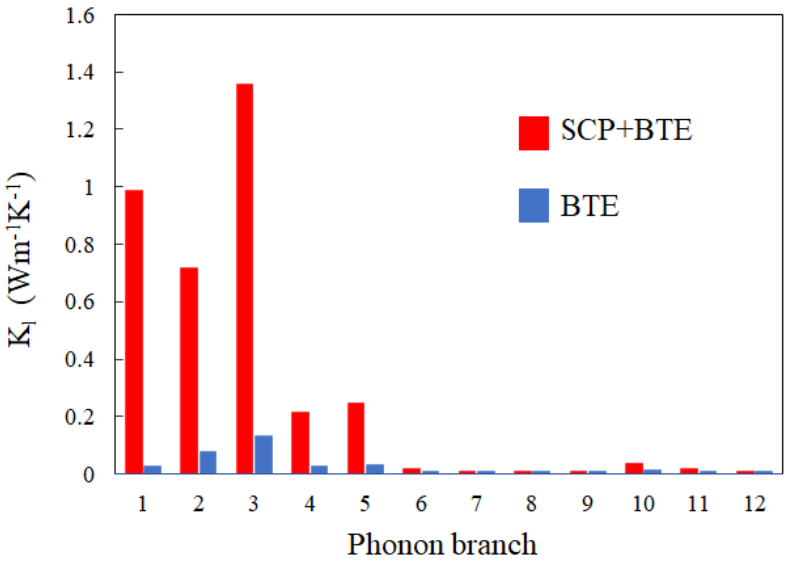

Figure 45. The total lattice thermal conductivity (κl), contribution of the phonon branches to κl for InTe monolayer at room temperature K achieved with the BTE and SCP + BTE approaches.

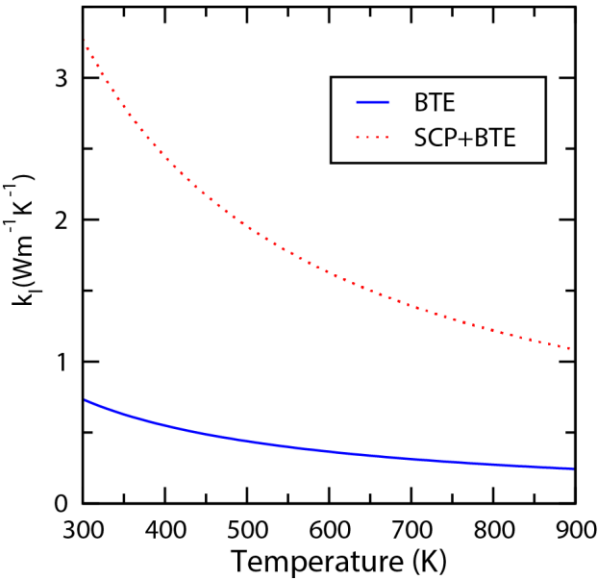

Figure 46. lattice thermal conductivity (κ_l) with temperature for the InTe monolayer achieved with the BTE and SCP + BTE approaches.

8.5 Summary

The InTe lattice dynamical properties are calculated within the SCP +BTE theory. In these calculations, the CSLD technique is used to find the higher-order harmonic IFCs. The Nonperturbative SCP approach is used to obtain the temperature-dependent phonon frequencies renormalized with the quartic anharmonicity. The phonon dispersion curves using the SCP approach are slightly higher than those of the Harmonic approach. In addition, the cumulative κ_l values demonstrated that the most contribution of heat transfer is due to acoustic modes and low energy optical modes. Using the SCP + BTE approach, the κ_l values are found to be higher than those obtained using the standard BTE approach. The SCP + BTE approach is believed to be more valid and accurate than the standard BTE approach in predicting the κ_l value. This is due to the fact that the standard BTE approach eliminates the temperature reliance of phonon frequency and eigenvector. These results provide important insights into the effect of phonon anharmonicity on the lattice dynamics, thermodynamic properties and κ_l value of the two-dimensional InTe monolayer, which play a key role in determining the thermoelectric properties.

Chapter 8: Conclusion

Calculations based on density functional theory (DFT) were undertaken to study the structural, dynamical, mechanical, electronic, and thermoelectric properties of $Cd_{1-x}Zn_xO$ alloys, VTiRhZ (Al, Ga, In, Si, Ge, Sn), ZrTiRhZ (Ge, Sn) quaternary Heusler alloys and two-dimensional monolayer InTe. Furthermore, the thermoelectric properties were evaluated utilizing the semi-classical Boltzmann transport theory. For the investigation of $Cd_{1-x}Zn_xO$ alloys, we found that the $Cd_{1-x}Zn_xO$ alloys display semiconducting performance with direct and indirect band gaps in their wurtzite and rock-salt structures, respectively, according to the hybrid GGA-mbj functional. For all structures of $Cd_{1-x}Zn_xO$ alloys, the maximum Seebeck coefficient and power factor values were obtained at 1200 K.

For the investigation of VTiRhZ and ZrTiRhZ quaternary Heusler alloys, we found that all alloys were estimated to be half-metallic ferromagnets and an excellent spin polarization of 100%. However, the spin polarization of VTiRhAl alloy was exhibited zero. In addition, the total magnetic moment of alloys was shown integer value of 2 μ_B and 3μ_B. The finding of spin polarization and the total magnetic moment makes these alloys to be promising materials for spintronic applications. The figure-of-merit values of VTiRhZ and ZrTiRhZ quaternary Heusler alloys were arranged between 0.51 and 2.92 which can be favorable materials for future thermoelectric applications.

Moreover, we investigate the influence of the lattice anharmonicity on the lattice thermal conductivity of InTe monolayer. The thermodynamic parameters are calculated by using the self-consistent phonon (SCP) theory. The κ_l value of the InTe monolayer is obtained to be 0.30 $Wm^{-1}K^{-1}$ by using the standard Boltzmann transport equation (BTE) approach, while it is 3.58 $Wm^{-1}K^{-1}$ by using SCP + BTE approach. These results confirm the importance of the

anharmonic effects on the κ_l value, where it was found to be significantly higher (91%) using the SCP + BTE approach than that obtained using the standard BTE approach.

References

1. Dresselhaus MS, Chen G, Tang MY, et al (2007) New Directions for Low-Dimensional Thermoelectric Materials. Adv Mater 19:1043–1053. https://doi.org/10.1002/ADMA.200600527

2. Rowe DM (2005) Thermoelectrics handbook: macro to nano. Thermoelectr Handb Macro to Nano 80:1014

3. Snyder GJ, Toberer ES (2008) Complex thermoelectric materials. Nat Mater 2008 72 7:105–114. https://doi.org/10.1038/nmat2090

4. Hicks LD, Harman TC, Sun X, Dresselhaus MS (1996) Experimental study of the effect of quantum-well structures on the thermoelectric figure of merit. Phys Rev B 53:R10493. https://doi.org/10.1103/PhysRevB.53.R10493

5. Hicks LD, Dresselhaus MS (1993) Effect of quantum-well structures on the thermoelectric figure of merit. Phys Rev B 47:12727. https://doi.org/10.1103/PhysRevB.47.12727
6. Flage-Larsen E, Prytz (2011) The Lorenz function: Its properties at optimum thermoelectric figure-of-merit. Appl Phys Lett 99:202108. https://doi.org/10.1063/1.3656017

7. (2001) 1. Gersten JI, Smith FW. The Physics and Chemistry of Materials. John Wiley & Sons: New York; 2001. 2001

8. Kanatzidis MG, Mahanti SD, Hogan TP (Timothy P. (2003) Chemistry, physics, and materials science of thermoelectric materials : beyond bismuth telluride. 317

9. Gao L, Zhai S, Liu R, et al (2015) Enhanced Thermoelectric Performance of CdO Ceramics Via Ba $^{2+}$ Doping. J Am Ceram Soc 98:3285–3290. https://doi.org/10.1111/jace.13780

10. Rademann K, Raghuwanshi VS, Hoell A (2016) Crystallization and Growth Mechanisms of Nanostructures in Silicate Glass: From Complete Characterization Toward Applications. From Complete Characterization Toward Applications. Elsevier Inc.

11. Zha X-Y, Gao L-J, Bai H-C, et al (2017) Optimize the thermoelectric performance of CdO ceramics by doping Zn. Chinese Phys B 26:107202. https://doi.org/10.1088/1674-1056/26/10/107202

12. Han L, Christensen D V., Bhowmik A, et al (2016) Scandium-doped zinc cadmium oxide as a new stable n-type oxide thermoelectric material. J Mater Chem A 4:12221–12231. https://doi.org/10.1039/c6ta03126a

13. Wang S, Lü Q, Li L, et al (2013) High-temperature thermoelectric properties of Cd1-xPr xO ceramics. Scr Mater 69:533–536. https://doi.org/10.1016/j.scriptamat.2013.06.018

14. Zha XY, Gao LJ, Bai HC, et al (2017) Optimize the thermoelectric performance of CdO ceramics by doping Zn. Chinese Phys B 26:. https://doi.org/10.1088/1674-1056/26/10/107202

15. Graf T, Casper F, Winterlik J, et al (2009) Crystal Structure of New Heusler Compounds. Zeitschrift für Anorg und Allg Chemie 635:976–981. https://doi.org/10.1002/zaac.200900036

16. Qin G, Wu W, Hu S, et al (2017) Effect of swap disorder on the physical properties of the quaternary Heusler alloy PdMnTiAl: A first-principles study. IUCrJ 4:506–511. https://doi.org/10.1107/S205225251700745X

17. Haleoot R, Hamad B (2019) Ab Initio Investigations of the Structural, Electronic, Magnetic, and Thermoelectric Properties of CoFeCuZ (Z = Al, As, Ga, In, Pb, Sb, Si, Sn) Quaternary Heusler Alloys. J Electron Mater 48:1164–1173. https://doi.org/10.1007/s11664-018-6833-1

18. Bainsla L, Suresh KG (2016) Equiatomic quaternary Heusler alloys: A material perspective for spintronic applications. Appl. Phys. Rev. 3:031101

19. Khandy SA, Chai J Da (2020) Thermoelectric properties, phonon, and mechanical stability of new half-metallic quaternary Heusler alloys: FeRhCrZ (Z = Si and Ge). J Appl Phys 127:165102. https://doi.org/10.1063/1.5139072

20. Kara H, Upadhyay Kahaly M, Özdoğan K (2018) Thermoelectric response of quaternary Heusler compound CrVNbZn. J Alloys Compd 735:950–958. https://doi.org/10.1016/J.JALLCOM.2017.11.022

21. Gao YC, Gao X (2015) The half-metallicity of LiMgPdSn-type quaternary Heusler alloys FeMnScZ (Z=Al, Ga, In): A first-principle study. AIP Adv 5:057157. https://doi.org/10.1063/1.4921900

22. Rao CNR, Sood AK, Subrahmanyam KS, Govindaraj A (2009) Graphene: the new two-dimensional nanomaterial. Angew Chem Int Ed Engl 48:7752–7777. https://doi.org/10.1002/ANIE.200901678

23. He J, Kanatzidis MG, Dravid VP (2013) High performance bulk thermoelectrics via a panoscopic approach. Mater Today 16:166–176. https://doi.org/10.1016/J.MATTOD.2013.05.004

24. Zhang J, Liu HJ, Cheng L, et al (2014) Phosphorene nanoribbon as a promising candidate for thermoelectric applications. Sci Reports 2014 41 4:1–8. https://doi.org/10.1038/srep06452

25. Novoselov KS, Geim AK, Morozov S V., et al (2004) Electric field in atomically thin carbon films. Science (80-) 306:666–669.

https://doi.org/10.1126/SCIENCE.1102896/SUPPL_FILE/NOVOSELOV.SOM.PDF

26. Allen MJ, Tung VC, Kaner RB (2009) Honeycomb Carbon: A Review of Graphene. Chem Rev 110:132–145. https://doi.org/10.1021/CR900070D

27. Zhu S, Wang J, Fan W (2015) Graphene-based catalysis for biomass conversion. Catal Sci Technol 5:3845–3858. https://doi.org/10.1039/C5CY00339C

28. Hoat DM (2018) Comparative study of structural, electronic, optical and thermoelectric properties of GaS bulk and monolayer. https://doi.org/101080/1478643520181560513 99:736–751. https://doi.org/10.1080/14786435.2018.1560513

29. Hoat DM, Naseri M, Hieu NN, et al (2020) Transition from indirect to direct band gap in SiC monolayer by chemical functionalization: A first principles study. Superlattices Microstruct 137:106320. https://doi.org/10.1016/J.SPMI.2019.106320

30. Naseri M, Hoat DM, Rivas-Silva JF, Cocoletzi GH (2020) Electronic structure, optical and thermoelectric properties of cadmium chalcogenides monolayers. Optik (Stuttg) 210:164567. https://doi.org/10.1016/J.IJLEO.2020.164567

31. Gomes LC, Carvalho A (2015) Phosphorene analogues: Isoelectronic two-dimensional group-IV monochalcogenides with orthorhombic structure. Phys Rev B - Condens Matter Mater Phys 92:085406. https://doi.org/10.1103/PHYSREVB.92.085406/FIGURES/6/MEDIUM

32. Zhao LD, Lo SH, Zhang Y, et al (2014) Ultralow thermal conductivity and high thermoelectric figure of merit in SnSe crystals. Nat 2014 5087496 508:373–377. https://doi.org/10.1038/nature13184

33. Zhao LD, Chang C, Tan G, Kanatzidis MG (2016) SnSe: a remarkable new thermoelectric material. Energy Environ Sci 9:3044–3060. https://doi.org/10.1039/C6EE01755J

34. Qin G, Qin Z, Fang WZ, et al (2016) Diverse anisotropy of phonon transport in two-dimensional group IV–VI compounds: A comparative study. Nanoscale 8:11306–11319. https://doi.org/10.1039/C6NR01349J

35. Hao S, Shi F, Dravid VP, et al (2016) Computational Prediction of High Thermoelectric Performance in Hole Doped Layered GeSe. Chem Mater 28:3218–3226. https://doi.org/10.1021/ACS.CHEMMATER.6B01164/SUPPL_FILE/CM6B01164_SI_001.PDF

36. Liboff RL (2003) Introductory quantum mechanics, 4. ed. Addison-Wesley, San Francisco
37. Capelle K (2006) A bird's-eye view of density-functional theory. Brazilian J Phys 36:1318–1343. https://doi.org/10.1590/S0103-97332006000700035

38. Hohenberg P, Kohn W (1964) Inhomogeneous electron gas. Phys Rev 136:B864.

https://doi.org/10.1103/PHYSREV.136.B864/FIGURE/1/THUMB

39. Kohn W, Sham LJ (1965) Self-consistent equations including exchange and correlation effects. Phys Rev 140:A1133. https://doi.org/10.1103/PHYSREV.140.A1133/FIGURE/1/THUMB

40. Kresse G, Furthmüller J (1996) Efficiency of ab-initio total energy calculations for metals and semiconductors using a plane-wave basis set. Comput Mater Sci 6:15–50. https://doi.org/10.1016/0927-0256(96)00008-0

41. Joubert D, Kresse G, Joubert D (1999) From Ultrasoft Pseudopotentials to the Projector Augmented-Wave Method First-Principles Calculations of the Electronic and Optical Properties of CH 3 NH 3 PbI 3 for Photovoltaic Applications View project One dimensional Lattice Density Functional Theory V. Artic Phys Rev B. https://doi.org/10.1103/PhysRevB.59.1758

42. Kresse G, Furthmüller J (1996) Efficient iterative schemes for *ab initio* total-energy calculations using a plane-wave basis set. Phys Rev B 54:11169. https://doi.org/10.1103/PhysRevB.54.11169

43. Perdew JP, Burke K, Ernzerhof M (1996) Generalized gradient approximation made simple. Phys Rev Lett 77:3865–3868. https://doi.org/10.1103/PhysRevLett.77.3865

44. Ahmad S, Mahanti SD, Kanatzidis MG (2005) Ab initio studies of electronic structure of defects on the Te sites in PbTe. MRS Online Proc Libr 886:161–166. https://doi.org/10.1557/PROC-0886-F04-11

45. Hurd CM (1972) The Hall Effect in Metals and Alloys. Hall Eff Met Alloy. https://doi.org/10.1007/978-1-4757-0465-5

46. Madsen GKH, Singh DJ (2006) BoltzTraP. A code for calculating band-structure dependent quantities. Comput Phys Commun 175:67–71. https://doi.org/10.1016/J.CPC.2006.03.007

47. Lin TT, Gao Q, Liu GD, et al (2019) Dynamical stability, electronic and thermoelectric properties of quaternary ZnFeTiSi Heusler compound. Curr Appl Phys 19:721–727. https://doi.org/10.1016/J.CAP.2019.03.020

48. Zha X, Gao L, Bai H, et al (2018) Towards a high thermoelectric performance in CdO ceramics by introducing multiscale scattering centers via ZnCO 3 doping. Mater Res Express 5:. https://doi.org/10.1088/2053-1591/aab5ee

49. Ding G, Gao G, Yao K (2015) High-efficient thermoelectric materials: The case of orthorhombic IV-VI compounds. Sci Rep 5:9567. https://doi.org/10.1038/srep09567

50. Han M-K, Hoang K, Kong H, et al Substitution of Bi for Sb and its Role in the

Thermoelectric Properties and Nanostructuring in Ag 1-x Pb 18 MTe 20 (M) Bi, Sb) (x) 0, 0.14, 0.3). https://doi.org/10.1021/cm703661g

51. Mukasia A, Manyali GS, Barasa H, et al (2019) Reviewers: (1) Sunipa Roy, Guru Nanak Institute of Technology (JIS Grp.), India. (2) Mohd Faizul Mohd Sabri, University of Malaya, Malaysia. (3) Djillali Bensaid. Orig Res Artic Mukasia al 2:1–7. https://doi.org/10.9734/JMSRR/2019/45389

52. Ginzburg VL (1989) Thermoelectric effects in superconductors. J Supercond 2:323–328. https://doi.org/10.1007/BF00617883

53. Wan C, Wang Y, Wang N, et al (2010) Development of novel thermoelectric materials by reduction of lattice thermal conductivity. Sci Technol Adv Mater 11:44306–44313. https://doi.org/10.1088/1468-6996/11/4/044306

54. Hamid Elsheikh M, Shnawah DA, Sabri MFM, et al (2014) A review on thermoelectric renewable energy: Principle parameters that affect their performance. Renew. Sustain. Energy Rev. 30:337–355

55. Han L, Christensen D V., Bhowmik A, et al (2016) Scandium-doped zinc cadmium oxide as a new stable n-type oxide thermoelectric material. J Mater Chem A 4:12221–12231. https://doi.org/10.1039/c6ta03126a

56. Rozale H, Bouhafs B, Ruterana P (2007) First-principles calculations of the optical band-gaps of ZnxCd1-xO alloys. Superlattices Microstruct 42:165–171. https://doi.org/10.1016/j.spmi.2007.04.007

57. Kumar P, Mathpal MC, Inwati GK, et al (2020) Optical and surface properties of Zn doped CdO nanorods and antimicrobial applications. Colloids Surfaces A Physicochem Eng Asp 605:125369. https://doi.org/10.1016/j.colsurfa.2020.125369

58. Gao L, Wang S, Liu R, et al (2016) The effect of Ni doping on the thermoelectric transport properties of CdO ceramics. J Alloys Compd 662:213–219. https://doi.org/10.1016/j.jallcom.2015.12.043

59. Gopal P, Spaldin NA (2006) Polarization, piezoelectric constants, and elastic constants of ZnO, MgO, and CdO. In: Journal of Electronic Materials. Springer, pp 538–542

60. Zhang X, Li H, Wang J (2015) Effect of sintering temperature on thermoelectric properties of CdO ceramics. J Adv Ceram 4:226–231. https://doi.org/10.1007/s40145-015-0153-1

61. OHTA S, OHTA H, KOUMOTO K (2006) Grain Size Dependence of Thermoelectric Performance of Nb-Doped SrTiO3 Polycrystals. J Ceram Soc Japan 114:102–105. https://doi.org/10.2109/jcersj.114.102

62. Harun K, Salleh NA, Deghfel B, et al (2020) DFT + U calculations for electronic, structural, and optical properties of ZnO wurtzite structure: A review. Results Phys 16:102829. https://doi.org/10.1016/j.rinp.2019.102829

63. Lalrinkima, Lahriatzuala, Rai DP, Srivastava S (2019) Strain dependence of electronic properties and effective masses of monolayer ZnO from density functional theory. In: AIP Conference Proceedings. American Institute of Physics Inc., p 30093

64. Ohtaki M, Tsubota T, Eguchi K, Arai H (1996) High-temperature thermoelectric properties of ($Zn_{1-x}Al_x$)O. J Appl Phys 79:1816–1818. https://doi.org/10.1063/1.360976

65. Feng Y, Jiang X, Ghafari E, et al (2018) Metal oxides for thermoelectric power generation and beyond. Adv Compos Hybrid Mater 1:114–126. https://doi.org/10.1007/s42114-017-0011-4

66. Ji L (2018) Metal oxide-based thermoelectric materials. Met Oxides Energy Technol 49–72. https://doi.org/10.1016/B978-0-12-811167-3.00003-1

67. Qu X, Wang W, Lv S, Jia D (2011) Thermoelectric properties and electronic structure of Al-doped ZnO. Solid State Commun 151:332–336. https://doi.org/10.1016/j.ssc.2010.11.020

68. Blöchl PE (1994) Projector augmented-wave method. Phys Rev B 50:17953–17979. https://doi.org/10.1103/PhysRevB.50.17953

69. Han F (2012) Projector-Augmented Plane-Wave Method. Probl Solid State Phys with Solut 50:391–396. https://doi.org/10.1142/9789814365031_0023

70. Kart HH, Uludogan M, Cagin T (2009) DFT studies of sulfur induced stress corrosion cracking in nickel. Comput Mater Sci 44:1236–1242. https://doi.org/10.1016/j.commatsci.2008.08.007

71. Blaha P, Schwarz K, Sorantin P, Trickey SB (1990) Full-potential, linearized augmented plane wave programs for crystalline systems. Comput Phys Commun 59:399–415. https://doi.org/10.1016/0010-4655(90)90187-6

72. Togo A, Tanaka I (2015) First principles phonon calculations in materials science. Scr Mater 108:1–5. https://doi.org/10.1016/j.scriptamat.2015.07.021

73. Karzel H, Potzel W, Köfferlein M, et al (1996) Lattice dynamics and hyperfine interactions in ZnO and ZnSe at high external pressures

74. Yao G, An X, Lei H, et al (2013) Electronic and Optical Properties of Rocksalt CdO: A first-Principles Density-Functional Theory Study. Model Numer Simul Mater Sci 03:16–19. https://doi.org/10.4236/mnsms.2013.31b005

75. Zaoui A, Zaoui M, Kacimi S, et al (2010) Stability and electronic properties of ZnxCd1-xO alloys. Mater Chem Phys 120:98–103. https://doi.org/10.1016/j.matchemphys.2009.10.027

76. Spooner KB, Ganose AM, Scanlon DO (2020) Assessing the limitations of transparent conducting oxides as thermoelectrics. J Mater Chem A 8:11948–11957. https://doi.org/10.1039/d0ta02247k

77. Berrezoug HI, Merad AE, Zerga A, Hassoun ZS (2015) Simulation and Modeling of Structural Stability, Electronic Structure and Optical Properties of ZnO. In: Energy Procedia. Elsevier Ltd, pp 1517–1524

78. Jefferson PH, Hatfield SA, Veal TD, et al (2008) Bandgap and effective mass of epitaxial cadmium oxide. Appl Phys Lett 92:022101. https://doi.org/10.1063/1.2833269

79. Özgür Ü, Alivov YI, Liu C, et al (2005) A comprehensive review of ZnO materials and devices. J. Appl. Phys. 98:1–103

80. Feng W, Cui S, Hu H, et al (2010) Structural stabilities and electronic and elastic properties of CdO: A first-principles study. Phys status solidi 247:2202–2206. https://doi.org/10.1002/pssb.201046098

81. Scheidemantel J, Ambrosch-Draxl C, Thonhauser T, et al (2003) Transport coefficients from first-principles calculations. Phys Rev B - Condens Matter Mater Phys 68:125210. https://doi.org/10.1103/PhysRevB.68.125210

82. Wang S, Liu F, Lü Q, et al (2013) The effect of Er3+ doping on the structure and thermoelectric properties of CdO ceramics. J Eur Ceram Soc 33:1763–1768. https://doi.org/10.1016/j.jeurceramsoc.2013.02.025

83. Skaftouros S, Özdoğan K, Şaşioğlu E, Galanakis I (2013) Generalized Slater-Pauling rule for the inverse Heusler compounds. Phys Rev B - Condens Matter Mater Phys 87:024420. https://doi.org/10.1103/PhysRevB.87.024420

84. Galanakis I, Mavropoulos P, Dederichs PH (2006) Electronic structure and Slater-Pauling behaviour in half-metallic Heusler alloys calculated from first principles. J Phys D Appl Phys 39:765–775. https://doi.org/10.1088/0022-3727/39/5/S01

85. De Groot RA, Mueller FM, Engen PGV, Buschow KHJ (1983) New class of materials: Half-metallic ferromagnets. Phys Rev Lett 50:2024–2027. https://doi.org/10.1103/PhysRevLett.50.2024

86. Hamad B (2017) Theoretical Investigations of the Thermoelectric Properties of Fe2NbGa1−xAlx (x = 0, 0.25, 0.5) Alloys. J Electron Mater 46:6595–6602. https://doi.org/10.1007/s11664-017-5721-4

87. Joshi G, Poudel B (2016) Efficient and Robust Thermoelectric Power Generation Device Using Hot-Pressed Metal Contacts on Nanostructured Half-Heusler Alloys. J Electron Mater 45:6047–6051. https://doi.org/10.1007/s11664-016-4692-1

88. Guo X, Ni Z, Liang Z, Luo H (2018) Magnetic semiconductors and half-metals in FeRu-based quaternary Heusler alloys. Comput Mater Sci 154:442–448. https://doi.org/10.1016/j.commatsci.2018.08.023

89. Zhang L, Cheng ZX, Wang XT, et al (2018) First-Principles Investigation of Equiatomic Quaternary Heusler Alloys NbVMnAl and NbFeCrAl and a Discussion of the Generalized Electron-Filling Rule. J Supercond Nov Magn 31:189–196. https://doi.org/10.1007/s10948-017-4182-6

90. Barman CK, Mondal C, Pathak B, Alam A (2019) Quaternary Heusler alloy: An ideal platform to realize triple point fermions. Phys Rev B 99:045144. https://doi.org/10.1103/PhysRevB.99.045144

91. Haleoot R, Hamad B (2020) Thermodynamic and thermoelectric properties of CoFeYGe (Y = Ti, Cr) quaternary Heusler alloys: First principle calculations. J Phys Condens Matter 32:075402. https://doi.org/10.1088/1361-648X/ab5321

92. Alijani V, Ouardi S, Fecher GH, et al (2011) Electronic, structural, and magnetic properties of the half-metallic ferromagnetic quaternary Heusler compounds CoFeMnZ (Z=Al, Ga, Si, Ge). Phys Rev B - Condens Matter Mater Phys 84:224416. https://doi.org/10.1103/PhysRevB.84.224416

93. Guo R, Liu G, Wang X, et al (2016) First-principles study on quaternary Heusler compounds ZrFeVZ (Z = Al, Ga, In) with large spin-flip gap. RSC Adv 6:109394–109400. https://doi.org/10.1039/c6ra18873g

94. Alijani V, Winterlik J, Fecher GH, et al (2011) Quaternary half-metallic Heusler ferromagnets for spintronics applications. Phys Rev B - Condens Matter Mater Phys 83:184428. https://doi.org/10.1103/PhysRevB.83.184428

95. Li Y, Liu GD, Wang XT, et al (2017) First-principles study on electronic structure, magnetism and half-metallicity of the NbCoCrAl and NbRhCrAl compounds. Results Phys 7:2248–2254. https://doi.org/10.1016/j.rinp.2017.06.047

96. Bainsla L, Suresh KG, Nigam AK, et al (2014) High spin polarization in CoFeMnGe equiatomic quaternary Heusler alloy. J Appl Phys 116:203902. https://doi.org/10.1063/1.4902831

97. Eliassen SNH, Katre A, Madsen GKH, et al (2017) Lattice thermal conductivity of TixZryHf1-x-yNiSn half-Heusler alloys calculated from first principles: Key role of nature of phonon modes. Phys Rev B 95:045202. https://doi.org/10.1103/PhysRevB.95.045202

98. Lue CS, Chen CF, Lin JY, et al (2007) Thermoelectric properties of quaternary Heusler alloys Fe2 VAl1-x Six. Phys Rev B - Condens Matter Mater Phys 75:064204. https://doi.org/10.1103/PhysRevB.75.064204

99. Yabuuchi S, Okamoto M, Nishide A, et al (2013) Large seebeck coefficients of fe2tisn and fe2tisi: First-principles study. Appl Phys Express 6:025504. https://doi.org/10.7567/APEX.6.025504

100. Alqurashi H, Hamad B (2021) Magnetic structure, mechanical stability and thermoelectric properties of VTiRhZ (Z = Si, Ge, Sn) quaternary Heusler alloys: first-principles calculations. Appl Phys A Mater Sci Process 127:1–11. https://doi.org/10.1007/S00339-021-04949-0/FIGURES/6

101. Lin TT, Gao Q, Liu GD, et al (2019) Dynamical stability, electronic and thermoelectric properties of quaternary ZnFeTiSi Heusler compound. Curr Appl Phys 19:721–727. https://doi.org/10.1016/j.cap.2019.03.020

102. Alqurashi H, Haleoot R, Pandit A, Hamad B (2021) Investigations of the electronic, dynamical, and thermoelectric properties of Cd1-xZnxO alloys: First-principles calculations. Mater Today Commun 28:102511. https://doi.org/10.1016/j.mtcomm.2021.102511

103. Mushtaq M, Sattar MA, Dar SA (2020) Phonon phase stability, structural, mechanical, electronic, and thermoelectric properties of two new semiconducting quaternary Heusler alloys <scp>CoCuZrZ</scp> (Z = Ge and Sn). Int J Energy Res 44:5936–5946. https://doi.org/10.1002/er.5373

104. Berri S Computational Study of Structural, Electronic, Elastic, Half-Metallic and Thermoelectric Properties of CoCrScZ (Z=Al, Si, Ge, and Ga) Quaternary Heusler Alloys. https://doi.org/10.1007/s10948-020-05638-4/Published

105. Kresse G, Hafner J (1993) Ab initio molecular dynamics for liquid metals. Phys Rev B 47:558–561. https://doi.org/10.1103/PhysRevB.47.558

106. Madsen GKH, Singh DJ (2006) BoltzTraP. A code for calculating band-structure dependent quantities. Comput Phys Commun 175:67–71. https://doi.org/10.1016/j.cpc.2006.03.007

107. Hoat DM, Naseri M (2020) Electronic and thermoelectric properties of RbYSn half-Heusler compound with 8 valence electrons: Spin-orbit coupling effect. Chem Phys 528:110510. https://doi.org/10.1016/j.chemphys.2019.110510

108. Dynamical theory of crystal lattices - CERN Document Server

109. Hill R (1952) The elastic behaviour of a crystalline aggregate. Proc Phys Soc Sect A 65:349–354. https://doi.org/10.1088/0370-1298/65/5/307

110. Zhao JS, Gao Q, Li L, et al (2017) First-principles study of the structure, electronic, magnetic and elastic properties of half-Heusler compounds LiXGe (X = Ca, Sr and Ba). Intermetallics 89:65–73. https://doi.org/10.1016/j.intermet.2017.04.011

111. Wang X, Cheng Z, Wang J, Liu G (2016) A full spectrum of spintronic properties demonstrated by a C1b-type Heusler compound Mn2Sn subjected to strain engineering. J Mater Chem C 4:8535–8544. https://doi.org/10.1039/c6tc02526a

112. Semari F, Boulechfar R, Dahmane F, et al (2020) Phase stability, mechanical, electronic and thermodynamic properties of the Ga3Sc compound: An ab-initio study. Inorg Chem Commun 122:108304. https://doi.org/10.1016/j.inoche.2020.108304

113. Berri S First-Principles Calculations to Investigate the Structural, Electronic, and Half-Metallic Properties of Ti 2 RhSn 1-x Si x , Ti 2 RhSn 1-x Ge x , and Ti 2 RhGe 1-x Si x (x = 0, 0.25, 0.5, 0.75, and 1) Quaternary Heusler Alloys. https://doi.org/10.1007/s10948-018-4952-9

114. Candan A (2019) Magnetic, Electronic, Mechanic, Anisotropic Elastic and Vibrational Properties of Antiferromagnetic Ru2TGa (T = Cr, Mn, and Co) Heusler Alloys. J. Electron. Mater. 48:7608–7622

115. Jain R, Jain VK, Chandra AR, et al (2018) Study of the Electronic Structure, Magnetic and Elastic Properties and Half-Metallic Stability on Variation of Lattice Constants for CoFeCrZ (Z = P, As, Sb) Heusler Alloys. J Supercond Nov Magn 31:2399–2409. https://doi.org/10.1007/s10948-017-4460-3

116. Chen X-R, Zhong M-M, Feng Y, et al (2015) Structural, electronic, elastic, and thermodynamic properties of the spin-gapless semiconducting Mn $_2$ CoAl inverse Heusler alloy under pressure. Phys status solidi 252:2830–2839. https://doi.org/10.1002/pssb.201552389

117. Lv Y, Zhang X, Jiang W (2018) Phase stability, elastic, anisotropic properties, lattice dynamical and thermodynamic properties of B12M (M=Th, U, Np, Pu) dodecaborides. Ceram Int 44:128–135. https://doi.org/10.1016/j.ceramint.2017.09.147

118. Wu SC, Fecher GH, Shahab Naghavi S, Felser C (2019) Elastic properties and stability of Heusler compounds: Cubic Co 2 YZ compounds with L 2 1 structure. J Appl Phys 125:082523. https://doi.org/10.1063/1.5054398

119. Levin EM (2016) Charge carrier effective mass and concentration derived from combination of Seebeck coefficient and Te 125 NMR measurements in complex tellurides. Phys Rev B 93:245202. https://doi.org/10.1103/PhysRevB.93.245202

120. Gao Q, Opahle I, Zhang H (2019) High-throughput screening for spin-gapless semiconductors in quaternary Heusler compounds. Phys Rev Mater 3:024410. https://doi.org/10.1103/PhysRevMaterials.3.024410

121. Beth Stearns M (1977) Simple explanation of tunneling spin-polarization of Fe, Co, Ni and its alloys. J. Magn. Magn. Mater. 5:167–171

122. Galanakis I, Dederichs PH, Papanikolaou N (2002) Slater-Pauling behavior and origin of the half-metallicity of the full-Heusler alloys. Phys Rev B - Condens Matter Mater Phys 66:1–9. https://doi.org/10.1103/PhysRevB.66.174429

123. Mubarak AA, Saad S, Hamioud F, Al-Elaimi M (2021) Structural, thermo-elastic, electro-magnetic and thermoelectric attributes of quaternary CoNbMnX (X = Al, Si) Heusler alloys. Solid State Sci 111:106397. https://doi.org/10.1016/j.solidstatesciences.2020.106397

124. Berri S (2017) Electronic structure and half-metallicity of the new Heusler alloys PtZrTiAl, PdZrTiAl and Pt0.5Pd0.5ZrTiAl. Chinese J Phys 55:195–202. https://doi.org/10.1016/J.CJPH.2016.10.017

125. Candan A, Uğur G, Charifi Z, et al (2013) Electronic structure and vibrational properties in cobalt-based full-Heusler compounds: A first principle study of Co2MnX (X = Si, Ge, Al, Ga). J Alloys Compd 560:215–222. https://doi.org/10.1016/j.jallcom.2013.01.102

126. Elahmar MH, Rached H, Rached D, et al (2015) Structural, mechanical, electronic and magnetic properties of a new series of quaternary Heusler alloys CoFeMnZ (Z=Si, As, Sb): A first-principle study. J Magn Magn Mater 393:165–174. https://doi.org/10.1016/j.jmmm.2015.05.019

127. Sofo JO, Mahan GD (1994) Optimum band gap of a thermoelectric material. Phys Rev B 49:4565–4570. https://doi.org/10.1103/PhysRevB.49.4565

128. Gibbs ZM, Kim HS, Wang H, Snyder GJ (2015) Band gap estimation from temperature dependent Seebeck measurement - Deviations from the 2e|S|maxTmax relation. Appl Phys Lett 106:022112. https://doi.org/10.1063/1.4905922

129. Hasdeo EH, Krisna LPA, Hanna MY, et al (2019) Optimal band gap for improved thermoelectric performance of two-dimensional Dirac materials. J Appl Phys 126:035109. https://doi.org/10.1063/1.5100985

130. Guo SD (2016) Thermoelectric properties of half-Heusler ZrNiPb by using first principles calculations. RSC Adv 6:47953–47958. https://doi.org/10.1039/C6RA08461C

131. Shrivastava D, Sanyal SP (2019) Theoretical study of structural, electronic, phonon and thermoelectric properties of KScX (X=Sn and Pb) and KYX (X=Si and Ge) half-Heusler compounds with 8 valence electrons count. J Alloys Compd 784:319–329. https://doi.org/10.1016/J.JALLCOM.2019.01.050

132. Hong AJ, Li L, He R, et al (2016) Full-scale computation for all the thermoelectric property parameters of half-Heusler compounds. Sci Rep 6:1–12

https://doi.org/10.1038/srep22778

133. Ma H, Yang CL, Wang MS, et al (2019) Effect of M elements (M = Ti, Zr, and Hf) on thermoelectric performance of the half-Heusler compounds MCoBi. J Phys D Appl Phys 52:255501. https://doi.org/10.1088/1361-6463/ab137d

134. Dhakal C, Aryal S, Sakidja R, Ching WY (2015) Approximate lattice thermal conductivity of MAX phases at high temperature. J Eur Ceram Soc 35:3203–3212. https://doi.org/10.1016/j.jeurceramsoc.2015.04.013

135. Haleoot R, Hamad B (2020) Thermoelectric properties of doped β-InSe by Bi: First principle calculations. Phys B Condens Matter 587:412105. https://doi.org/10.1016/j.physb.2020.412105

136. Nag S, Saini A, Singh R, Kumar R (2020) Ultralow lattice thermal conductivity and anisotropic thermoelectric performance of AA stacked SnSe bilayer. Appl Surf Sci 512:145640. https://doi.org/10.1016/J.APSUSC.2020.145640

137. Slack GA (1973) Nonmetallic crystals with high thermal conductivity. J Phys Chem Solids 34:321–335. https://doi.org/10.1016/0022-3697(73)90092-9

138. Disalvo FJ (1999) Thermoelectric cooling and power generation. Science (80-.). 285:703–706

139. Kim HS, Liu W, Chen G, et al (2015) Relationship between thermoelectric figure of merit and energy conversion efficiency. Proc Natl Acad Sci U S A 112:8205–8210. https://doi.org/10.1073/pnas.1510231112

140. Pandit A, Hamad B (2021) Thermoelectric and lattice dynamics properties of layered MX (M = Sn, Pb; X = S, Te) compounds. Appl Surf Sci 538:147911. https://doi.org/10.1016/j.apsusc.2020.147911

141. Alqurashi H, Haleoot R, Pandit A, Hamad B (2021) Investigations of the electronic, dynamical, and thermoelectric properties of Cd1-xZnxO alloys: First-principles calculations. Mater Today Commun 28:102511. https://doi.org/10.1016/J.MTCOMM.2021.102511

142. Nishino Y, Deguchi S, Mizutani U (2006) Thermal and transport properties of the Heusler-type Fe2 VAl1-x Gex ($0 \leq x \leq 0.20$) alloys: Effect of doping on lattice thermal conductivity, electrical resistivity, and Seebeck coefficient. Phys Rev B - Condens Matter Mater Phys 74:115115. https://doi.org/10.1103/PhysRevB.74.115115

143. Seh AQ, Gupta DC (2019) Exploration of highly correlated Co-based quaternary Heusler alloys for spintronics and thermoelectric applications. Int J Energy Res 43:er.4853. https://doi.org/10.1002/er.4853

144. Benacchio G, Titov I, Malyeyev A, et al (2019) Evidence for the formation of nanoprecipitates with magnetically disordered regions in bulk <math xmlns. Phys Rev B 99:184422. https://doi.org/10.1103/PhysRevB.99.184422

145. Ilkhani M, Boochani A, Amiri M, et al (2020) Mechanical stability and thermoelectric properties of the PdZrTiAl quaternary Heusler: A DFT study. Solid State Commun 308:113838. https://doi.org/10.1016/j.ssc.2020.113838

146. Jia LY, Xu JL, Zhao RB, et al (2017) New Quaternary Half-Metallic Materials of the Z t − 28 Rule in LiMgPdSn-Type Heusler Alloys. J Supercond Nov Magn 2017 314 31:1067–1072. https://doi.org/10.1007/S10948-017-4280-5

147. Chen XQ, Podloucky R, Rogl P (2006) Ab initio prediction of half-metallic properties for the ferromagnetic Heusler alloys Co2MSi (M=Ti,V,Cr). J Appl Phys 100:113901. https://doi.org/10.1063/1.2374672

148. Geilhufe M, Nayak SK, Thomas S, et al (2015) Effect of hydrostatic pressure and uniaxial strain on the electronic structure of Pb1-xSnxTe. Phys Rev B - Condens Matter Mater Phys 92:235203. https://doi.org/10.1103/PhysRevB.92.235203

149. Singh S, Gupta DC (2019) Lanthanum based quaternary Heusler alloys LaCoCrX (X = Al, Ga): Hunt for half-metallicity and high thermoelectric efficiency. Results Phys 13:102300. https://doi.org/10.1016/j.rinp.2019.102300

150. Li C, Wang Z (2012) Computational modelling and ab initio calculations in MAX phases – I. Adv Sci Technol Mn+1AXn Phases 197–222. https://doi.org/10.1533/9780857096012.197

151. Jiang Q, Wan R, Zhang Z, et al (2021) High thermoelectric performance of half-Heusler Zr X Pb (X= Ni, Pd, and Pt) compounds from first principle calculation. J Phys Condens Matter 33:. https://doi.org/10.1088/1361-648X/AC1E48

152. Galanakis I, Özdoğan K, Şaşioğlu E (2016) Spin-filter and spin-gapless semiconductors: The case of Heusler compounds. AIP Adv 6:055606. https://doi.org/10.1063/1.4943761

153. Shakil M, Sadia H, Zeba I, et al (2021) First-principles study of structural, mechanical, thermal, electronic and magnetic properties of highly spin-polarized quaternary Heusler alloy CoYVSn. Solid State Commun 325:114157. https://doi.org/10.1016/J.SSC.2020.114157

154. Choudhary R, Kashyap A, Paudyal D, et al (2020) Non-Heisenberg magnetism in a quaternary spin-gapless semiconductor. J Magn Magn Mater 497:166058. https://doi.org/10.1016/J.JMMM.2019.166058

155. Hossain MA, Rahman MT, Khatun M, Haque E (2018) Structural, elastic, electronic, magnetic and thermoelectric properties of new quaternary Heusler compounds CoZrMnX

(X=Al, Ga, Ge, In). Comput Condens Matter 15:31–41. https://doi.org/10.1016/J.COCOM.2018.03.006

156. Bhat TM, Gupta DC (2018) First-principles study of high spin-polarization and thermoelectric efficiency of ferromagnetic CoFeCrAs quaternary Heusler alloy. J Magn Magn Mater 449:493–499. https://doi.org/10.1016/J.JMMM.2017.10.081

157. Bainsla L, Suresh KG, Nigam AK, et al (2014) High spin polarization in CoFeMnGe equiatomic quaternary Heusler alloy. J Appl Phys 116:203902. https://doi.org/10.1063/1.4902831

158. Alqurashi H, Haleoot R, Hamad B (2021) First-principles investigations of the electronic, magnetic and thermoelectric properties of VTiRhZ (Z= Al, Ga, In) Quaternary Heusler alloys. Mater Chem Phys 125685. https://doi.org/10.1016/J.MATCHEMPHYS.2021.125685

159. Cai Y, Bai Z, Yang M, Feng YP (2012) Effect of interfacial strain on spin injection and spin polarization of Co2CrAl/NaNbO3/Co2CrAl magnetic tunneling junction. Europhys Lett 99:37001. https://doi.org/10.1209/0295-5075/99/37001

160. Khandy SA, Islam I, Gupta DC, et al (2019) Lattice dynamics, mechanical stability and electronic structure of Fe-based Heusler semiconductors. Sci Rep 9:. https://doi.org/10.1038/S41598-018-37740-Y

161. Mohamedi MW, Chahed A, Amar A, et al (2016) Ab-initio study of structural, elastic, thermal, electronic and magnetic properties of quaternary Heusler alloys CoMnCrZ (Z = Al, As, Si, Ge). EPJB 89:267. https://doi.org/10.1140/EPJB/E2016-70183-6

162. Kanti Biswas S, Gnanasekaran T, Kumar Ghorai T, et al (2020) Structural, elastic, electronic, and magnetic properties of MnNbZ (Z = As, Sb) and FeNbZ (Z = Sn, Pb) semi-Heusler alloys. Mater Res Express 7:116527. https://doi.org/10.1088/2053-1591/ABCC86

163. Hoat DM, Hoang DQ, Binh NTT, et al (2021) First principles analysis of the half-metallic ferromagnetism, elastic and thermodynamic properties of equiatomic quaternary Heusler compound CoCrRhSi. Mater Chem Phys 257:123695. https://doi.org/10.1016/J.MATCHEMPHYS.2020.123695

164. Gencer A, Surucu O, Usanmaz D, et al (2021) Equiatomic quaternary Heusler compounds TiVFeZ (Z=Al, Si, Ge): Half-metallic ferromagnetic materials. J Alloys Compd 883:160869. https://doi.org/10.1016/J.JALLCOM.2021.160869

165. Yan PL, Zhang JM, Zhou B, Xu KW (2016) The structural, electronic, magnetic and mechanical properties of quaternary Heusler alloys ZrTiCrZ (Z = Al, Ga, In, Si, Ge, Sn): a first-principles study. J Phys D Appl Phys 49:255002. https://doi.org/10.1088/0022-3727/49/25/255002

166. Electrons and Phonons: The Theory of Transport Phenomena in Solids - J.M. Ziman - Google Books. https://books.google.com/books?hl=en&lr=&id=UtEy63pjngsC&oi=fnd&pg=PA1&ots=JQTbPKtTB2&sig=z_-71l6Y5H8Q5X5mvWGchzLWP7E#v=onepage&q&f=false. Accessed 13 Oct 2021

167. Ziman JM (2001) PHONONS. Electrons and Phonons 1–61. https://doi.org/10.1093/ACPROF:OSO/9780198507796.003.0001

168. Wallace DC (2005) Thermodynamics of Crystals. Am J Phys 40:1718. https://doi.org/10.1119/1.1987046

169. Baroni S, Gironcoli S de, Corso AD, Giannozzi P (2001) Phonons and related crystal properties from density-functional perturbation theory. Rev Mod Phys 73:515. https://doi.org/10.1103/RevModPhys.73.515

170. Pandit A, Hamad B (2021) The effect of finite-temperature and anharmonic lattice dynamics on the thermal conductivity of ZrS 2 monolayer: self-consistent phonon calculations. J Phys Condens Matter J Phys Condens Matter 33:425405. https://doi.org/10.1088/1361-648X/ac1822

171. Terumasa T, Shinji T (2018) First-Principles Lattice Dynamics Method for Strongly Anharmonic Crystals. https://doi.org/107566/JPSJ87041015 87:. https://doi.org/10.7566/JPSJ.87.041015

172. Esfarjani K, Stokes HT (2008) Method to extract anharmonic force constants from first principles calculations. Phys Rev B 77:144112. https://doi.org/10.1103/PhysRevB.77.144112

173. Lang G, Karch K, Schmitt M, et al (1999) Anharmonic line shift and linewidth of the Raman mode in covalent semiconductors. Phys Rev B 59:6182. https://doi.org/10.1103/PhysRevB.59.6182

174. Bonini N, Lazzeri M, Marzari N, Mauri F (2007) Phonon Anharmonicities in Graphite and Graphene. Phys Rev Lett 99:176802. https://doi.org/10.1103/PhysRevLett.99.176802

175. Pawley GS, Cochran W, Cowley RA, Dolling G (1966) Diatomic Ferroelectrics. Phys Rev Lett 17:753. https://doi.org/10.1103/PhysRevLett.17.753

176. Holt M, Zschack P, Hong H, et al (2001) X-Ray Studies of Phonon Softening in <span class. Phys Rev Lett 86:3799. https://doi.org/10.1103/PhysRevLett.86.3799

177. Delaire O, Ma J, Marty K, et al (2011) Giant anharmonic phonon scattering in PbTe. Nat Mater 2011 108 10:614–619. https://doi.org/10.1038/nmat3035

178. Ghosez PSH, Gonze X, Michenaud JP (2011) AB initio phonon dispersion curves and interatomic force constants of barium titanate.

http://dx.doi.org/101080/00150199808009159 206–207:205–217. https://doi.org/10.1080/00150199808009159

179. Wang CZ, Chan CT, Ho KM (1990) Tight-binding molecular-dynamics study of phonon anharmonic effects in silicon and diamond. Phys Rev B 42:11276. https://doi.org/10.1103/PhysRevB.42.11276

180. Koker N de (2009) Thermal Conductivity of MgO Periclase from Equilibrium First Principles Molecular Dynamics. Phys Rev Lett 103:125902. https://doi.org/10.1103/PhysRevLett.103.125902

181. Hellman O, Abrikosov IA, Simak SI (2011) Lattice dynamics of anharmonic solids from first principles. Phys Rev B 84:180301. https://doi.org/10.1103/PhysRevB.84.180301

182. Hellman O, Abrikosov IA (2013) Temperature-dependent effective third-order interatomic force constants from first principles. Phys Rev B - Condens Matter Mater Phys 88:144301. https://doi.org/10.1103/PHYSREVB.88.144301/FIGURES/6/MEDIUM

183. Werthamer NR (1970) Self-Consistent Phonon Formulation of Anharmonic Lattice Dynamics. Phys Rev B 1:572. https://doi.org/10.1103/PhysRevB.1.572

184. Hooton DJ (2010) The use of a model in anharmonic lattice dynamics. https://doi.org/101080/14786435808243224 3:49–54. https://doi.org/10.1080/14786435808243224

185. Souvatzis P, Eriksson O, Katsnelson MI, Rudin SP (2008) Entropy driven stabilization of energetically unstable crystal structures explained from first principles theory. Phys Rev Lett 100:095901. https://doi.org/10.1103/PHYSREVLETT.100.095901/FIGURES/2/MEDIUM

186. Zhou F, Nielson W, Xia Y, Ozoliņš V (2014) Lattice Anharmonicity and Thermal Conductivity from Compressive Sensing of First-Principles Calculations. Phys Rev Lett 113:185501. https://doi.org/10.1103/PhysRevLett.113.185501

187. Hung NT, Nugraha ART, Saito R (2017) Two-dimensional InSe as a potential thermoelectric material. Appl Phys Lett 111:092107. https://doi.org/10.1063/1.5001184

188. Hung NT, Nugraha ART, Yang T, et al (2018) Thermoelectric performance of monolayer InSe improved by convergence of multivalley bands. J Appl Phys 125:082502. https://doi.org/10.1063/1.5040752

189. Zeng J, He X, Liang S-J, et al (2018) Experimental Identification of Critical Condition for Drastically Enhancing Thermoelectric Power Factor of Two-Dimensional Layered Materials. Nano Lett 18:7538–7545. https://doi.org/10.1021/ACS.NANOLETT.8B03026

190. Pushkar Mishra, Deobrat Singh, Yogesh Sonvane, Rajeev Ahuja (2020) Two-dimensional

boron monochalcogenide monolayer for thermoelectric material. Sustain Energy Fuels 4:2363–2369. https://doi.org/10.1039/D0SE00004C

191. Shangguan H, Han L, Zhang T, et al (2019) Thermoelectric Properties of Two-Dimensional Gallium Telluride. J Electron Mater 2019 489 48:5988–5994. https://doi.org/10.1007/S11664-019-07323-2

192. Çınar MN, Sargın GÖ, Sevim K, et al (2021) Ballistic thermoelectric transport properties of two-dimensional group III-VI monolayers. Phys Rev B 103:165422. https://doi.org/10.1103/PhysRevB.103.165422

193. Tadano T, Tsuneyuki S (2015) Self-consistent phonon calculations of lattice dynamical properties in cubic SrTiO3 with first-principles anharmonic force constants. Phys Rev B - Condens Matter Mater Phys 92 https://doi.org/10.1103/PHYSREVB.92.054301/FIGURES/1/THUMBNAIL

194. Tadano T, Tsuneyuki S (2018) Quartic Anharmonicity of Rattlers and Its Effect on Lattice Thermal Conductivity of Clathrates from First Principles. Phys Rev Lett 120:105901. https://doi.org/10.1103/PhysRevLett.120.105901

195. Oba Y, Tadano T, Akashi R, Tsuneyuki S (2019) First-principles study of phonon anharmonicity and negative thermal expansion in ScF3. Phys Rev Mater 3:. https://doi.org/10.1103/PHYSREVMATERIALS.3.033601/FIGURES/1/THUMBNAIL

196. Paulatto L, Errea I, Calandra M, Mauri F (2015) First-principles calculations of phonon frequencies, lifetimes, and spectral functions from weak to strong anharmonicity: The example of palladium hydrides. Phys Rev B 91:054304. https://doi.org/10.1103/PhysRevB.91.054304

197. Horner H (1967) Lattice dynamics of quantum crystals. Zeitschrift für Phys 1967 2051 205:72–89. https://doi.org/10.1007/BF01326300

198. Li W, Carrete J, Katcho NA, Mingo N (2014) ShengBTE: A solver of the Boltzmann transport equation for phonons. Comput Phys Commun 185:1747–1758. https://doi.org/10.1016/J.CPC.2014.02.015

199. Klimeš J, Bowler DR, Michaelides A (2011) Van der Waals density functionals applied to solids. Phys Rev B 83:195131. https://doi.org/10.1103/PhysRevB.83.195131

200. Tadano T, Gohda Y, Tsuneyuki S (2014) Anharmonic force constants extracted from first-principles molecular dynamics: applications to heat transfer simulations. J Phys Condens Matter 26:225402. https://doi.org/10.1088/0953-8984/26/22/225402

201. Shafique A, Shin Y-H (2020) The effect of non-analytical corrections on the phononic thermal transport in InX (X = S, Se, Te) monolayers. Sci Reports 2020 101 10:1–10. https://doi.org/10.1038/s41598-020-57644-0

202. Min-Shan Li, Kai-Xuan Chen, Dong-Chuan Mo, Shu-Shen Lyu (2019) Predicted high thermoelectric performance in a two-dimensional indium telluride monolayer and its dependence on strain. Phys Chem Chem Phys 21:24695–24701. https://doi.org/10.1039/C9CP04666F

203. Demirci S, Avazlı N, Durgun E, Cahangirov S (2017) Structural and electronic properties of monolayer group III monochalcogenides. Phys Rev B 95:115409. https://doi.org/10.1103/PhysRevB.95.115409

204. Terumasa T, Shinji T (2018) First-Principles Lattice Dynamics Method for Strongly Anharmonic Crystals. https://doi.org/107566/JPSJ87041015 87:. https://doi.org/10.7566/JPSJ.87.041015

205. Lindsay L, Broido DA, Mingo N (2010) Flexural phonons and thermal transport in graphene. Phys Rev B 82:115427. https://doi.org/10.1103/PhysRevB.82.115427

206. Qin G, Yan Q-B, Qin Z, et al (2015) Anisotropic intrinsic lattice thermal conductivity of phosphorene from first principles. Phys Chem Chem Phys 17:4854–4858. https://doi.org/10.1039/C4CP04858J

207. Neto AHC, Guinea F, Peres NMR, et al (2009) The electronic properties of graphene. Rev Mod Phys 81:109. https://doi.org/10.1103/RevModPhys.81.109

208. AS N, Z R, J M, W L (2020) Lattice Thermal Transport in Monolayer Group 13 Monochalcogenides MX (M = Ga, In; X = S, Se, Te): Interplay of Atomic Mass, Harmonicity, and Lone-Pair-Induced Anharmonicity. Inorg Chem 59:14899–14909. https://doi.org/10.1021/ACS.INORGCHEM.0C01407

209. Osei-Agyemang E, Balasubramanian G (2019) Understanding the Extremely Poor Lattice Thermal Transport in Chalcogenide Perovskite BaZrS 3. https://doi.org/10.1021/acsaem.9b02185

210. Linnera J, Karttunen AJ (2017) Ab initio study of the lattice thermal conductivity of Cu2 O using the generalized gradient approximation and hybrid density functional methods. Phys Rev B 96:. https://doi.org/10.1103/PHYSREVB.96.014304/FIGURES/1/THUMBNAIL

211. Glebko N, Karttunen AJ (2019) Lattice thermal conductivity of TiS2, ZrS2, and HfS2: Periodic trends studied by dispersion-corrected hybrid density functional methods. Phys Rev B 100:. https://doi.org/10.1103/PHYSREVB.100.024301/FIGURES/1/THUMBNAIL

212. Pandey T, Parker DS, Lindsay L (2017) Ab initio phonon thermal transport in monolayer InSe, GaSe, GaS, and alloys. Nanotechnology 28:455706. https://doi.org/10.1088/1361-6528/AA8B39

213. Han Y, Dong J, Qin G, Hu M (2016) Phonon transport in the ground state of two-

dimensional silicon and germanium. RSC Adv 6:69956–69965. https://doi.org/10.1039/C6RA14351B

214. Shi H, Wang D, Xiao Y, Zhao L-D (2021) Dynamic carrier transports and low thermal conductivity in n-type layered InSe thermoelectrics. Aggregate 2:e92. https://doi.org/10.1002/AGT2.92

215. Zhou F, Nielson W, Xia Y, Ozoliņš V (2019) Compressive sensing lattice dynamics. I. General formalism. Phys Rev B 100:184308. https://doi.org/10.1103/PHYSREVB.100.184308/FIGURES/8/MEDIUM

216. Oba Y, Tadano T, Akashi R, Tsuneyuki S (2019) First-principles study of phonon anharmonicity and negative thermal expansion in ScF3. Phys Rev Mater 3:033601. https://doi.org/10.1103/PHYSREVMATERIALS.3.033601/FIGURES/10/MEDIUM

Appendix

Appendix A: Description of Research for Popular Publication

The unquenchable global quest for more dependable and secure energy sources has resulted in a dramatic increase in social and political instability. Many nations are strengthening their research and development efforts in order to produce a more sustainable energy option. Such efforts are designed at mitigating the environmental effects of the global climate change, which is growing increasingly alarming as a result of fossil fuel burning. Around 90% of the world's power is generated by thermal energy from fossil fuel burning. Production facilities normally function at 30-40% efficiency, dissipating approximately fifteen terawatts of energy to the environment as heat. Waste heat can be converted into usable power using thermoelectric generators. The quantity of heat generated by many industrial and residential operations, as well as automobile exhaust, might be converted to energy using thermoelectric devices. Thermoelectric devices could create electrical currents in the presence of heat gradients, making them potential power sources. Thermoelectric devices are solid-state devices that have no moving parts and are quiet, dependable, and scalable, making them suitable for small-scale electricity production. Electrical and thermal connections connect two dissimilar types of semiconductor materials in series and parallel to form a thermoelectric device. Based on this definition of thermoelectric devices, it is critical to identify thermoelectric materials with a high degree of efficiency.

In this research, we are seeking new materials with optimal properties (structural, electronic, magnetic, and thermoelectric) for spintronic and thermoelectric applications to provide them to the world. Metal oxides are among the studied material, which are found to be very promising thermoelectric materials at elevated temperature because of their high melting

point and chemical stability at increased temperatures. Other investigated materials are the quaternary Heusler alloys, which exhibit unusual features such as high thermoelectric efficiency and half-metallic behaviors. These unusual features make them to be promising for thermoelectric and spintronic applications. The last investigated material belongs to the group of two-dimensional chalcogenides. This group has gained considerable interest in nano-photonics and nano-electronics, due to its superior optical, electrical, mechanical, and thermoelectric properties.

Appendix B: Executive Summary of Newly Created Intellectual Property

As a result of this findings of the studies, newly created intellectual property should be considered as follows:

1. Thermoelectric properties of the rock-salt and wurtzite of $Zn_xCd_{1-x}O$ alloys.
2. Thermoelectric properties of different quaternary Heusler alloys such as VTiRhZ (Z=Al, Ga, In, Si, Ge, Sn) and ZrTiRhZ (Z=Ge, Sn).
3. Anharmonic effects on lattice dynamics and thermal transport of two-dimensional InTe Monolayer.

Appendix C: Potential Patent and Commercialization Aspects of Listed Intellectual Property Items

C.1 Patentability of Intellectual Property (Could Each Item be Patented)

1. Thermoelectric properties of rock-salt and wurtzite of $Zn_xCd_{1-x}O$ alloys and different quaternary Heusler alloys, namely, VTiRhZ(Z=Al, Ga, In, Si, Ge, Sn) and ZrTiRhZ(Z=Ge, Sn) were studied by using density functional theory. These results could not be patented.
2. Anharmonic effects on lattice dynamics and thermal transport of two-dimensional InTe monolayer were also studied by using density functional theory. These investigations could not be patented.

C.2 Commercialization Prospects (Should Each Item Be Patented)

N/A

C.3 Possible Prior Disclosure of IP

1. The findings of the studies have been published in preeminent peer-reviewed journals (see Appendix G).

Appendix D: Broader Impact of Research

D.1 Applicability of Research Methods to Other Problems

The findings of this study demonstrated that the rock-salt and wurtzite of $Zn_xCd_{1-x}O$ alloys, quaternary Heusler alloys such as VTiRhZ (Z=Al, Ga, In, Si, Ge, Sn) and ZrTiRhZ (Z=Ge, Sn), as well as the two-dimensional InTe monolayer, may be employed as thermoelectric devices to convert thermal energy into electricity. Additionally, this quaternary Heusler alloys showed a perfect spin-polarization of 100% and half-metallic behavior, which make them to be promising materials for spintronic application, spin injector, spin-valve application, and magnetic tunnel junction.

D.2 Impact of Research Results on U.S. and Global Society

This proposed study in this dissertation can be contributed to the progress of alternative sources of energy such as thermoelectric and spintronic devices. The thermoelectric devices could be designed by two dissimilar semiconductor materials, which can convert thermal energy to power energy. This source of renewable power has the potential to minimize the dependency of our society on fossil fuels. This can benefit the environment and the economy, in addition to securing the energy demands of the society even when fossil fuels run out. This source can be used in a variety of fields, including power production, refrigeration, air conditioning, and biomedical equipments.

D.3 Impact of research results on the environment

One of the drawbacks of fossil fuels, as the primary source energy, is pollution. Therefore, researchers worldwide are seeking for other sources of power to help reduce this reliance. This study focuses on developing new materials with optimal magnetic and

thermoelectric properties for spintronic and thermoelectric applications. These applications are environmentally friendly because they do not emit gas emissions or poisonous liquids.

Appendix E: Microsoft Project for Ph.D Micro-EP Degree Plan

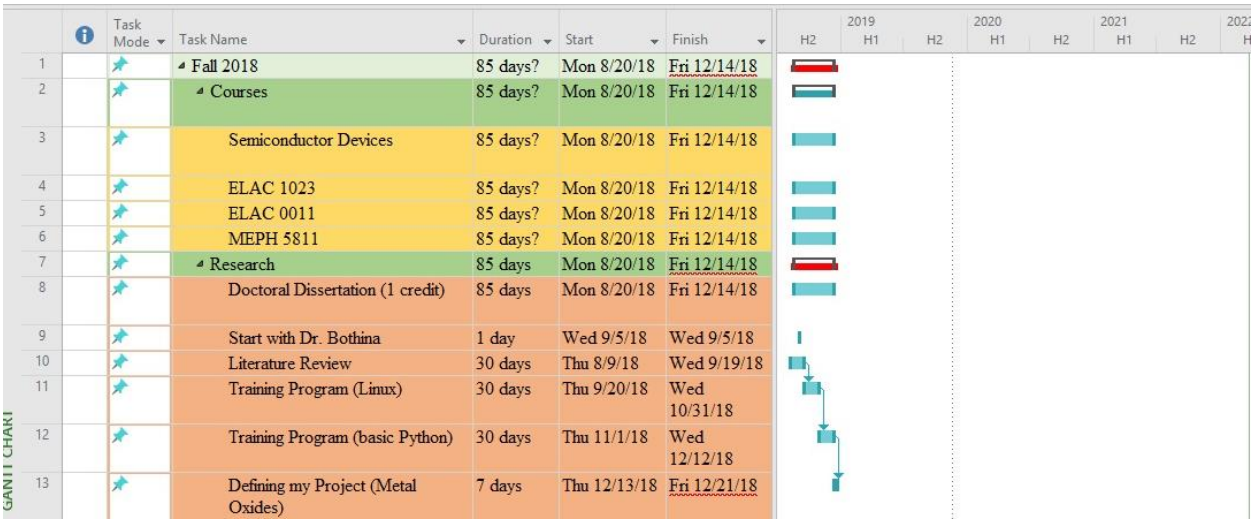

	Task Mode	Task Name	Duration	Start	Finish
1		Fall 2018	85 days?	Mon 8/20/18	Fri 12/14/18
2		Courses	85 days?	Mon 8/20/18	Fri 12/14/18
3		Semiconductor Devices	85 days?	Mon 8/20/18	Fri 12/14/18
4		ELAC 1023	85 days?	Mon 8/20/18	Fri 12/14/18
5		ELAC 0011	85 days?	Mon 8/20/18	Fri 12/14/18
6		MEPH 5811	85 days?	Mon 8/20/18	Fri 12/14/18
7		Research	85 days	Mon 8/20/18	Fri 12/14/18
8		Doctoral Dissertation (1 credit)	85 days	Mon 8/20/18	Fri 12/14/18
9		Start with Dr. Bothina	1 day	Wed 9/5/18	Wed 9/5/18
10		Literature Review	30 days	Thu 8/9/18	Wed 9/19/18
11		Training Program (Linux)	30 days	Thu 9/20/18	Wed 10/31/18
12		Training Program (basic Python)	30 days	Thu 11/1/18	Wed 12/12/18
13		Defining my Project (Metal Oxides)	7 days	Thu 12/13/18	Fri 12/21/18

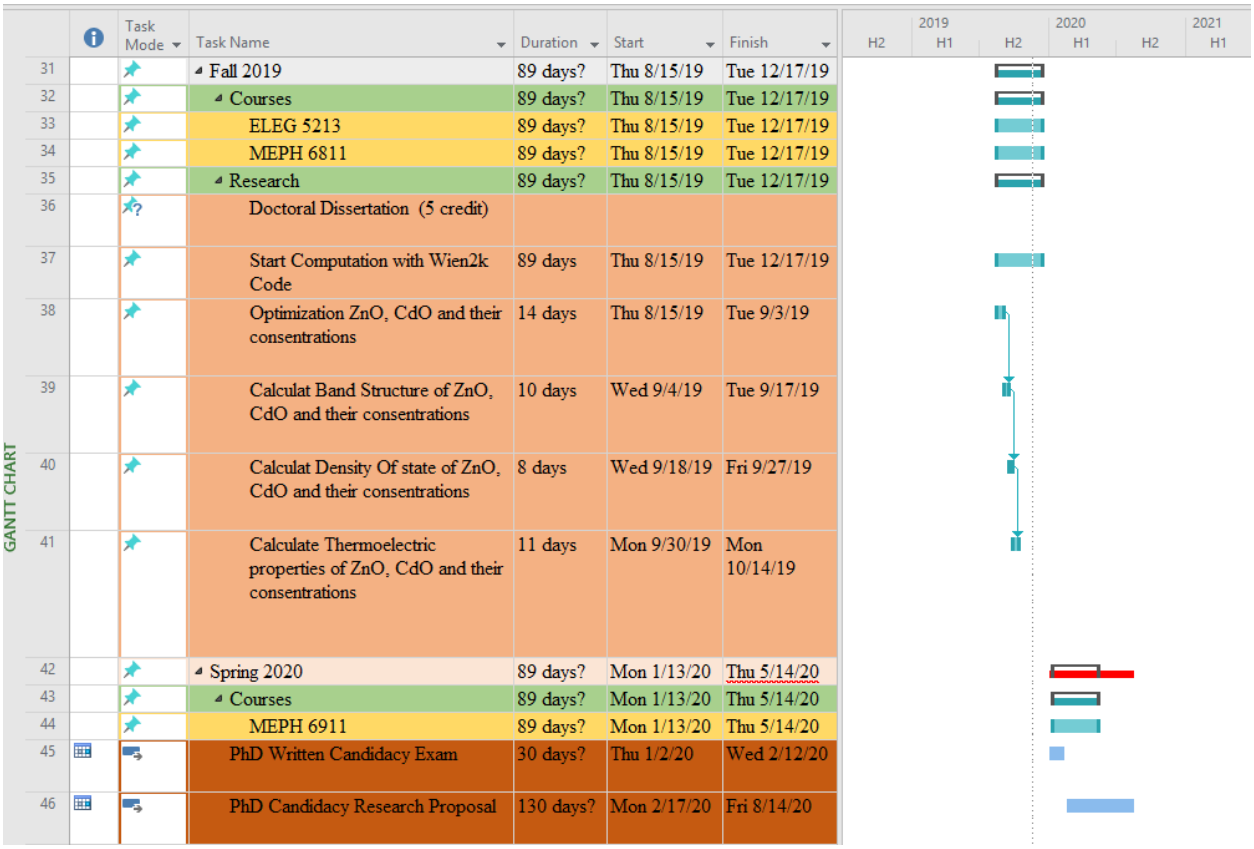

	Task Mode	Task Name	Duration	Start	Finish
31		Fall 2019	89 days?	Thu 8/15/19	Tue 12/17/19
32		Courses	89 days?	Thu 8/15/19	Tue 12/17/19
33		ELEG 5213	89 days?	Thu 8/15/19	Tue 12/17/19
34		MEPH 6811	89 days?	Thu 8/15/19	Tue 12/17/19
35		Research	89 days?	Thu 8/15/19	Tue 12/17/19
36		Doctoral Dissertation (5 credit)			
37		Start Computation with Wien2k Code	89 days	Thu 8/15/19	Tue 12/17/19
38		Optimization ZnO, CdO and their consentrations	14 days	Thu 8/15/19	Tue 9/3/19
39		Calculat Band Structure of ZnO, CdO and their consentrations	10 days	Wed 9/4/19	Tue 9/17/19
40		Calculat Density Of state of ZnO, CdO and their consentrations	8 days	Wed 9/18/19	Fri 9/27/19
41		Calculate Thermoelectric properties of ZnO, CdO and their consentrations	11 days	Mon 9/30/19	Mon 10/14/19
42		Spring 2020	89 days?	Mon 1/13/20	Thu 5/14/20
43		Courses	89 days?	Mon 1/13/20	Thu 5/14/20
44		MEPH 6911	89 days?	Mon 1/13/20	Thu 5/14/20
45		PhD Written Candidacy Exam	30 days?	Thu 1/2/20	Wed 2/12/20
46		PhD Candidacy Research Proposal	130 days?	Mon 2/17/20	Fri 8/14/20

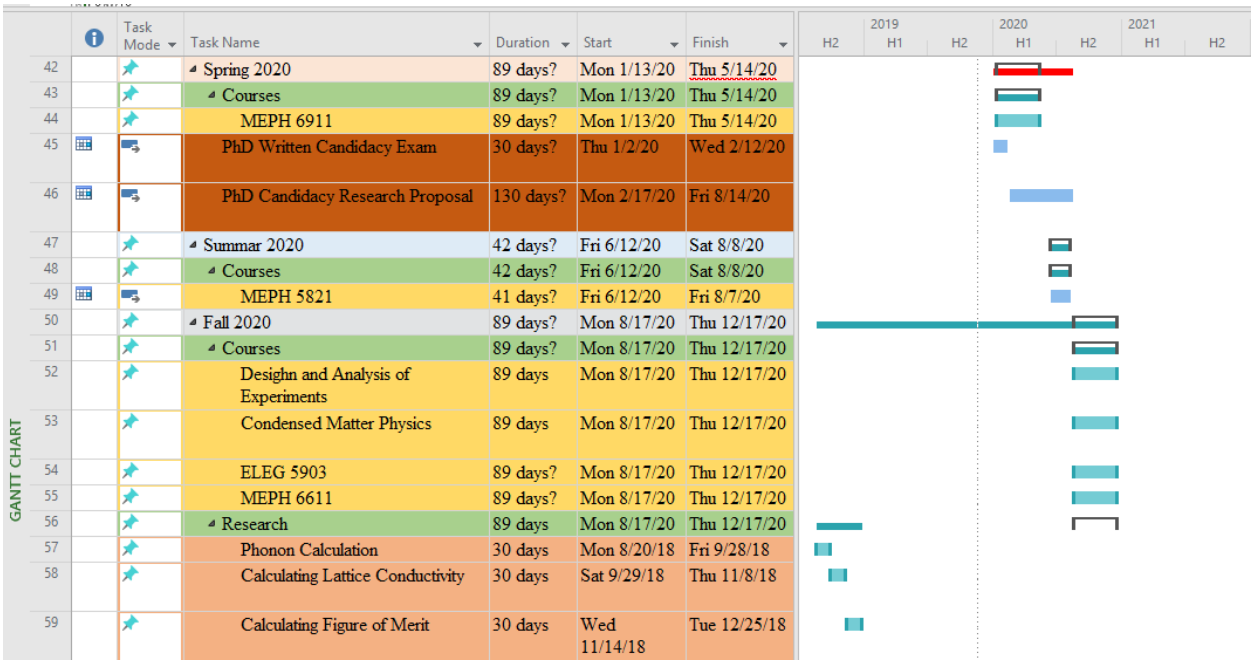

GANTT CHART

	Task Mode	Task Name	Duration	Start	Finish
42		Spring 2020	89 days?	Mon 1/13/20	Thu 5/14/20
43		Courses	89 days?	Mon 1/13/20	Thu 5/14/20
44		MEPH 6911	89 days?	Mon 1/13/20	Thu 5/14/20
45		PhD Written Candidacy Exam	30 days?	Thu 1/2/20	Wed 2/12/20
46		PhD Candidacy Research Proposal	130 days?	Mon 2/17/20	Fri 8/14/20
47		Summar 2020	42 days?	Fri 6/12/20	Sat 8/8/20
48		Courses	42 days?	Fri 6/12/20	Sat 8/8/20
49		MEPH 5821	41 days?	Fri 6/12/20	Fri 8/7/20
50		Fall 2020	89 days?	Mon 8/17/20	Thu 12/17/20
51		Courses	89 days?	Mon 8/17/20	Thu 12/17/20
52		Desighn and Analysis of Experiments	89 days	Mon 8/17/20	Thu 12/17/20
53		Condensed Matter Physics	89 days	Mon 8/17/20	Thu 12/17/20
54		ELEG 5903	89 days?	Mon 8/17/20	Thu 12/17/20
55		MEPH 6611	89 days?	Mon 8/17/20	Thu 12/17/20
56		Research	89 days	Mon 8/17/20	Thu 12/17/20
57		Phonon Calculation	30 days	Mon 8/20/18	Fri 9/28/18
58		Calculating Lattice Conductivity	30 days	Sat 9/29/18	Thu 11/8/18
59		Calculating Figure of Merit	30 days	Wed 11/14/18	Tue 12/25/18

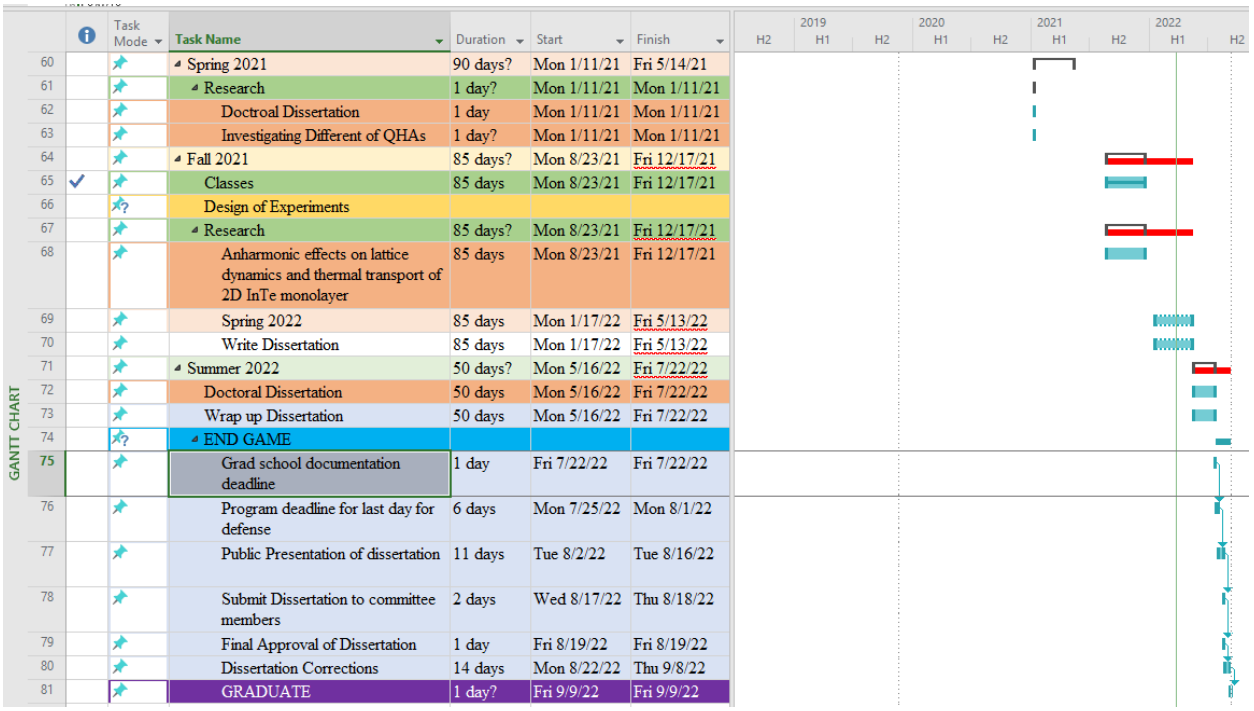

GANTT CHART

	Task Mode	Task Name	Duration	Start	Finish
60		Spring 2021	90 days?	Mon 1/11/21	Fri 5/14/21
61		Research	1 day?	Mon 1/11/21	Mon 1/11/21
62		Doctroal Dissertation	1 day	Mon 1/11/21	Mon 1/11/21
63		Investigating Different of QHAs	1 day?	Mon 1/11/21	Mon 1/11/21
64		Fall 2021	85 days?	Mon 8/23/21	Fri 12/17/21
65		Classes	85 days	Mon 8/23/21	Fri 12/17/21
66		Design of Experiments			
67		Research	85 days?	Mon 8/23/21	Fri 12/17/21
68		Anharmonic effects on lattice dynamics and thermal transport of 2D InTe monolayer	85 days	Mon 8/23/21	Fri 12/17/21
69		Spring 2022	85 days	Mon 1/17/22	Fri 5/13/22
70		Write Dissertation	85 days	Mon 1/17/22	Fri 5/13/22
71		Summer 2022	50 days?	Mon 5/16/22	Fri 7/22/22
72		Doctoral Dissertation	50 days	Mon 5/16/22	Fri 7/22/22
73		Wrap up Dissertation	50 days	Mon 5/16/22	Fri 7/22/22
74		END GAME			
75		Grad school documentation deadline	1 day	Fri 7/22/22	Fri 7/22/22
76		Program deadline for last day for defense	6 days	Mon 7/25/22	Mon 8/1/22
77		Public Presentation of dissertation	11 days	Tue 8/2/22	Tue 8/16/22
78		Submit Dissertation to committee members	2 days	Wed 8/17/22	Thu 8/18/22
79		Final Approval of Dissertation	1 day	Fri 8/19/22	Fri 8/19/22
80		Dissertation Corrections	14 days	Mon 8/22/22	Thu 9/8/22
81		GRADUATE	1 day?	Fri 9/9/22	Fri 9/9/22

Appendix F: Identification of all software used in research and dissertation generation Computer #1: Personal Laptop

Model Number: 15-cs0061c1

Serial Number: 5cd82545JD

Owner: Hind Alqurashi

Computer #2: Personal Laptop

Model Number: A1278

Serial Number: C02H6023DV13

Owner: Hind Alqurashi

Computer #3:

Model Number: N/A

Serial Number: N/A

Owner: Prof. Bothina Hamad-Manasreh

Software #1:

Name: Ubuntu

license: downloaded by Hind Alqurashi

Software #2:

Name: XMGRACE

license: downloaded by Hind Alqurashi

Software #3:

Name: VESTA

Free license: downloaded by Hind Alqurashi

Software #4:

Name: Mendeley

Free license: downloaded by Hind Alqurashi

Software #5:

Name: Adobe Illustrator

Purchased by: Hind Alqurashi

Software #6:

Name: XCrySden

Free license: downloaded by Hind Alqurashi

Software #7:

Name: VM VirtualBox

Free license: downloaded by Hind Alqurashi

Appendix G: All publications published, submitted, and planned Publications

Publications published

Part of Chapter 8 was originally published as:

1. Alqurashi H, Pandit A, Hamad B (2022) Anharmonic effects on lattice dynamics and thermal transport of two-dimensional InTe Monolayer. https://doi.org/10.1016/j.mseb.2022.115823

Part of Chapter 7 was originally published as:

2. Alqurashi H, Haleoot R, Hamad B (2022) First-principles investigations of Zr-based Quaternary Heusler Alloys for spintronic and thermoelectric applications. Computational materials scinces. https://doi.org/10.1016/j.commatsci.2022.111477

3. Sanjay E, Alqurashi H, Hamad B (2022) Lattice Dynamics, Mechanical Properties, Electronic Structure and Magnetic Properties of Equiatomic Quaternary Heusler Alloys CrTiCoZ (Z =Al,Si) using first principles calculations. https://doi.org/10.3390/ma15093128

Part of Chapter 6 was originally published as:

4. Alqurashi H, Haleoot R, Hamad B (2021) First-principles investigations of the electronic, magnetic and thermoelectric properties of VTiRhZ (Z= Al, Ga, In) Quaternary Heusler alloys. Mater Chem Phys 125685. https://doi.org/10.1016/J.MATCHEMPHYS.2021.125685.

Part of Chapter 5 was originally published as:

5. Alqurashi H, Hamad B (2021) Magnetic structure, mechanical stability and thermoelectric properties of VTiRhZ (Z = Si, Ge, Sn) quaternary Heusler alloys: first-principles calculations. Appl Phys A Mater Sci Process 127:1–11. https://doi.org/10.1007/S00339-021-04949-0/FIGURES/6.

Part of Chapter 4 was originally published as:

6. Alqurashi H, Haleoot R, Pandit A, Hamad B (2021) Investigations of the electronic, dynamical, and thermoelectric properties of $Cd_{1-x}Zn_xO$ alloys: First-principles calculations. Mater Today Commun 28:102511. https://doi.org/10.1016/j.mtcomm.2021.102511.

Publications submitted

1. Hzzazi A, Alqurashi H, Hamad B (2022) Theoretical Investigations of the structural, dynamical, electronic, magnetic, and thermoelectric properties of CoYRhSi (Y = Cr, Mn) quaternary Heusler alloys.

Publications planned

1. Shurug, Alqurashi H, Sanjay E, Hamad B First-principal Investigations of the Electronic, Magnetic and Thermoelectric Properties of CrTiRhAl Quaternary Heusler Alloy.

2. Alqurashi H, Hamad B (2023) Theoretical Investigations of the structural, and thermoelectric properties of two-dimensional $ZrCl_2$ Monolayer.

3. Sanjay E, Alqurashi H, Pandit A, Hamad B (2023) Anharmonic effects on lattice dynamics and thermal transport of two-dimensional HfX_2 (S, Se, Te) Monolayer.

Presentations

1. Hind Alqurashi and Bothina Hamad 2022 Magnetic structure, mechanical stability and thermoelectric properties of VTiRhZ (Z = Si, Ge, Sn) quaternary Heusler alloys: first-principles calculations of the American Physical Society, APS March Meeting, (March 2022).